People`s Democratic Republic of Algeria

Ministry of Higher Education and Scientific Research

University of Echahid Hamma Lakhdar - El Oued

Faculty of Technology

Department of Process Engineering and Petrochemical

Dissertation

ACADEMIC MASTER

Domain: Technology

Division: Process Engineering

Specialty: Chemical Engineering

Presented by:

1. SADINE Hadjer
2. BEN MOUSSA Zohra

Entitled:

Sustainable Synthesis and Characterization of Nanocomposites for Simultaneous Removal of Heavy Metals and Organic Pollutants from Industrial Wastewater

Publicly defended in: 13/06/2026

Board of Examiners:

Dr. DIA Ouahida	**Chairman**
Dr. BOUAFIA Abderrhmane	**Supervisor**
Mr. NESRAT Hocine Sadam	**Assistant Supervisor**
Dr. BERRA Djamila	**Examiner**

Academic Year: 2025/2026

Dedication

Dedication

To those whom Allah has commanded us to honor and obey, who sacrificed their rest to light my path with their love and generosity—my dear parents. May Allah grant them long lives filled with health and well-being.

To those who shared with me the warmth of home and were my greatest support throughout this journey my beloved brothers and sisters, each holding a special place in my heart. And a loyal tribute to those companions who have passed on, whose memories remain forever alive in the depths of my soul.

To those who ignited in me the love of knowledge and gave generously without hesitation—my esteemed teachers and professors, each deserving of the highest respect and gratitude.

Finally, I ask Allah Almighty to make this work sincere for His sake, beneficial to His servants, and a light in the scale of my good deeds on the Day when only a pure heart will avail.

Acknowledgements

Acknowledgements

By the grace and blessings of Allah, we present the fruit of our labor.

First and foremost, we would like to express our sincere gratitude to our supervisor, ***BOUAFIA Abderrhmane****, who served as a guiding light throughout our research. We are deeply grateful for his unwavering dedication and efforts in ensuring the success of this work.*

Our gratitude also extends to all our esteemed professors in the Process Engineering Department and to the members of the jury who honored us by agreeing to review and evaluate this thesis.

To our companions on this journey—the Master 2 Chemical Engineering students—and to all our friends and everyone who encouraged us, even with a simple word, we offer our highest appreciation and thanks.

Abstract

ملخص

Résumé

Abstract

Heavy metals (As, Cd, Cr, Mn, Mo, Ni, Pb, Sb, Se, and Zn) in petrochemical wastewater and Rose Bengal dye in textile industrial wastewater pose serious environmental and public health risks due to their toxicity, persistence, and bioaccumulation potential. The effective removal of these pollutants from their respective effluents remains a major challenge in sustainable wastewater management. $ZnFe_2O_4$ spinel ferrite nanoparticles were synthesized via co-precipitation using zinc acetate dihydrate and iron(III) chloride hexahydrate, followed by calcination at 800 °C. XRD confirmed a single-phase cubic spinel structure ($Fd\bar{3}m$) with a lattice parameter of 8.4300 Å and a crystallite size of 26.74 ± 0.50 nm. FTIR identified metal–oxygen stretching vibrations at 531 and 432 cm^{-1}, while UV-Vis spectroscopy revealed an optical bandgap of 2.5 eV, confirming visible-light photoactivity. When applied to real petrochemical wastewater, the nanoparticles achieved removal efficiencies exceeding 99.90% for all ten heavy metals within 30 minutes, with Cr, Mo, and Se reaching complete elimination after 20 minutes. They also reduced oil-in-water content, TSS, and COD by 95.20%, 93.83%, and 98.34%, respectively. Under natural solar irradiation, the photocatalytic degradation of Rose Bengal dye reached 94.38% within 90 minutes without any chemical additives or artificial light sources. These results establish $ZnFe_2O_4$ nanoparticles as a versatile and sustainable material capable of addressing both inorganic and organic pollutants in different complex industrial effluents.

Keywords: *$ZnFe_2O_4$ nanoparticles; heavy metals; Rose Bengal dye; petrochemical wastewater; textile wastewater; adsorption; photocatalysis; spinel ferrite; co-precipitation.*

Résumé

Les métaux lourds (As, Cd, Cr, Mn, Mo, Ni, Pb, Sb, Se, et Zn) dans les eaux usées pétrochimiques et le colorant Rose Bengale dans les eaux usées textiles posent de graves risques environnementaux et sanitaires en raison de leur toxicité, de leur persistance et de leur potentiel de bioaccumulation. Leur élimination efficace dans leurs effluents respectifs reste un défi majeur dans la gestion durable des eaux usées industrielles. Des nanoparticules de $ZnFe_2O_4$ spinelle ferrite ont été synthétisées par co-précipitation en utilisant de l'acétate de zinc dihydraté et du chlorure de fer(III) hexahydraté, suivie d'une calcination à 800 °C. La DRX a confirmé une structure spinelle cubique monophasée ($Fd\bar{3}m$) avec un paramètre de maille de 8,4300 Å et une taille de cristallites de 26,74 ± 0,50 nm. L'analyse FTIR a identifié des vibrations d'élongation métal-oxygène à 531 et 432 cm^{-1}, tandis que la spectroscopie UV-Vis a révélé une bande interdite optique de 2,5 eV, confirmant la photoactivité sous lumière visible. Appliquées aux eaux usées pétrochimiques réelles, les nanoparticules ont atteint des rendements d'élimination supérieurs à 99,90 % pour les dix métaux lourds en 30 minutes, avec élimination complète de Cr, Mo et Se après 20 minutes. Elles ont également réduit la teneur en huile-dans-eau, les MES et la DCO de 95,20 %, 93,83 % et 98,34 % respectivement. Sous irradiation solaire naturelle, la dégradation photocatalytique du Rose Bengale a atteint 94,38 % en 90 minutes sans aucun additif chimique ni source de lumière artificielle. Ces résultats établissent les nanoparticules de $ZnFe_2O_4$ comme un matériau polyvalent et durable capable de traiter les polluants inorganiques et organiques dans différents effluents industriels complexes.

Mots-clés : Nanoparticules $ZnFe_2O_4$; métaux lourds ; Rose Bengale ; eaux usées pétrochimiques ; eaux usées textiles ; adsorption ; photocatalyse ; ferrite spinelle ; co-précipitation.

ملخص

تُمثّل المعادن الثقيلة (As، Cd، Cr، Mn، Mo، Ni، Pb، Sb، Se، وZn) في مياه الصرف البتروكيماوي وصبغة روز بنغال في مياه الصرف النسيجي تهديدًا بيئيًا وصحيًا خطيرًا بسبب سميّتها وثباتها وإمكانية تراكمها البيولوجي. ويظل إزالتها الفعّالة من مياه الصرف الخاصة بها تحدّيًا رئيسيًا في الإدارة المستدامة لمياه الصرف الصناعي. تم تصنيع نانوجسيمات $ZnFe_2O_4$ سبينيل فريت بطريقة الترسيب المشترك باستخدام أسيتات الزنك ثنائي الماء وكلوريد الحديد (III)سداسي الماء، تلاها التكليس عند 800 درجة مئوية. أكد تحليل XRD بنية سبينيل مكعبة أحادية الطور ($Fd\bar{3}m$)بمعامل شبكة 8.4300 Å وحجم بلورات 26.74 ± 0.50 نانومتر. كشف FTIR عن اهتزازات تمدد معدن-أكسجين عند 531 و432 سم$^{-1}$، بينما أظهر UV-Vis فجوة نطاق بصرية قدرها 2.5 إلكترون فولت، مؤكدًا النشاط الضوئي تحت الضوء المرئي. عند تطبيقها على مياه صرف بتروكيماوية حقيقية، حققت النانوجسيمات كفاءات إزالة تجاوزت 99.90% لجميع المعادن الثقيلة العشرة خلال 30 دقيقة، مع إزالة كاملة لـ Cr و Mo و Se بعد 20 دقيقة. كما خفضت محتوى الزيت في الماء والمواد العالقة والطلب الكيميائي على الأكسجين بنسب 95.20% و93.83% و98.34% على التوالي. تحت الإشعاع الشمسي الطبيعي، بلغ تحلل صبغة Rose Bengal 94.38% في 90 دقيقة دون أي مضافات كيميائية أو مصدر ضوء اصطناعي. تُثبت هذه النتائج أن نانوجسيمات $ZnFe_2O_4$ مادة متعددة الوظائف ومستدامة قادرة على معالجة الملوثات غير العضوية والعضوية في مياه الصرف الصناعي المعقدة المختلفة.

الكلمات المفتاحية *: نانوجسيمات $ZnFe_2O_4$ ؛ معادن ثقيلة؛ روز بنغال؛ مياه صرف بتروكيماوية؛ مياه صرف نسيجي؛ امتزاز؛ تحفيز ضوئي؛ فريت سبينيل؛ ترسيب مشترك.*

TABLE OF CONTENTS

Table of Contents

Chapter III : Study of Efficient Heavy Metals Removal

List of Figures

Chapter II : Synthesis and Characterization

Chapter III : Study of Efficient Heavy Metals Removal

Chapter IV: Photocatalytic Activity Study of Rose Bengal

List of Tables

List of Abbreviations

ABBREVIATION	FULL TERM
$ZnFe_2O_4$	Zinc Ferrite nanoparticles
NPs	Nanoparticles
XRD	X-ray Diffraction
FTIR	Fourier Transform Infrared Spectroscopy
UV-Vis	Ultraviolet-Visible Spectroscopy
ICP-MS	Inductively Coupled Plasma Mass Spectrometry
Eg	Optical Bandgap Energy
FWHM	Full Width at Half Maximum
FCC	Face-Centered Cubic
JCPDS	Joint Committee on Powder Diffraction Standards
AOP	Advanced Oxidation Process
ROS	Reactive Oxygen Species
VB	Valence Band
CB	Conduction Band
SPR	Surface Plasmon Resonance
LSPR	Localized Surface Plasmon Resonance
QSE	Quantum Size Effect
TiO_2	Titanium Dioxide
RB	Rose Bengal
POP	Persistent Organic Pollutant
RE%	Removal Efficiency (%)
COD	Chemical Oxygen Demand

TSS	Total Suspended Solids
OIW	Oil-in-Water content
MCL	Maximum Contaminant Level
USEPA	United States Environmental Protection Agency
DI	Deionized water
PEG	Polyethylene Glycol
MRI	Magnetic Resonance Imaging

General Introduction

General Introduction

Fresh water scarcity and the progressive deterioration of aquatic ecosystems stand today among the most consequential environmental challenges confronting the global community. Industrial expansion, largely unrestrained in many developing regions, has dramatically accelerated the discharge of hazardous substances into water bodies, with petrochemical operations and textile industries occupying a particularly prominent place among the sectors responsible for severe aquatic contamination [1]. The effluents generated by oil and gas production facilities carry heavy metals (As, Cd, Cr, Mn, Mo, Ni, Pb, Sb, Se and Zn), emulsified hydrocarbons, suspended particulate matter, and elevated organic loads. On the other hand, textile wastewater is heavily loaded with synthetic dyes such as Rose Bengal. This renders their treatment far more demanding than that of wastewater streams arising from most other industrial activities.

Heavy metals constitute the most critically concerning fraction in petrochemical wastewater. Unlike organic pollutants, which can in principle be mineralized by biological or chemical action, heavy metals are chemically inert in the sense that they resist degradation entirely once introduced into an aquatic environment, they persist indefinitely, accumulate progressively in sediments and living organisms, and migrate up trophic chains with increasing concentration at each level [2]. The consequences for human health are well documented and severe: prolonged or acute exposure to heavy metals such as arsenic, cadmium, lead, chromium, and nickel has been causally linked to a broad spectrum of pathological outcomes, including neurological damage, renal failure, hepatotoxicity, developmental abnormalities in children, and multiple forms of malignancy [3]. Regulatory agencies including the United States Environmental Protection Agency (USEPA) and the World Health Organization (WHO) have accordingly established maximum contaminant levels for these elements in drinking water and discharge effluents, though compliance remains inconsistent in many industrial contexts worldwide.

Alongside inorganic heavy metal contamination, synthetic organic dyes represent a second major class of recalcitrant industrial pollutant, particularly in textile wastewater. The textile and printing industries discharge millions of tonnes of dye-laden wastewater annually, much of it containing structurally complex compounds that are highly resistant to biological degradation and

acutely toxic to aquatic organisms even at trace concentrations [4]. Rose Bengal, a xanthene-based dye widely used in industrial and biomedical applications, exemplifies this class of compound: it is highly soluble in water, photostable, and known to generate reactive oxygen species under irradiation that damage cellular membranes and disrupt aquatic ecosystems The development of effective strategies for the treatment of these two distinct categories of pollutants in their respective industrial effluents (petrochemical for heavy metals and textile for dyes) is therefore not merely a technical ambition but an environmental and public health necessity.

Conventional wastewater treatment approaches including chemical precipitation, ion exchange, flotation, and biological degradation have demonstrated meaningful but ultimately limited effectiveness against the full complexity of industrial effluent matrices [5]. Despite some progress, a significant research gap remains in developing a single versatile material capable of efficiently addressing heavy metals in real petrochemical wastewater and organic dyes such as Rose Bengal in textile wastewater under practical conditions (real effluents, natural solar light, without chemical additives).

This gap raises the following research question: Can $ZnFe_2O_4$ spinel ferrite nanoparticles, synthesized via a simple and scalable method, simultaneously serve as an effective adsorbent for multiple heavy metals in real petrochemical wastewater and as a visible-light photocatalyst for Rose Bengal dye degradation in textile wastewater?

Nanotechnology has emerged over the past two decades as one of the most promising domains of innovation for water and wastewater treatment [6, 7]. Among the family of spinel ferrite nanoparticles, zinc ferrite ($ZnFe_2O_4$) has progressively distinguished itself as a material of exceptional versatility for environmental remediation applications due to its high surface reactivity and suitable bandgap for visible-light photocatalysis [8, 9].

The co-precipitation method has established itself as the synthesis route of choice for $ZnFe_2O_4$ nanoparticles in environmental applications, owing to its operational simplicity, scalability, and capacity to yield phase-pure, nanocrystalline products [10].

The present work was conceived within this scientific context, with the objective of synthesizing and characterizing $ZnFe_2O_4$ spinel ferrite nanoparticles via co-precipitation and evaluating their capacity to address the two distinct categories of industrial water pollution mentioned above. The study is organized across four chapters. **Chapter I** provides a comprehensive theoretical background on nanomaterials their history, classification, properties, and synthesis routes with particular attention to metallic oxide nanoparticles and the spinel ferrite structural family. **Chapter II** details the synthesis and full physicochemical characterization of the $ZnFe_2O_4$ nanoparticles, employing UV-Vis spectrophotometry, FTIR spectroscopy, and X-ray diffraction to establish their optical, chemical, and structural identity. **Chapter III** investigates the adsorption performance of the synthesized material toward ten heavy metal species simultaneously present in real petrochemical wastewater, evaluating removal efficiency as a function of contact time and discussing the governing mechanisms. **Chapter IV** assesses the photocatalytic activity of $ZnFe_2O_4$ nanoparticles for the degradation of Rose Bengal dye under natural solar light irradiation, establishing a link between the material's optical properties and its remediation performance toward persistent organic pollutants.

References

1. Oladimeji TE, Oyedemi M, Emetere ME, et al (2024) Review on the impact of heavy metals from industrial wastewater effluent and removal technologies. Heliyon 10:e40370. https://doi.org/10.1016/j.heliyon.2024.e40370
2. Mitra S, Chakraborty AJ, Tareq AM, et al (2022) Impact of heavy metals on the environment and human health: Novel therapeutic insights to counter the toxicity. J King Saud Univ - Sci 34:101865. https://doi.org/10.1016/j.jksus.2022.101865
3. Tchounwou PB, Yedjou CG, Patlolla AK, Sutton DJ (2012) Heavy metal toxicity and the environment. In: Exs. pp 133–164
4. Bayuo J, Rwiza MJ, Sillanpää M, Mtei KM (2023) Removal of heavy metals from binary and multicomponent adsorption systems using various adsorbents - a systematic review. RSC Adv 13:13052–13093. https://doi.org/10.1039/d3ra01660a
5. Qasem NAA, Mohammed RH, Lawal DU (2021) Removal of heavy metal ions from wastewater: a comprehensive and critical review. npj Clean Water 4:36. https://doi.org/10.1038/s41545-021-00127-0
6. Ali I, Peng C, Khan ZM, et al (2019) Overview of microbes based fabricated biogenic nanoparticles for water and wastewater treatment. J Environ Manage 230:128–150. https://doi.org/10.1016/j.jenvman.2018.09.073
7. Roshanfekr Rad L, Anbia M (2021) Zeolite-based composites for the adsorption of toxic matters from water: A review. J Environ Chem Eng 9:106088. https://doi.org/10.1016/j.jece.2021.106088
8. Darandale S V., Hase D, Mane K, et al (2025) Synthesis of Spinel Ferrites and Their Composites: A Comprehensive Review on Synthesis Methods, Characterization Techniques, and Photocatalytic Applications. J Chem Rev 7:216–235. https://doi.org/10.48309/jcr.2025.505407.1416
9. Zhao X, Baharinikoo L, Farahani MD, et al (2022) Experimental modelling studies on the removal of dyes and heavy metal ions using ZnFe2O4 nanoparticles. Sci Rep 12:5987. https://doi.org/10.1038/s41598-022-10036-y
10. Yadav RS, Havlica J, Kuřitka I, et al (2015) Magnetic Properties of ZnFe2O4 Nanoparticles Synthesized by Starch-Assisted Sol–Gel Auto-combustion Method. J Supercond Nov Magn 28:1417–1423. https://doi.org/10.1007/s10948-014-2870-z

CHAPTER I

Nanomaterials in Catalysis and Wastewater Treatment

I.1. Overview of Nanomaterials

The term "nanotechnology" refers to the science and engineering of materials and devices structured at the atomic or molecular scale. The prefix *nano* is derived from the Greek word *nanos*, meaning dwarf, and corresponds to one billionth of a meter (10^{-9} m). Materials operating within this dimensional regime, generally spanning from 1 to 100 nanometers as illustrated in **Figure (I.1)**, exhibit markedly different properties compared to their bulk counterparts [1].

This dramatic transformation in behavior arises primarily from two interrelated factors: the dominance of quantum mechanical effects and the substantial increase in the surface-area-to-volume ratio. Together, these factors render nanomaterials exceptionally reactive, both chemically and physically, opening avenues that conventional materials cannot offer.

The interdisciplinary nature of nanotechnology, which bridges physics, chemistry, biology, and materials engineering, has catalyzed significant advances across multiple sectors. In electronics, it has enabled the fabrication of faster and more compact integrated circuits. In medicine, it has contributed to improved diagnostic tools and targeted therapeutic strategies. In aerospace and energy, it has facilitated the development of high-performance, lightweight materials alongside more sustainable energy solutions.

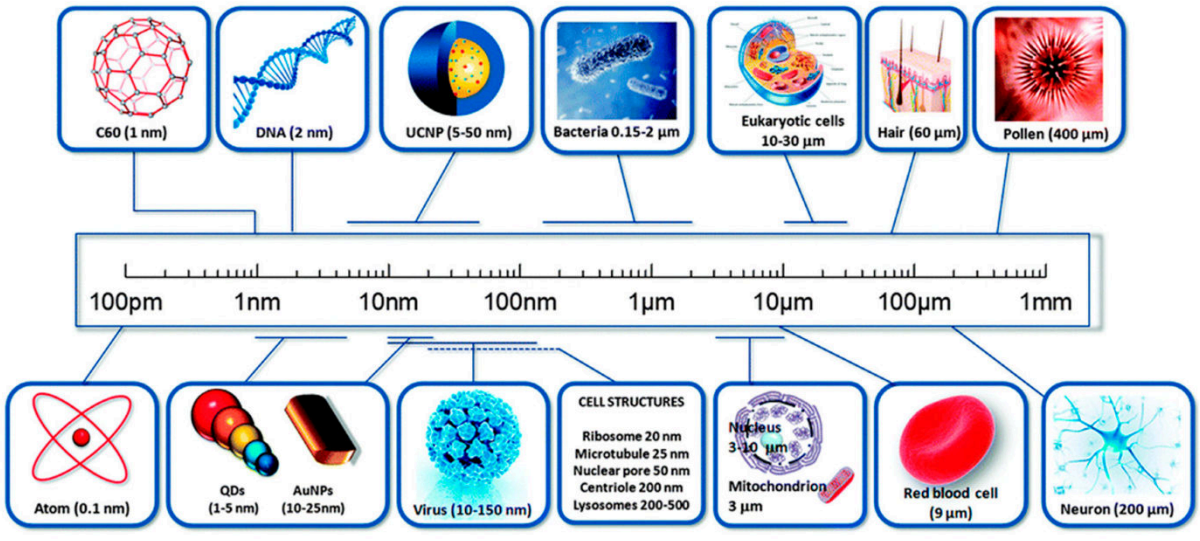

Figure (I.1): *Comparative size chart highlighting the nanometric scale (1–100 nm) relative to various biological structures, with reference dimensions defining the micro and nano ranges* [2].

I.1.1. History

Nanomaterials are by no means a recent phenomenon; their existence predates human civilization by millions of years. Natural processes such as volcanic activity, forest fires, and radioactive decay have continuously introduced nanoscale structures into the environment long before any human intervention. Although early human populations interacted with and made practical use of nanomaterials without conscious awareness, it is only through the advent of advanced characterization techniques that scientists have been able to trace their origins and assess their implications for human health and environmental integrity [3, 4].

The trajectory of nanotechnology, as depicted in **Figure (I.2)**, reflects a gradual and cumulative evolution stretching from antiquity through the medieval period and into the contemporary era. Ancient and medieval craftsmen, unknowingly exploited nanoscale phenomena in the production of colored glass, ceramics, and metallic alloys, achieving effects that modern science has only recently been able to explain [3].

The turning point that is widely regarded as the foundation of modern nanotechnology came in 1959, when the physicist Richard Feynman delivered his seminal lecture entitled *"There's Plenty of Room at the Bottom."* This landmark address articulated, for the first time, the theoretical possibility of manipulating matter at the atomic scale, thereby laying the conceptual groundwork for the rapid scientific developments that would follow throughout the 1960s and beyond.

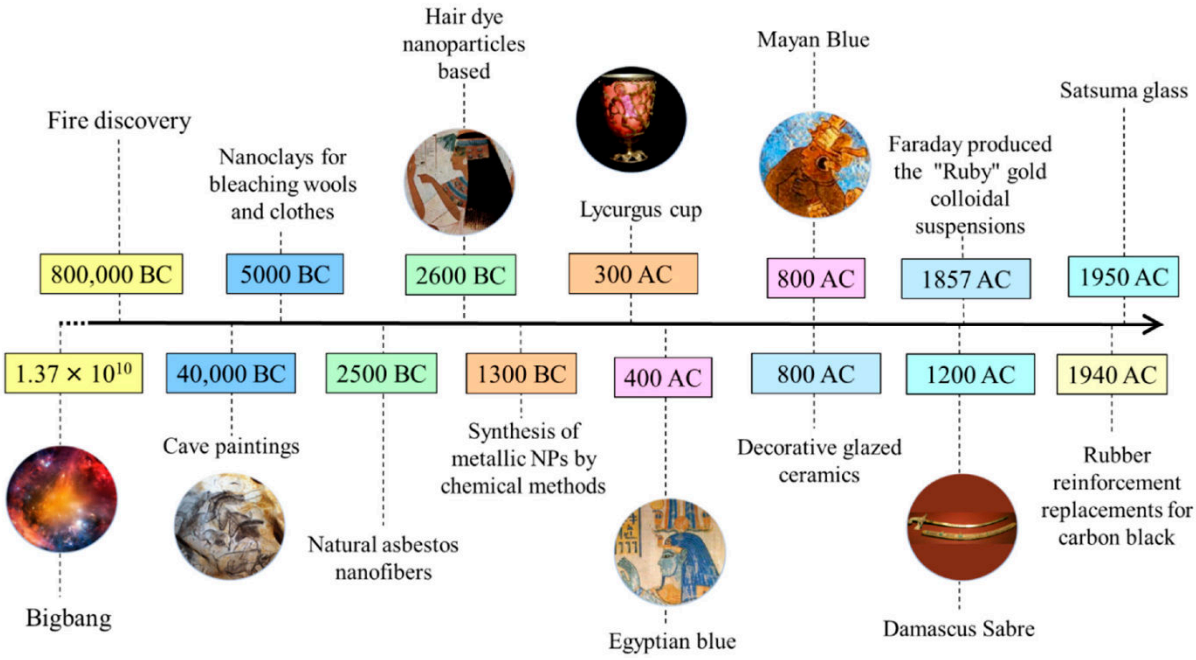

Figure (I.2): *Timeline illustrating the historical progression of nanomaterial use across civilizations, from early empirical applications in ancient societies to the emergence of modern nanotechnology, highlighting the absence of nanoscale awareness in early periods* [3].

I.1.1.1. Prehistoric Nanomaterials: Ancestors' Instinctive Touch with the Nanoscale

Humanity's connection to nanomaterials goes back much further than the 1990s, when the word "nanotechnology" finally entered everyday language thanks to new imaging tools. In reality, our early ancestors were already working with these tiny structures at the very start of human culture [5].

Everything began with the control of fire roughly 800,000 years ago. The smoke and soot rising from those ancient fires carried complex carbon forms—fullerenes, graphene sheets, and carbon nanotubes—that our forebears unknowingly turned into the first artistic tools. Far from being simple waste, these materials helped shape some of humanity's earliest creative expressions, as shown in **Figure (I.3)**.

Figure (I.3): *Cave paintings and hand stencils from Chauvet-Pont-d'Arc in France and Sulawesi in Indonesia, where carbon-based nanostructures gave ancient artists exceptional depth and durability. © MCC/DRAC. Open Access* [3].

I.1.1.2. Nanomaterials Through the Lens of Ancient History

Long before the term "nanotechnology" was ever coined, ancient peoples were unknowingly working with nanoscale materials in remarkably sophisticated ways. Both the Greeks and Egyptians, for instance, incorporated nanostructured compounds into cosmetic preparations, most notably in the formulation of hair-coloring products that contained nanoscale particles (**Figure (I.4)-A**). Among the most celebrated achievements of ancient materials science is the development of what scholars now call "Egyptian blue," a synthetic colorant that dates back to the third millennium BC. This pigment was produced through a carefully controlled mixture of glass and quartz, resulting in a finely structured material with distinct optical properties (**Figure (I.4)-B**) [6].

The use of naturally occurring nanomaterials extends even further back in history, with evidence suggesting their exploitation as early as 5000 BC. Across the Atlantic, the Maya civilization independently developed their own range of pigment formulations, among them a

vivid blue hue — though it is worth noting that the compositional and structural characteristics of Egyptian blue set it apart from comparable pigments produced by other cultures across Europe and Asia. Meanwhile, historical and archaeological records point to the deliberate use of metallic nanoparticles by craftsmen in both Mesopotamia and Egypt during the twelfth and fourteenth centuries BC.

Perhaps the most widely cited illustration of ancient nanotechnology is found in Roman glassmaking. The Lycurgus Cup, a remarkable artifact from the fourth century AD, was crafted from what is known as dichroic glass — a material that owes its extraordinary color-shifting behavior to the presence of embedded metallic nanoparticles. Depending on whether light passes through the glass or reflects off its surface, the cup transitions between distinctly different hues, a phenomenon that modern science now attributes to plasmonic interactions at the nanoscale.

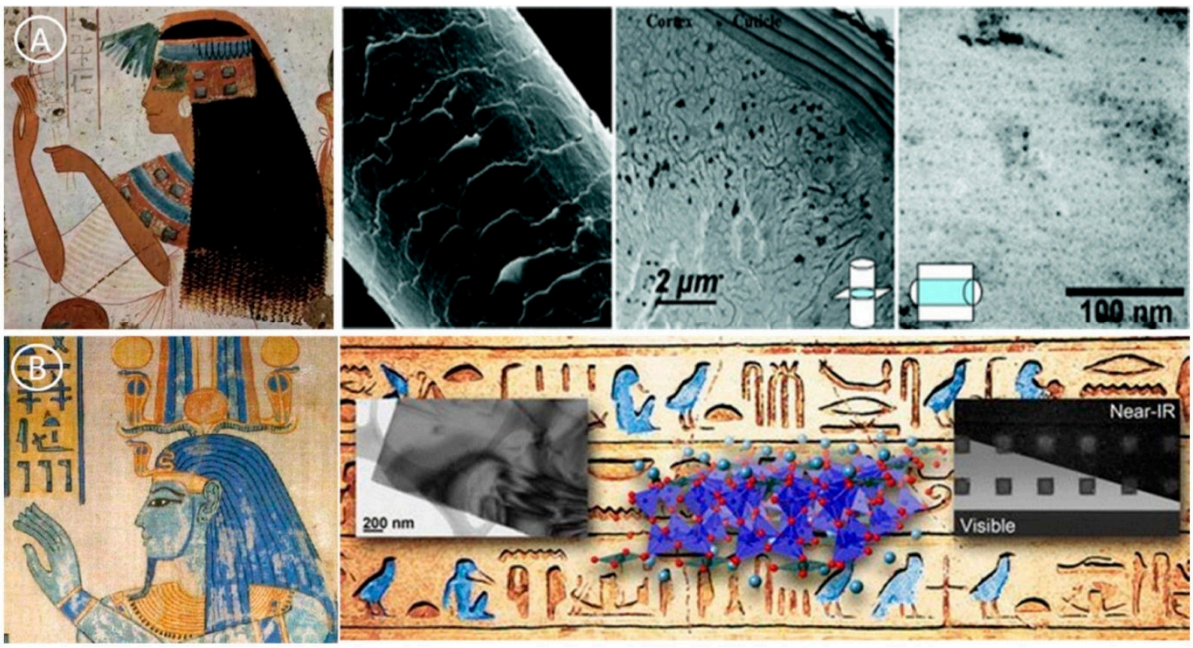

Figure (I.4): *Examples of nanostructured materials created in ancient times: (A) Hair dye formulated by ancient Egyptians using palladium sulfide nanoparticles (PdS_2 NPs) [7]; (B) Egyptian blue pigment (composed of $CaCuSi_4O_{10}$ and SiO_2 nanosheets with thickness below 5 nm) synthesized by ancient Egyptian craftsmen* [8].

I.1.1.3. Nanotechnology Before Its Time: The Medieval Era

The legacy of Roman craftsmanship in working with nanoscale materials represents one of the most compelling early chapters in the history of nanotechnology. A defining example is the Lycurgus Cup (**Figure (I.5)-A**), widely recognized as the earliest known artifact made from dichroic glass. What makes this object particularly extraordinary is its ability to display two entirely different colors depending on how light interacts with it — appearing green under direct illumination and shifting to a deep red-purple when light is transmitted through it from behind [9]. Modern analytical techniques, including electron microscopy and X-ray diffraction (XRD), have since confirmed that this remarkable optical behavior arises from gold and silver nanoparticles embedded within the glass matrix, with particle diameters typically falling in the range of 50 to 100 nm.

The medieval Islamic world also demonstrated a sophisticated, if unintentional, command of nanoscale phenomena. Lustrous ceramic wares produced across Islamic regions were long admired for their distinctive metallic sheen, and elemental analyses of these decorative glazes have revealed the presence of finely dispersed silver and copper nanoparticles responsible for that visual effect. Another striking example comes from the field of medieval metallurgy: Damascus steel, which was widely used from the thirteenth century onward to forge high-performance blades, has been found to contain embedded carbon nanowires that contributed significantly to its legendary mechanical strength and resilience (**Figure (I.5)-B**) [4].

Figure (I.5): *Selected examples of handcrafted nanomaterial-based artifacts from the medieval period.* ***(A)*** *The Lycurgus Cup, which glows red when backlit, owes its color-changing property to an embedded Au-Ag nanoparticle alloy within the glass* [10, 11]*;* ***(B)*** *A blade forged from*

Damascus steel, whose internal nanostructure underpins its renowned durability (photograph by Tina Fineberg for The New York Times).

I.1.1.4. From Discovery to Innovation: Nanomaterials in the Modern Era

The puzzling properties observed in many ancient artifacts eventually drew the attention of modern scientists, compelling them to look more closely at the materials behind these phenomena. A pivotal moment came in 1857, when Michael Faraday undertook a systematic investigation into colloidal gold solutions — what was then referred to as "ruby" gold — and demonstrated that gold nanoparticles were capable of altering the perceived color of a liquid medium under particular lighting conditions [12]. This work laid important groundwork for understanding the optical behavior of metallic nanoparticles at the submicron scale.

Decades later, in the 1940s, silica-based nanoparticles entered industrial application as reinforcing agents in rubber manufacturing, offering a viable substitute for carbon black in improving the mechanical properties of the material. The field then received a defining intellectual impulse on December 29, 1959, when Richard Feynman delivered his now-legendary lecture, "There's Plenty of Room at the Bottom," at the annual meeting of the American Physical Society. That address is broadly regarded as the conceptual birth of what would later be formalized as "nanotechnology." Around the same period, in the early 1960s, a small but forward-thinking community of researchers — Richard Zsigmondy among them — introduced the term "nanometer" as a precise unit for characterizing the dimensions of colloidal gold particles, while simultaneously speculating about the long-term scientific possibilities that nanoscale research might unlock.

The trajectory of discovery that followed has been both rapid and wide-ranging, as illustrated in **Figure (I.6)**, which traces the key milestones in nanomaterial development throughout the modern nanotechnology era [4].

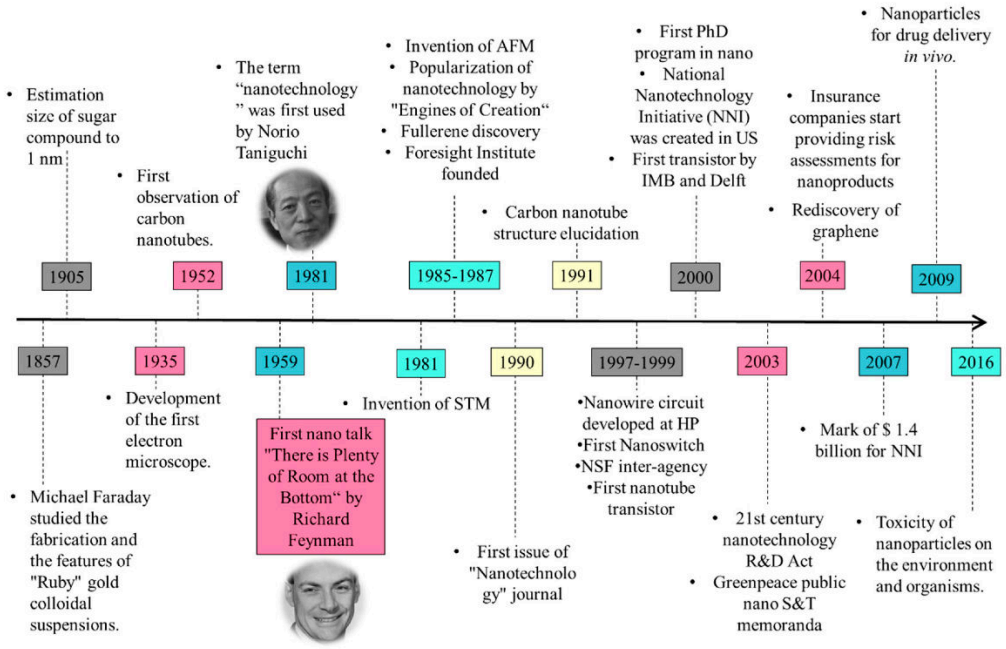

Figure (I.6): *A chronological overview of major nanomaterial discoveries across the modern nanotechnology period* [3].

I.1.2 Terms Related to Nanotechnology

The prefix "nano," rooted in the Greek word for dwarf, serves as the foundation for a broad and interconnected family of scientific concepts. In an effort to standardize the language used across disciplines, the International Organization for Standardization (ISO) has formally defined nanomaterials as substances possessing at least one internal or external dimension that falls within the nanoscale range. **Table (I.1)** below presents a structured overview of the principal terms associated with the nano domain [1].

Table (I.1): Key terminology used in the field of nanotechnology and their corresponding definitions.

Term	Size Range and Definition
Nanoscale	Refers to the dimensional range spanning from 1 to 100 nm
Nanoscience	The scientific discipline concerned with studying and understanding matter at the nanoscale, where materials exhibit properties fundamentally distinct from those observed in their bulk counterparts
Nanotechnology	A field of applied science and engineering focused on designing, developing, and controlling materials, devices, and systems at the nanoscale
Nanomaterial	Any material in which at least one dimension lies within the 1 to 100 nm range
Nano object	A discrete material unit possessing one, two, or three external dimensions at the nanoscale
Nanoparticle	A nano object in which all three spatial dimensions fall within the nanoscale range
Nanofibre	A nano object characterized by two dimensions in the nanoscale while the third extends considerably beyond that range
Nanostructure	A material whose internal or surface architecture contains at least one discrete functional component residing in the nanoscale region
Nanocomposite	A multi-component, multiphase material system in which at least one constituent phase has a minimum of one nanoscale dimension
Nanorod	A material whose shortest and longest axes differ along their length, with a width between 1 and 100 nm and an aspect ratio greater than one
Nanowire	Structurally analogous to a nanorod, but distinguished by a significantly higher aspect ratio
Nanosphere	A nanoparticle characterized by a uniform aspect ratio of 1, indicating an essentially spherical geometry
Nanotube	A hollow cylindrical nanostructure, conceptually analogous to a nanofibre with an empty interior
Nanostructured material	A material whose architecture is assembled from elements, molecules, crystallites, or clusters operating at the nanoscale
Engineered nanomaterials	Intentionally manufactured materials of anthropogenic origin, with one or more dimensions deliberately engineered to fall within the 1–100 nm range
Nanomanufacturing	The process of fabricating nanoscale materials and structures through either top-down or bottom-up production strategies

I.1.3. Metallic Nanoparticles

I.1.3.1. Nanoparticles

Nanoparticles occupy a fascinating intermediate position in the material world, sitting at the boundary between bulk matter and individual atoms, and it is precisely this position that grants them their exceptional versatility. Generally defined as solid particles with dimensions falling between 10 and 1000 nm, they have attracted considerable attention in biomedical research owing to their capacity to encapsulate or bind therapeutic agents, enabling their transport through the human body with a high degree of spatial and temporal control [13]. Their ability to modify both pharmacokinetic and pharmacodynamic profiles means that drug molecules carried by nanoparticles are effectively shielded from premature degradation within systemic circulation while being delivered to target sites in a controlled and sustained manner.

In terms of structural design, nanoparticles can be engineered in different configurations depending on the intended application. Nanocapsules, for instance, provide a protective shell around a sensitive payload, while nanospheres allow for more uniform distribution of an embedded compound. The preparation of these structures relies on well-established physicochemical methods such as solvent evaporation and ionic gelation [14]. Beyond the biomedical domain, nanoparticles are finding growing utility in industrial settings, where their large surface-area-to-volume ratio and distinctive quantum-level behavior are exploited in applications ranging from corrosion-resistant marine coatings to thermally active textile systems. Nevertheless, ensuring long-term colloidal stability — typically assessed through zeta potential measurements — and thoroughly evaluating the potential biological and environmental consequences of widespread nanoparticle use remain open and pressing challenges for the research community [15].

I.1.3.2. Metallic Nanoparticles

Taking their etymological roots from the Greek word *nanos*, meaning dwarf, metallic nanoparticles represent a class of precision-engineered materials whose dimensions are deliberately confined to the 1–100 nm range. Within this scale, they exhibit optical, magnetic, and mechanical characteristics that differ markedly — and often dramatically — from those of their macroscopic equivalents, a divergence that underlies much of their scientific and technological appeal.

Their fabrication generally follows one of two overarching strategies. Top-down approaches begin with bulk material and progressively reduce it to the nanoscale through physical processes such as mechanical milling or laser ablation. Bottom-up approaches, by contrast, build nanostructures from the atomic or molecular level upward, assembling precursor units into stable nuclei through carefully controlled chemical reactions. Given the growing concerns around the financial cost and ecological footprint of conventional chemical synthesis routes, there has been a marked shift in the field toward greener alternatives. These environmentally conscious methods draw on biological systems — including bacteria, fungi, and plant-derived extracts — as natural reducing and stabilizing agents, converting metal ions into well-defined nanoparticles without relying on harsh reagents.

The resulting materials are finding application across a remarkably broad spectrum of disciplines. In medicine, they are being investigated for targeted cancer treatment and controlled drug delivery. In materials science, they are enabling the development of antimicrobial textiles and functional coatings. In environmental engineering, they are contributing to sustainable approaches in agriculture and wastewater remediation [16–18].

I.1.3.2.1. Advantages of Metallic Nanoparticles

Metallic nanoparticles offer a wide and compelling range of benefits that span multiple scientific and industrial domains. In oncology, their small size and surface tunability allow therapeutic agents to be directed with considerable precision toward malignant tissue, substantially reducing the collateral toxicity that typically accompanies conventional systemic treatments. From a catalytic standpoint, their exceptionally high surface-to-volume ratio translates into an abundance of accessible active sites, enabling reaction efficiencies that far surpass those achievable with bulk catalysts.

In pharmaceutical applications, metallic nanoparticles function as adaptable carriers that enhance the solubility and bioavailability of poorly soluble drug compounds, ultimately improving therapeutic outcomes for patients. In the realm of structural materials, their incorporation into metal matrix composites promotes grain refinement and activates Orowan reinforcement mechanisms, collectively imparting superior mechanical durability and resistance to creep deformation under prolonged stress.

Their optical properties are equally noteworthy. The Surface Plasmon Resonance (SPR) phenomenon exhibited by many metallic nanoparticles has been harnessed to develop highly sensitive detection platforms and advanced bioimaging tools, opening new possibilities in both clinical diagnostics and fundamental biological research. On the industrial sustainability front, when metallic nanoparticles are integrated into supported heterogeneous catalyst systems, they can be recovered and reused with relative ease, contributing to more resource-efficient and environmentally responsible manufacturing processes.

In biomedical engineering, their structural resemblance to natural biological architectures enhances their compatibility with living tissue, making them particularly promising candidates for improving the performance and longevity of dental and orthopedic implants. Finally, their capacity to serve as stable drug-release platforms — protecting bioactive compounds from premature breakdown and enabling sustained, controlled delivery over time — positions them as valuable tools in the design of next-generation therapeutic systems [19–21].

I.1.3.2.2. Disadvantages of Metallic Nanoparticles

While metallic nanoparticles hold considerable promise, several important limitations must be acknowledged.

Their high surface energy renders them thermodynamically unstable, making them prone to agglomeration over time. This tendency to cluster compromises their structural integrity and diminishes the overall performance of the materials in which they are used [22].

Biological safety is another pressing concern. Due to their ability to penetrate cellular membranes, these particles have been linked to toxic and potentially carcinogenic effects, including the generation of harmful reactive oxygen species that can induce oxidative damage within living tissues [26].

From a manufacturing perspective, producing metallic nanoparticles demands substantial investment and specialized infrastructure. Achieving reproducible particle size distributions in solution remains technically challenging, and the risk of environmental contamination during synthesis is difficult to eliminate entirely [23].

Finally, practical handling of these materials carries physical and environmental risks. Certain synthesis conditions can trigger exothermic reactions with explosive potential, while many conventional production routes rely on toxic chemical precursors that pose broader ecological concerns [24].

I.1.3.3. Catalytic Role of Metal Nanoparticles in Chemical Reactions

Metal nanoparticles bridge the gap between homogeneous and heterogeneous catalysis, combining high selectivity with thermal stability and easy recovery. Their nanoscale dimensions maximize active surface area, enhancing reactivity. However, their tendency to agglomerate remains a key challenge, addressed through stabilizing agents such as N-heterocyclic carbenes (NHCs), which provide effective electronic and steric protection.

Encapsulating nanoparticles within porous host materials — particularly zeolites and metal-organic frameworks (MOFs) — further improves their durability and introduces shape-selective control over reaction outcomes.

Their practical applications span two important areas. In synthetic chemistry, they facilitate carbon-carbon coupling reactions at minimal catalyst loadings, while in environmental applications, they contribute to the catalytic reduction of NOx pollutants. Together, these capabilities establish metal nanoparticles as essential tools in advancing green and sustainable chemistry [25–27].

I.1.3.4. Multidisciplinary Applications of Metallic Nanoparticles

Metallic nanoparticles have established a strong presence across a broad spectrum of applied fields. In medicine, they serve as precision-guided platforms for cancer cell detection — using tools such as NanoFlares — and as targeted drug delivery vehicles capable of transporting therapeutic agents directly to diseased tissues [28].

In industry, their protective properties are exploited in antifouling and anticorrosion coatings applied to marine infrastructure, while their thermal characteristics are utilized in self-heating textile systems integrated into automotive interiors. Aviation safety has also benefited from their incorporation into smart de-icing coatings designed to prevent ice accumulation on aircraft surfaces [29].

On the environmental front, metallic nanoparticles demonstrate notable efficiency in wastewater treatment, facilitating the removal of organic contaminants and heavy metal ions from

polluted water sources. Their utility extends further into healthcare, where they support dental enamel reinforcement and bone tissue regeneration, and into agriculture, where nano-pesticide formulations offer more targeted and resource-efficient crop protection strategies [30].

Taken together, these diverse applications underscore the transformative role that metallic nanoparticles are playing in building more efficient and sustainable technological solutions across multiple sectors.

I.1.4. Functional Characteristics of Nanomaterials

Nanomaterials, defined by dimensions spanning the 1–100 nm range, display physical and chemical characteristics that differ substantially from those of their bulk equivalents. These distinctive behaviors arise from the interplay of three fundamental factors: reduced particle size, elevated surface-to-volume ratio, and quantum mechanical effects. The sections below address the most significant of these properties [31].

I.1.4.1. Nanomaterials as Catalytic Agents

Catalysis occupies a central position in modern chemistry, underpinning the efficient conversion of raw materials — such as petroleum and natural gas — into valuable chemical products, while simultaneously reducing energy consumption and minimizing waste generation. The field has evolved considerably over the past century, and the search for increasingly active and durable catalysts remains an active area of investigation.

Catalysts are broadly divided into two categories: homogeneous catalysts, which operate in the same phase as the reactants as soluble molecular complexes, and heterogeneous catalysts, which exist as solid particles anchored to a support material. While homogeneous systems offer superior substrate accessibility and enhanced selectivity, their separation from reaction products presents a practical challenge. Heterogeneous systems, by contrast, simplify product isolation but may sacrifice some degree of catalytic precision [32].

Nanocatalysis has emerged as a compelling middle ground, combining high activity with structural tunability. The nanoscale dimensions, morphology, and large surface-to-volume ratio of nanocatalysts endow them with properties unattainable in conventional bulk catalysts. Materials such as clays, silica, titanium dioxide, iron, and aluminum have long been used at the

nanoscale in catalytic applications, yet the full mechanistic picture behind their remarkable activity remains an open scientific question [33].

Heterogeneous nanocatalysis has attracted particularly intensive research interest, encompassing reactions such as hydrogenation and oxidation carried out over noble metal catalysts — including gold, silver, and platinum — as well as metal oxides such as ZnO, Fe_2O_3, and TiO_2. Wang et al. (2019) [34] demonstrated that platinum-based nanoparticles supported on carbon nanotubes exhibited superior catalytic performance in the selective hydrogenation of nitroaromatic compounds, attributed to their high dispersion and strong metal-support interaction.

Nanomaterials also play an increasingly important role in electrochemical energy systems, including fuel cells, batteries, and electrolyzers, where they catalyze interfacial reactions at electrode surfaces. Zhu et al. (2021) [35] reported that cobalt oxide nanoparticles supported on nitrogen-doped carbon nanotubes displayed enhanced electrocatalytic activity toward oxygen reduction in alkaline media, highlighting the potential of nanomaterial-based electrodes to improve device efficiency [36]. More broadly, the integration of nanoparticles into industrial catalytic processes offers meaningful reductions in energy demand and waste output, contributing to more environmentally responsible chemical manufacturing [33].

I.1.4.2. Nanomaterial-Based Antimicrobial Activity

The treatment of bacterial, viral, fungal, and parasitic infections has historically relied on antibiotics and related antimicrobial agents. However, the rapid emergence and spread of antimicrobial-resistant pathogens has become one of the most pressing challenges in contemporary medicine, a concern further amplified by the vulnerabilities exposed during recent global health crises.

In this context, nanoparticles have attracted growing interest as a viable alternative or complement to conventional antimicrobial therapies [37]. Metallic, polymeric, lipid-based, and carbon-derived nanoparticles share the capacity to generate reactive oxygen species — including superoxide ions and hydroxyl radicals — that disrupt bacterial membranes and inhibit essential enzymatic functions, thereby neutralizing antibiotic-resistant strains. Their small size and distinctive physical characteristics further enable them to penetrate and disrupt biofilm structures, addressing one of the most persistent obstacles in treating chronic bacterial infections.

Beyond direct bactericidal action, nanoparticles are being integrated into a wide range of clinical and biomedical applications, including antimicrobial coatings for implantable devices, wound-healing materials, bacterial detection platforms, and targeted antibiotic delivery systems. **Figure (I.7)** provides an overview of the principal categories of antibacterial nanoparticles currently under investigation [38].

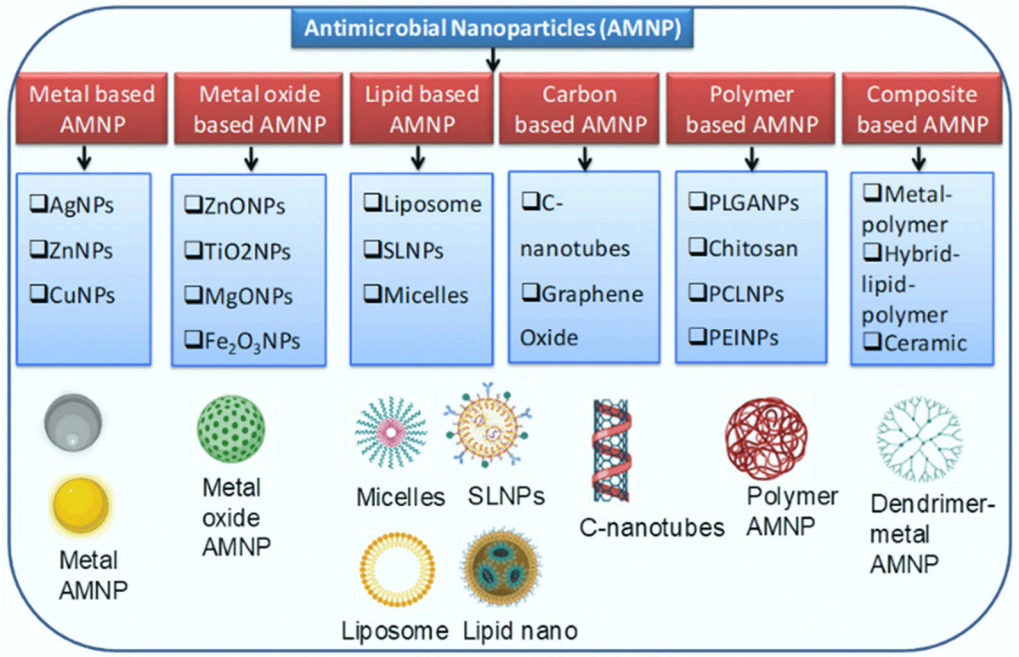

Figure (I.7): *Classification of antimicrobial nanoparticles and their structural representations* [39].

The enlarged surface area intrinsic to nanoparticles plays a key role in amplifying their antibacterial efficacy, as it increases the capacity for drug loading and improves direct contact with bacterial cell surfaces. **Figure (I.8)** summarizes the principal mechanisms through which nanoparticles exert their bactericidal effects [38].

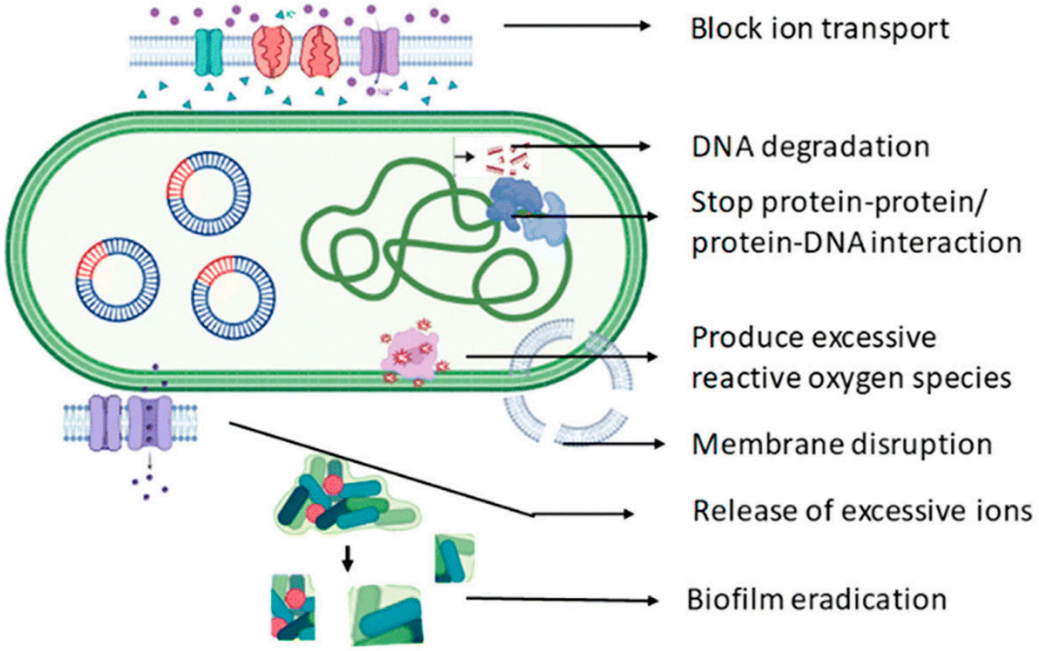

Figure (I.8): *Mechanisms underlying the bactericidal activity of nanoparticles against microbial cells* [39]. *with permission from the Royal Society of Chemistry*

I.1.4.3. Light Interaction and Optical Behavior of Nanoparticles

The way nanoscale materials interact with light has fundamentally reshaped our understanding of modern photonics. When material dimensions are reduced below 100 nm, physical properties no longer behave as fixed bulk constants — they become sensitive functions of particle size, shape, and the surrounding dielectric environment [40, 41].

For spherical nanoparticles, Mie theory (1908) remains the principal analytical framework for describing scattering and absorption behavior [42]. A particularly striking optical phenomenon observed in noble metal nanoparticles — such as gold and silver — is Surface Plasmon Polariton (SPP) resonance, arising from the collective oscillation of conduction electrons. This mechanism produces well-defined spectral peaks that govern the perceived color of the material. When particles adopt anisotropic shapes, such as nanorods or spheroids, these resonances split into distinct longitudinal and transverse modes, a property that has been exploited in the design of tunable optical filters and polarizers [43, 44].

At higher light intensities, nonlinear optical behavior becomes relevant. Under intense laser radiation, a material's polarization response deviates from simple linearity and involves

higher-order terms, most notably the third-order nonlinear susceptibility ($\chi^{(3)}$). These nonlinear effects form the physical basis for technologies such as all-optical switching and optical limiting — systems that attenuate intense laser pulses while remaining transparent to low-intensity ambient light, thereby protecting both human eyes and sensitive optical instruments. The Z-scan technique, introduced in 1989, remains the primary method for quantifying these parameters. As shown in **Figure (I.9)**, it involves translating a sample along the optical axis through the focal point of a Gaussian laser beam and monitoring the normalized transmittance to extract the nonlinear refractive index and absorption coefficient.

At very small particle sizes, quantum size effects (QSE) emerge as electrons become spatially confined, causing energy levels to discretize. In semiconductor quantum dots such as CdSe, this confinement progressively widens the bandgap as particle size decreases, producing a characteristic blue-shift in photoluminescence. These properties are actively harnessed through techniques like ion implantation to develop ultrafast optoelectronic devices capable of operating well beyond the speed limits of conventional electronics [45, 46].

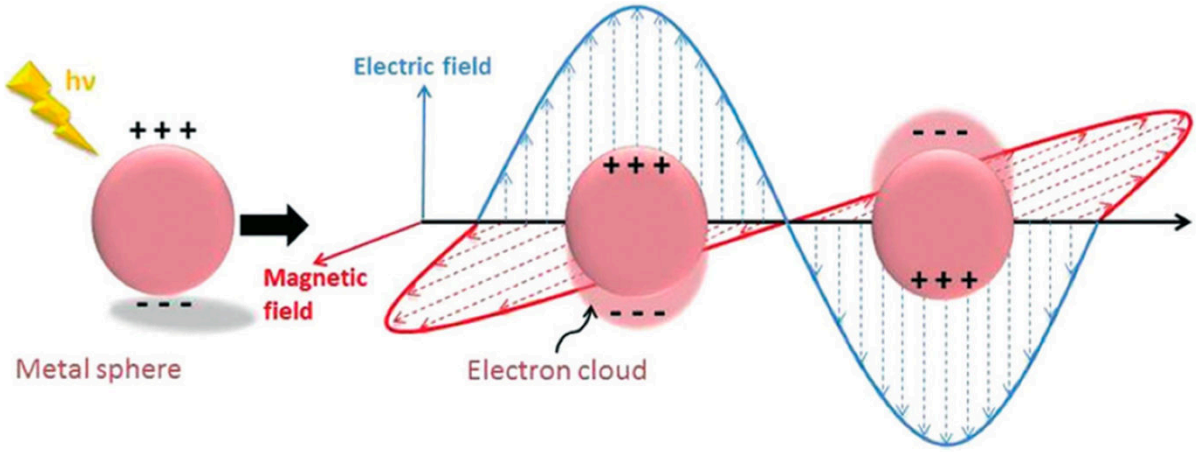

Figure (I.9): *Schematic illustration of localized surface plasmon resonance (LSPR) in metallic nanoparticles* [47].

I.1.4.4. Photocatalytic Mechanisms and Applications of Nanoparticles

Photocatalysis has emerged as a powerful and sustainable strategy for environmental remediation, harnessing solar energy to drive advanced oxidation processes (AOPs) capable of completely mineralizing hazardous organic pollutants into harmless end products such as CO_2

and H_2O [48]. Unlike conventional treatment methods that simply transfer contaminants from one phase to another, photocatalysis offers a pathway to their total elimination.

The underlying mechanism centers on the electronic dynamics of semiconductor nanoparticles under illumination. When incident photons carry energy exceeding the material's bandgap, electrons are promoted from the valence band (VB) to the conduction band (CB), generating reactive electron-hole pairs (e^-/h^+). As illustrated in **Figure (I.10)**, these photogenerated carriers may follow several competing pathways: becoming trapped at surface defect sites, recombining radiatively or non-radiatively, or migrating to the particle surface to participate in redox reactions with adsorbed species [49, 50]. The overall photocatalytic efficiency is governed by the balance between productive interfacial charge transfer and undesired carrier recombination.

The quantum size effect plays a defining role in nanoscale photocatalysis. As semiconductor particles shrink below a critical threshold — often below 10 nm for TiO_2 — spatial confinement causes energy bands to split into discrete states, widening the bandgap and inducing a blue-shift in optical absorption. Crucially, this also enhances the redox potential of charge carriers, enabling reactions that are thermodynamically inaccessible in bulk materials [55].

Titanium dioxide (TiO_2) remains the benchmark photocatalyst owing to its chemical stability and low toxicity, though its performance varies across crystal phases. The anatase polymorph is generally regarded as the most active, as its indirect bandgap allows longer charge carrier lifetimes and greater mobility relative to rutile or brookite [51, 52]. Recent advances have produced black TiO_2 variants that exploit surface defects and oxygen vacancies to extend light absorption into the visible and infrared regions [53].

Beyond TiO_2, other metal oxide nanostructures are attracting increasing attention. Magnesium oxide (MgO) nanoparticles synthesized via combustion methods, with an average size of approximately 27 nm and a bandgap of 2.9 eV, have demonstrated a degradation efficiency of 75% for methylene blue dye within 120 minutes of UV irradiation. These developments collectively reflect the growing capacity of nanotechnology to address critical global challenges, particularly in the area of water purification [53].

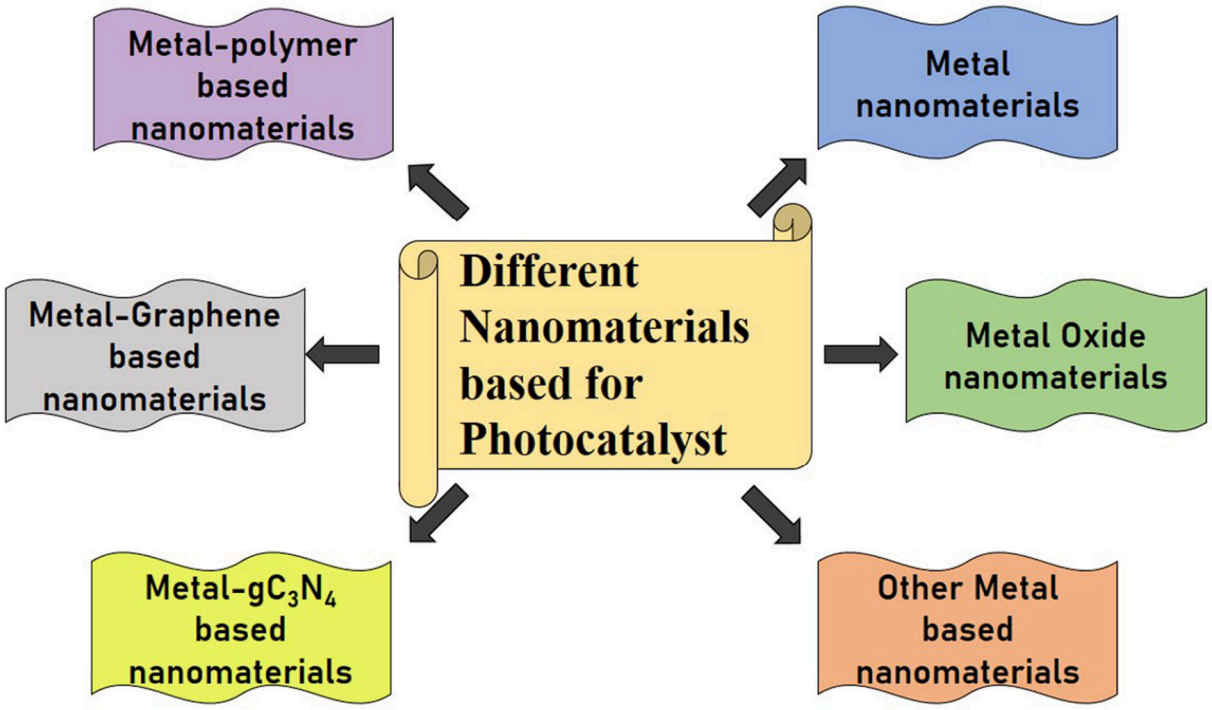

Figure (I.10): *Categories, structures, and recent developments in advanced nanomaterials used as photocatalysts* [54].

I.2. Types and Classification of Nanomaterials

Nanomaterials can be organized into several broad categories based on different classification criteria, regardless of their chemical composition or physical location.

I.2.1. Origin-Based Classification of Nanomaterials

From an academic standpoint, nanomaterials are grouped into four distinct classes according to their origin [55]. Natural nanomaterials arise spontaneously through biogeochemical cycles and include minerals and viruses. Incidental nanomaterials are unintended anthropogenic by-products generated through combustion processes or industrial waste streams [56]. Engineered nanomaterials, by contrast, are deliberately synthesized to achieve specific technical properties, while bioinspired nanomaterials are designed to replicate the architecture of natural structures in order to perform sophisticated functions [57].

I.2.2. Structure and Composition-Based Classification of Nanomaterials

The architectural makeup of nanomaterials is a primary determinant of their practical utility, and on this basis they can be organized into four principal families.

Organic nanomaterials rely on carbon-based molecular frameworks to construct structures such as liposomes and dendrimers. Their inherent biocompatibility, low toxicity, and biodegradability make them particularly well-suited as carriers in precision medicine applications [58, 59], as illustrated in **Figure (I.11)**.

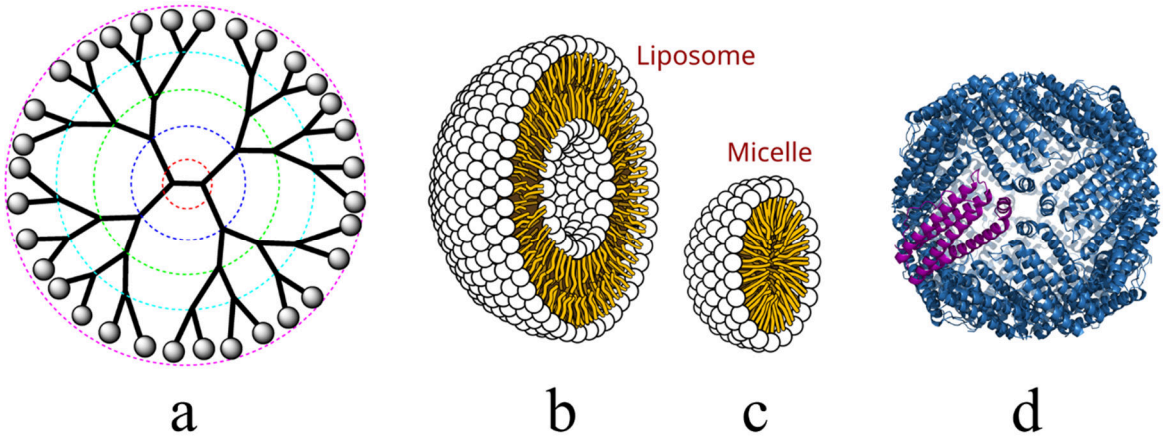

Figure (I.11): *Representative examples of organic nanomaterials: (a) dendrimers, (b) liposomes, (c) micelles, and (d) ferritin* [59].

Inorganic nanomaterials, which contain no carbon backbone, are typically composed of metals such as silver or metal oxides such as TiO_2. They are valued primarily for their exceptional catalytic activity and potent antibacterial properties [59].

Carbon-based nanomaterials — encompassing graphene, carbon nanotubes, and fullerenes — occupy a distinctive category owing to their extraordinary mechanical strength, which surpasses that of steel, combined with high thermal and electrical conductivity [60, 61].

Finally, composite nanomaterials offer a flexible hybrid approach, integrating different nanoparticles with bulk matrices to enhance properties such as mechanical durability and flame resistance. This structural diversity enables nanotechnology to address a wide spectrum of challenges, ranging from targeted cancer therapy to high-performance engineering applications [62].

I.2.3. Dimensionality-Based Classification of Nanomaterials

A widely adopted classification scheme organizes nanomaterials according to the number of dimensions that fall within the nanoscale range [63, 64].

Zero-dimensional (0D) materials, such as quantum dots, are confined to the nanoscale in all three spatial directions. One-dimensional (1D) materials, including nanotubes and nanowires, possess two nanometric dimensions while extending freely in the third [65]. Two-dimensional (2D) materials, of which graphene is the most prominent example, are restricted to the nanoscale in only one dimension, yielding planar sheet-like structures [66]. Three-dimensional (3D) bulk nanostructured systems, although exceeding 100 nm in overall size, are internally composed of nanoscale building blocks [67]. These distinctions are visually summarized in **Figure (I.12)**.

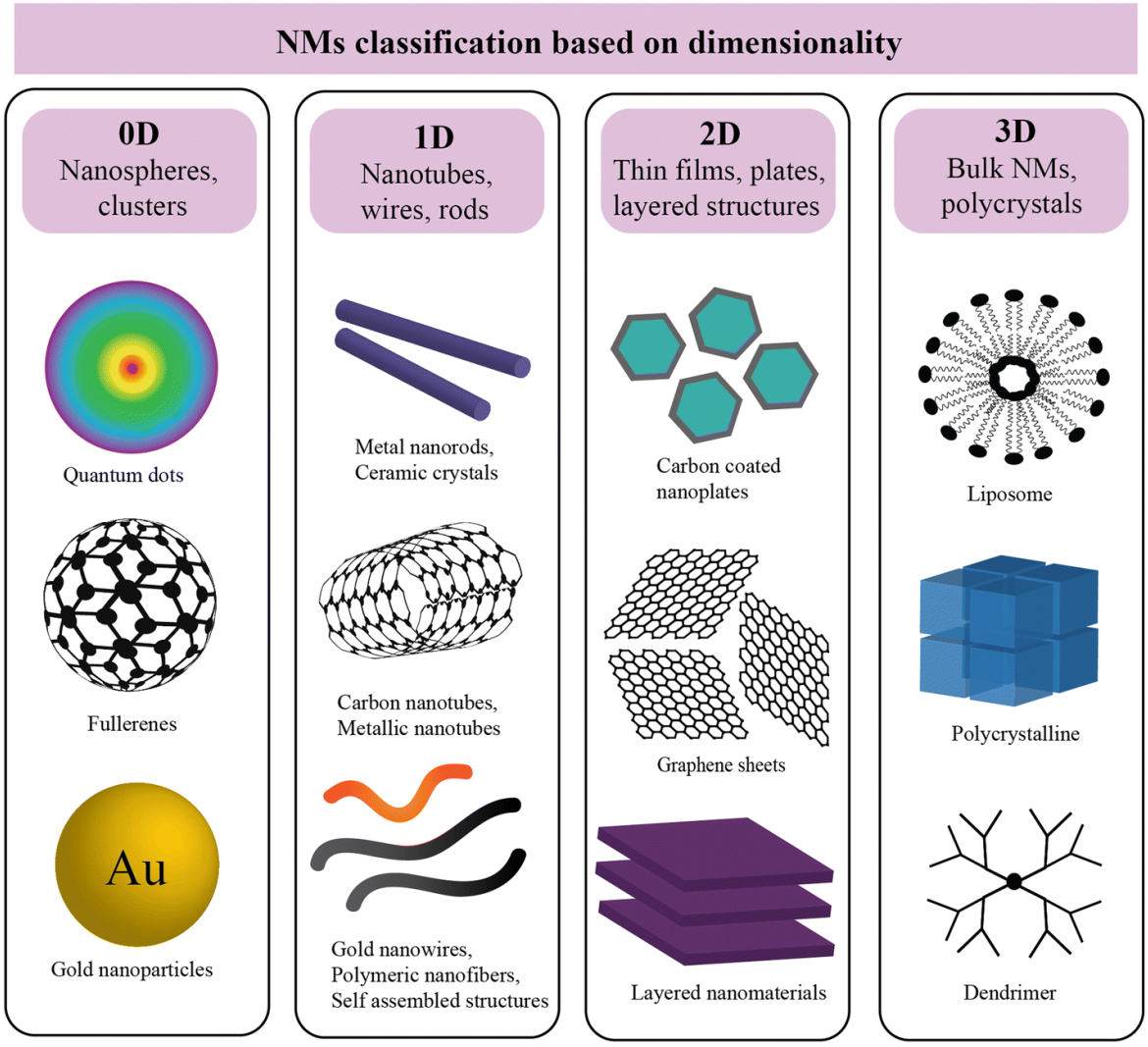

Figure (I.12): *Dimensional classification of nanostructured materials* [68].

I.2.4. Pore Size-Based Classification of Nanomaterials

In many nanomaterial systems, the internal void space is as functionally significant as the solid framework itself. Classifying nanomaterials by their pore dimensions provides a practical basis for tailoring them to specific applications such as drug delivery and heterogeneous catalysis.

Microporous materials occupy the finest end of the scale, with pore diameters typically below 2 nm [69]. Metal-organic frameworks (MOFs) and specialized zeolites are prominent examples, widely employed as molecular sieves in gas storage and petrochemical separation processes [70].

Mesoporous materials fall within the intermediate range of 2 to 50 nm [69]. Mesoporous silica nanoparticles (MSNs) are particularly notable in this category, offering large internal surface areas and highly tunable pore surfaces that make them effective vehicles for targeted drug delivery in cancer therapy [70].

Macroporous materials possess the largest void structures, with pore dimensions exceeding 50 nm and in some cases reaching the micrometer scale. These architectures find important applications in biotechnology and environmental engineering, and are often fabricated using specialized templating strategies such as Pickering emulsions to produce functional magnetic polymer systems [70].

Collectively, pore size classification serves as a practical guide for matching nanomaterial architecture to the demands of specific scientific and technological applications [70], as illustrated in **Figure (I.13)**.

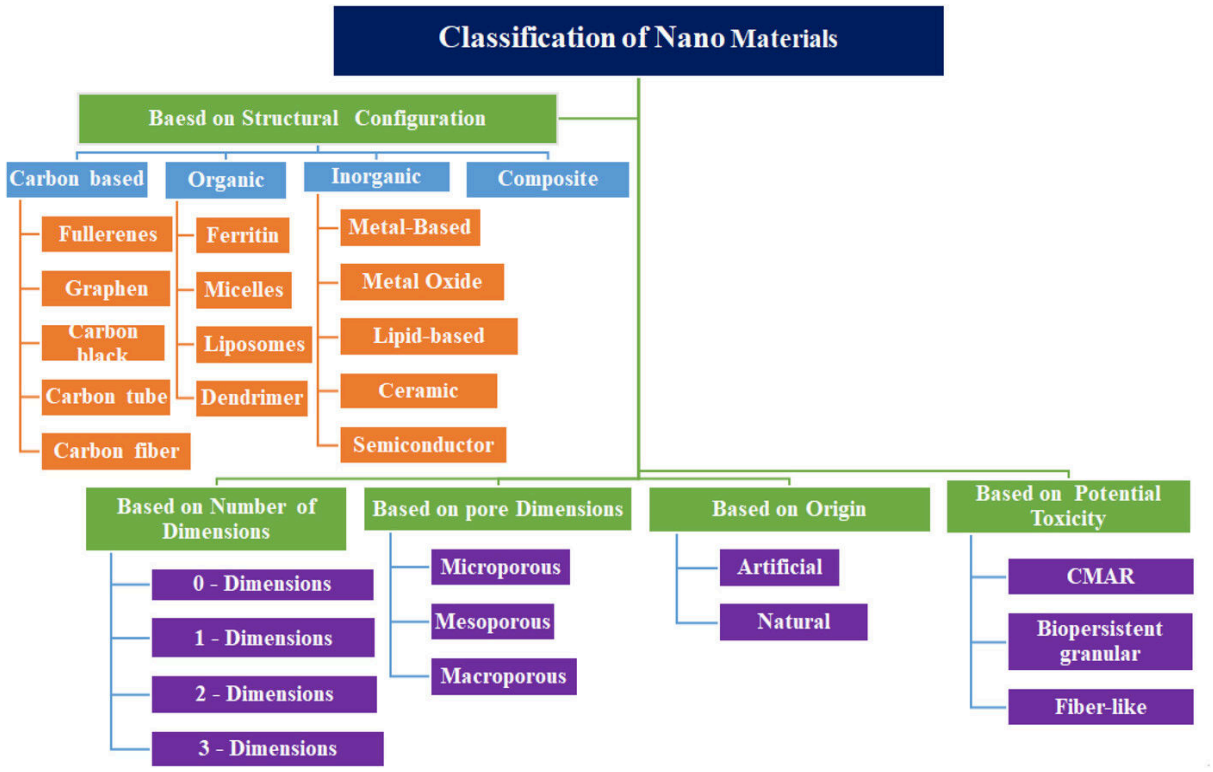

Figure (I.13): *Classification of nanomaterials based on pore dimensionality* [71].

I.3. Metallic Oxide Nanoparticles: Fundamentals and Biomedical Relevance

Among the most therapeutically significant metallic oxide nanoparticles are superparamagnetic iron oxide nanoparticles (Fe_3O_4), which have carved out a distinctive role in contemporary biomedical science. Their impact extends well beyond passive material behavior — they function as active diagnostic and therapeutic agents within the human body. By subtly perturbing the magnetic relaxation of surrounding water protons, they enhance the contrast resolution of MRI scans, effectively converting standard imaging into detailed, high-definition maps of pathological tissue [72].

Their versatility is equally remarkable. Through surface functionalization with biocompatible coatings such as polyethylene glycol (PEG) or dextran, these nanoparticles can be transformed into targeted delivery vehicles capable of transporting cytotoxic agents directly to tumor sites while minimizing exposure to healthy tissue [73, 74]. Applications range from stem cell tracking to the precision treatment of brain gliomas, positioning these materials at the intersection of diagnostics and therapy. Although concerns regarding potential neurotoxicity

warrant continued investigation, scalable fabrication methods such as chemical coprecipitation offer a viable route toward their integration into personalized medical strategies [73, 75].

I.3.1. Crystal Architecture and Structural Properties of Zinc Ferrite ($ZnFe_2O_4$)

Zinc ferrite ($ZnFe_2O_4$) adopts a normal cubic spinel structure of the XY_2O_4 type, crystallizing in space group $Fd\bar{3}m$ with a lattice parameter of a = 8.44 Å. Within this framework, oxygen anions occupy the 32e Wyckoff positions, forming a distorted face-centered cubic (FCC) sublattice in which the resulting interstices are partially filled by zinc and iron cations. Specifically, one-eighth of the available tetrahedral sites — designated as A-sites, corresponding to 8a Wyckoff positions — are occupied by divalent Zn^{2+} cations, while one-half of the octahedral sites — designated as B-sites, at 16d Wyckoff positions — are filled by trivalent Fe^{3+} cations, yielding the cation distribution $[Zn^{2+}]\_A[Fe^{3+}{}_2]\_B\ O^{2-}{}_4$, as represented in **Figure (I.14a)** [76].

A defining characteristic of the spinel system, however, is the broad range of cation distributions it can accommodate. Not all spinel compounds adopt the normal configuration as their ground-state arrangement. In the inverse spinel variant, trivalent Y cations preferentially occupy the tetrahedral A-sites, while the octahedral B-sites are shared equally between the divalent X and trivalent Y species, yielding the general formula $[Y]\_A[XY]\_B\ O_4$, as illustrated in **Figure (I.14b)** [77]. At finite temperatures, thermally driven mixing of cationic species — either within the octahedral sublattice or across both sublattices — frequently occurs. This behavior is formally described through an inversion degree parameter x, associated with the generalized cation distribution $[X_{1-x}Y_x]\_A[X_xY_{2-x}]\_B\ O_4$. The inversion parameter ranges from x = 0 for a purely normal spinel to x = 1 for a fully inverse configuration, with a value of x = 2/3 corresponding to a completely random distribution of metal cations across all available sites [78].

At the nanoscale, departures from the bulk normal spinel arrangement become increasingly pronounced. The high surface-to-volume ratio characteristic of nanostructured $ZnFe_2O_4$ promotes surface spin disorder and finite-size effects, which can drive partial inversion of the cation distribution and give rise to superparamagnetic behavior absent in the bulk antiferromagnetic phase. These structural transitions are experimentally confirmed through X-ray diffraction (XRD), which reveals characteristic peaks — most notably at 35.29° — attesting to the high crystallinity of the spinel phase, and through Fourier transform infrared (FTIR)

spectroscopy, which identifies the distinct vibrational signatures of Fe–O and Zn–O bonds within the fingerprint region [76, 78].

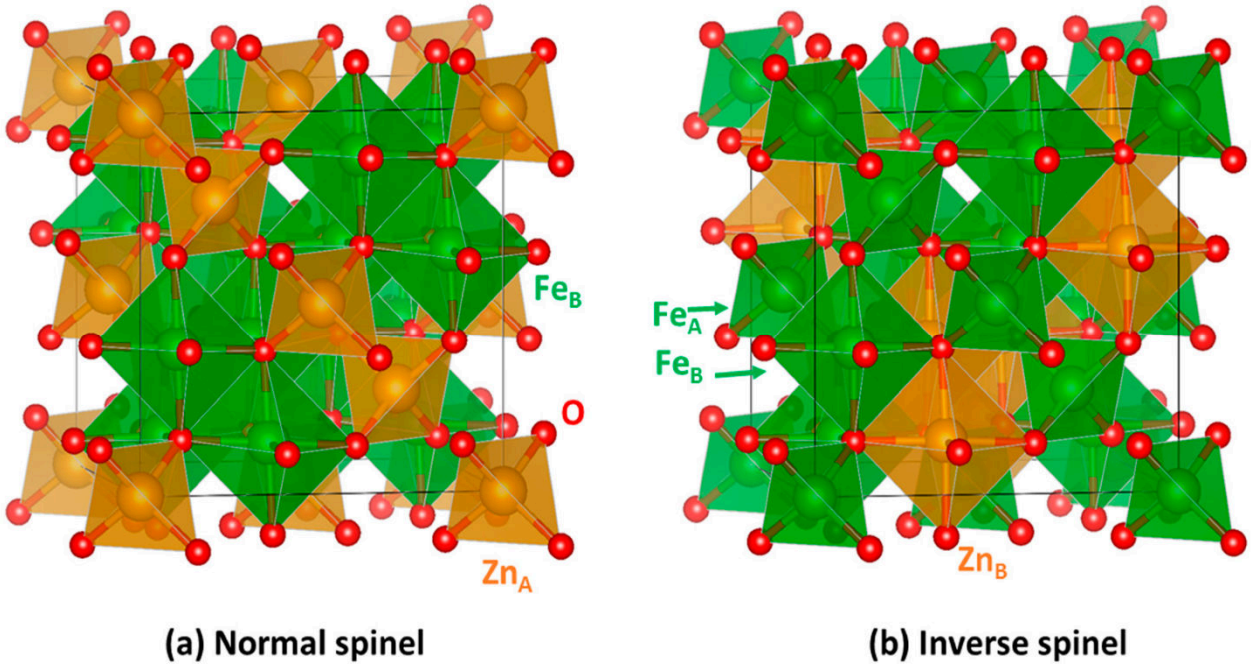

Figure (I.14): *Crystallographic representation of the zinc ferrite spinel structure illustrating:* ***(a)*** *normal cation distribution, with Zn^{2+} occupying tetrahedral (A) sites and Fe^{3+} residing in octahedral (B) sites; and* ***(b)*** *inverse cation distribution, reflecting partial site exchange between cations. The conventional cubic unit cell contains 8 formula units of $ZnFe_2O_4$, delimited by solid black lines. Orange, green, and red spheres represent Zn, Fe, and O atoms, respectively* [79].

I.4. Synthesis Strategies for Metal Oxide Nanoparticles

The fabrication of metal oxide nanoparticles is broadly organized around two overarching philosophical approaches: top-down and bottom-up strategies [80]. Top-down methods begin with bulk material and progressively reduce it to the nanoscale through physical processes such as mechanical milling, grinding, or laser ablation. Bottom-up approaches, by contrast, build nanostructures from the atomic or molecular level upward, relying on techniques such as chemical precipitation, sol-gel processing, and hydrothermal or solvothermal synthesis. The conceptual distinction between these two routes is illustrated in **Figure (I.15)**.

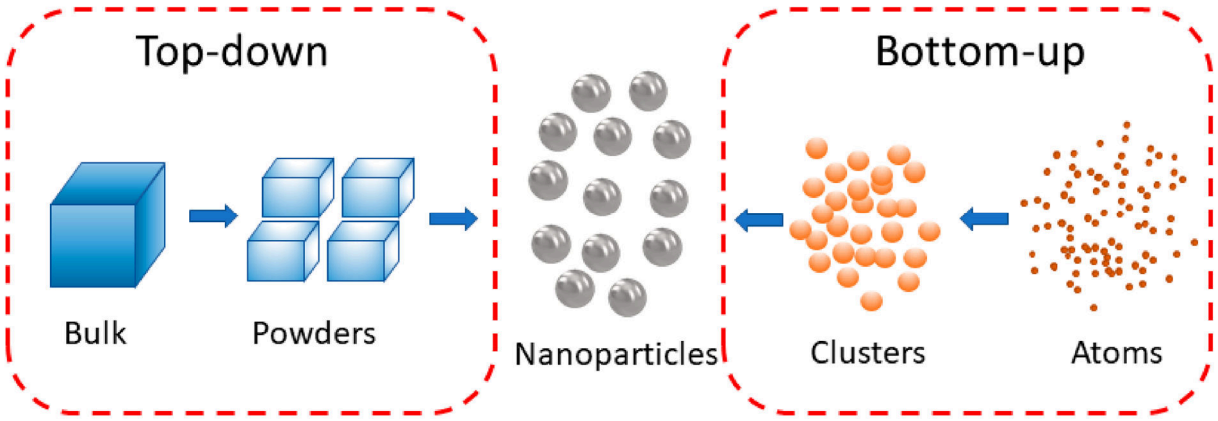

Figure (I.15): *Schematic comparison of top-down and bottom-up approaches to nanoparticle fabrication* [81].

Despite their widespread use, conventional synthesis routes carry notable drawbacks. Many require significant energy input or depend on toxic stabilizing agents that compromise the biocompatibility of the resulting particles and generate environmentally harmful by-products [82, 83]. These limitations have driven growing interest in greener alternatives, particularly biosynthesis-based approaches that harness biological systems — including plant extracts, fungi, and bacteria — as natural reaction platforms [84, 85]. The secondary metabolites present in these biological sources serve a dual function, acting simultaneously as reducing agents to facilitate metal ion conversion and as capping agents to prevent particle agglomeration, while also imparting enhanced antimicrobial activity to the synthesized nanomaterials [86, 87].

This shift toward sustainability extends beyond the choice of reducing agent. Hazardous organic solvents are increasingly being replaced by environmentally benign alternatives such as water, ionic liquids, and supercritical fluids [88]. Synthesis parameters including pH, temperature, and precursor concentration are carefully tuned to achieve precise control over particle size and morphology. The overall trajectory of the field is toward streamlined, low-impact protocols that balance high material performance with ecological responsibility [89, 90], as reflected in the diversity of synthesis pathways summarized in **Figure (I.16)**.

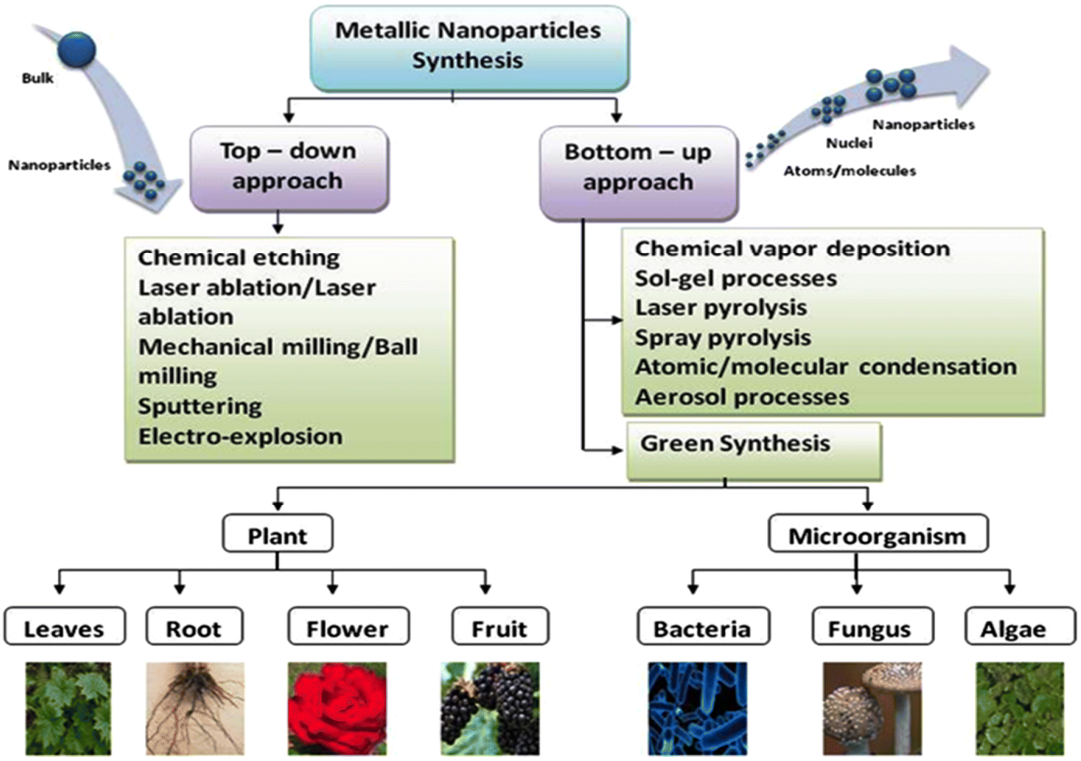

Figure (I.16)*: *Overview of established and emerging synthesis routes for the preparation of metal oxide nanoparticles [91].

I.4.1. Co-Precipitation as a Route to Metal Oxide Nanoparticle Synthesis

Co-precipitation ranks among the most widely adopted techniques for producing metal oxide nanoparticles, owing to its operational simplicity, relatively low cost, and compatibility with large-scale industrial production [92]. The process is fundamentally based on combining metal precursors — typically iron salts such as chlorides or sulfates — with a precipitating agent, commonly sodium hydroxide or ammonia, in an aqueous medium [93, 94]. The resulting alkaline conditions trigger rapid nucleation events, either direct or indirect, leading to the immediate formation of nanoparticles [95, 96], as illustrated in **Figure (II.17)**.

A key advantage of this approach lies in the degree of synthetic control it affords. By systematically varying parameters such as base concentration and salt composition, researchers can influence the final particle morphology, guiding formation from simple spherical geometries to more complex shapes such as octahedra [97]. While co-precipitation reliably yields high-purity particles with narrow size distributions, challenges including agglomeration and oxidative

degradation persist. The incorporation of appropriate stabilizing agents helps maintain monodispersity and preserve the functional integrity of the nanoparticles, particularly in biomedical contexts where performance consistency is critical [98, 99].

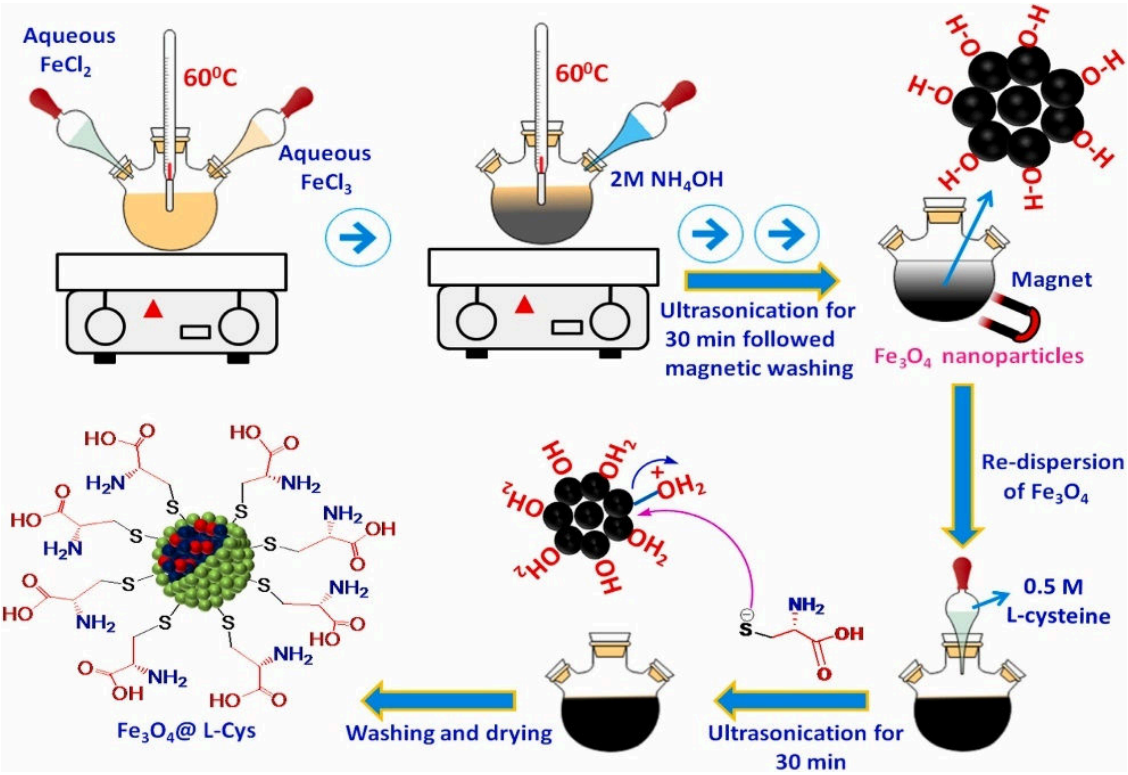

Figure (II.17): *Coprecipitation approach for the synthesis of magnetically recyclable L-cysteine capped Fe_3O_4 nanoadsorbent. (Adapted with permission from Bashir et al., 2021)*[100].

I.4.2. Hydrothermal Synthesis of Nanoparticles

Hydrothermal synthesis represents a well-established bottom-up strategy for the controlled fabrication of nanoparticles, using water as the reaction medium within sealed pressurized vessels. The defining characteristic of this method is its operation at temperatures and pressures approaching or exceeding the critical point of water — 374 °C and 22.1 MPa. Under these conditions, the physicochemical properties of water are substantially altered; a marked reduction in the dielectric constant lowers the solubility of polar salts, inducing supersaturation and promoting rapid crystal nucleation and growth.

This technique is particularly valued for its environmental compatibility, modest energy requirements, and capacity to yield highly crystalline materials with well-defined morphologies, all without requiring high-temperature post-synthesis calcination. Both conventional batch

reactors and advanced continuous hydrothermal flow synthesis (CHFS) systems can be employed to access metastable phases and complex nanostructures with applications spanning bioceramics, heterogeneous catalysis, and high-performance battery electrodes [101–103], as schematically represented in **Figure (I.18)**.

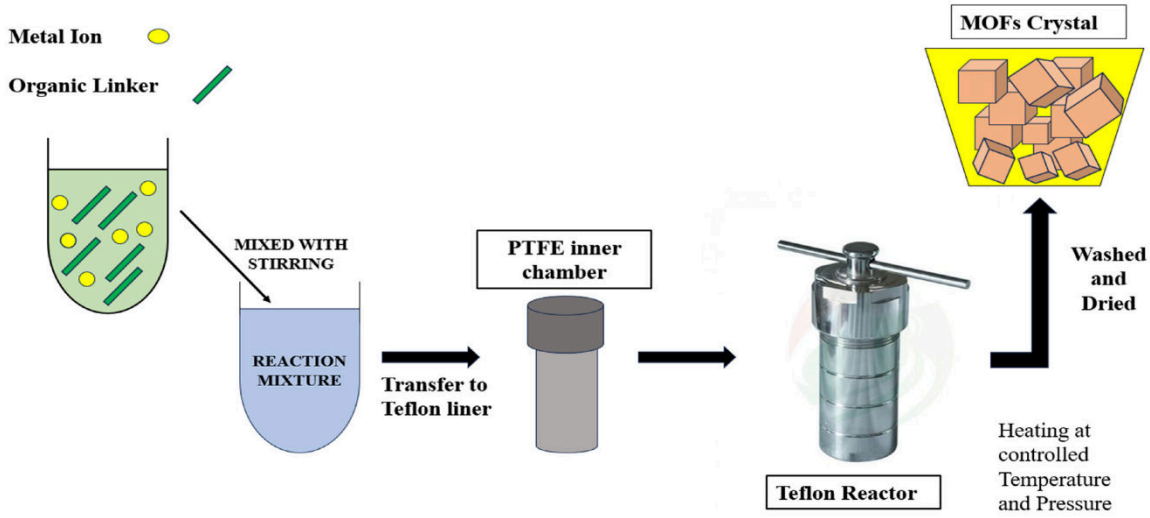

Figure (I.18)*: *Illustration of the hydrothermal and solvothermal synthesis procedure applied to Metal-Organic Framework (MOF) fabrication: sequential steps include preparation of the metal ion and organic linker mixture, transfer to a PTFE-lined chamber, sealing within a Teflon reactor, controlled heating under defined temperature and pressure conditions, followed by washing and drying to recover the final crystalline product. [Adapted from: Lalawmpuia R. et al., Preprints 2023, 2023090192 [104]***, Open Access, CC BY 4.0].***

Taken together, solution-based soft processing routes — including sol-gel, hydrothermal, and solvothermal methods — constitute a complementary and powerful toolkit for engineering advanced inorganic and hybrid nanomaterials, offering low energy consumption, precise morphological control, and molecular-level compositional uniformity [105, 106].

I.4.3. Green Chemistry Approaches to Nanoparticle Synthesis

Green chemistry offers a sustainable and scientifically rigorous alternative to conventional nanoparticle fabrication, circumventing the reliance on toxic reagents and energy-intensive processing conditions [107]. Within this framework, biological entities — including plant-derived extracts from leaves, fruits, and roots, as well as microorganisms such as bacteria

and fungi — are repurposed as natural nanofactories capable of reducing and stabilizing metal ions into well-defined nanostructures [59].

Grounded in twelve foundational principles that emphasize waste minimization and the preferential use of renewable feedstocks, green synthesis routes frequently employ water as a safe and readily available solvent. The biogenic nanoparticles produced through these methods exhibit favorable biocompatibility and low cytotoxicity profiles, rendering them particularly attractive for applications in targeted drug delivery, contrast-enhanced imaging, and environmental remediation [108], as illustrated in **Figure (I.19)**.

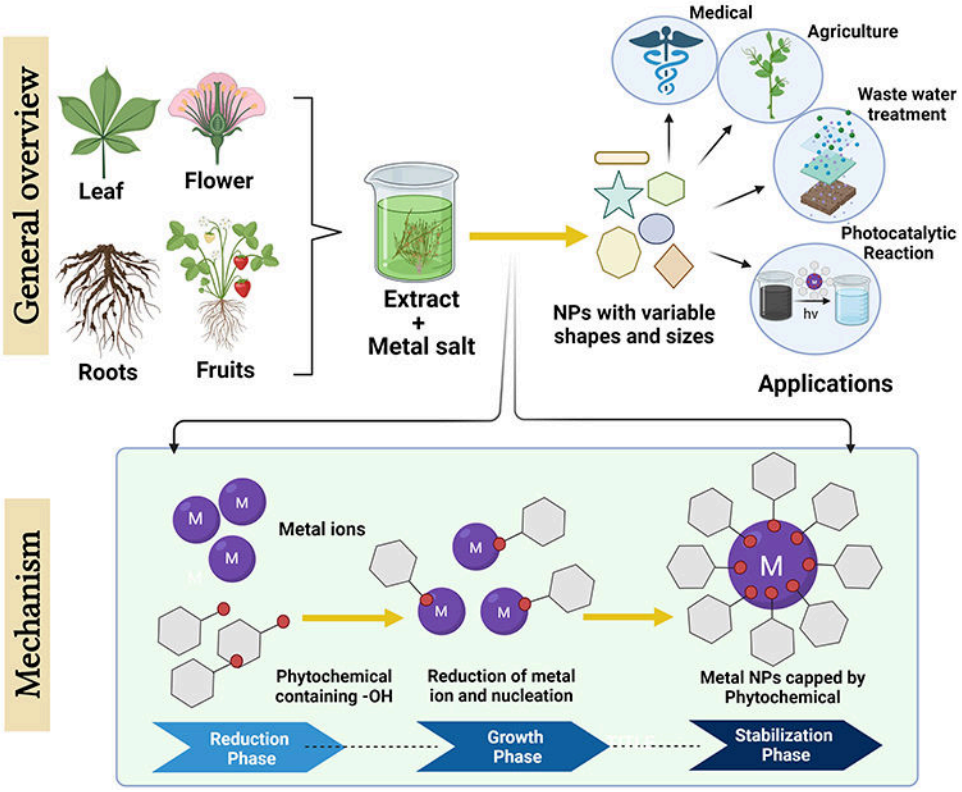

Figure (I.19): *Schematic representation of plant-extract-mediated green synthesis of metallic nanoparticles, highlighting the dual role of phytochemical constituents — including flavonoids, phenols, and terpenoids — as both reducing and capping agents, alongside the three sequential stages of nanoparticle formation: nucleation, growth, and termination* [109].

References

References

1. Guin M, Singh NB (2023) Nanomaterials: Overview and Historical Perspectives. Emerg Nanomater Their Impact Soc 21st Century 135:1–22
2. Gnach A, Lipinski T, Bednarkiewicz A, et al (2015) Upconverting nanoparticles: assessing the toxicity. Chem Soc Rev 44:1561–1584. https://doi.org/10.1039/C4CS00177J
3. Barhoum A, García-Betancourt ML, Jeevanandam J, et al (2022) Review on Natural, Incidental, Bioinspired, and Engineered Nanomaterials: History, Definitions, Classifications, Synthesis, Properties, Market, Toxicities, Risks, and Regulations. Nanomaterials 12:177. https://doi.org/10.3390/nano12020177
4. Barhoum A, García-Betancourt ML, Jeevanandam J, et al (2022) Review on Natural, Incidental, Bioinspired, and Engineered Nanomaterials: History, Definitions, Classifications, Synthesis, Properties, Market, Toxicities, Risks, and Regulations. Nanomater 2022, Vol 12, Page 177 12:177. https://doi.org/10.3390/NANO12020177
5. Barhoum A, Luisa García-Betancourt M (2018) Physicochemical characterization of nanomaterials: Size, morphology, optical, magnetic, and electrical properties. In: Emerging Applications of Nanoparticles and Architectural Nanostructures: Current Prospects and Future Trends. Elsevier Inc., pp 279–304
6. Ali N, Shahzad N, Jabeen M (2024) Nanomaterials: History, Production, Properties, Applications, and Toxicities. Qeios
7. Walter P, Welcomme E, Hallégot P, et al (2006) Early use of PbS nanotechnology for an ancient hair dyeing formula. Nano Lett 6:2215–2219. https://doi.org/10.1021/nl061493u
8. Johnson-Mcdaniel D, Barrett CA, Sharafi A, Salguero TT (2013) Nanoscience of an ancient pigment. J Am Chem Soc 135:1677–1679. https://doi.org/10.1021/ja310587c
9. Reeve AH (2021) Ancient Cyprus in Leeds: Objects, networks and museums from 1870 to 1947
10. Bayda S, Adeel M, Tuccinardi T, et al (2020) The history of nanoscience and nanotechnology: From chemical-physical applications to nanomedicine. Molecules 25:112. https://doi.org/10.3390/molecules25010112

11. Schaming D, Remita H (2015) Nanotechnology: from the ancient time to nowadays. Found Chem 17:187–205. https://doi.org/10.1007/s10698-015-9235-y

12. Kheirandish A, Sepehri Javan N, Mohammadzadeh H (2020) Modified Drude model for small gold nanoparticles surface plasmon resonance based on the role of classical confinement. Sci Rep 10:6517

13. Chandra A, Soni RK, Sharma U, Jain SK (2013) Review Article Nanosuspension : an Overview. 3:162–167

14. Reverchon E, Adami R (2006) Nanomaterials and supercritical fluids. J Supercrit Fluids 37:1–22. https://doi.org/10.1016/j.supflu.2005.08.003

15. Puglisi G, Fresta M, Giammona G, Ventura CA (1995) Influence of the preparation conditions on poly(ethylcyanoacrylate) nanocapsule formation. Int J Pharm 125:283–287. https://doi.org/10.1016/0378-5173(95)00142-6

16. Sotiropoulou S, Sierra-Sastre Y, Mark SS, Batt CA (2008) Biotemplated nanostructured materials. Chem Mater 20:821–834. https://doi.org/10.1021/cm702152a

17. Debnath S, Kumar RS, Babu MN (2024) Green synthesis of metallic nanoparticles and their potential applications. Pharma Times 56:6–11. https://doi.org/10.58532/v3bdcs18ch16

18. Uddandarao P, Balakrishnan RM, Ashok A, et al (2019) Uddandarao P, Balakrishnan RM, Ashok A, Swarup S, Sinha P (2019) Bioinspired ZnS: Gd nanoparticles synthesized from an endophytic fungi Aspergillus flavus for fluorescence-based metal detection. Biomimetics 4(1):11. Biomimetics 4:11. https://doi.org/10.3390/biomimetics4010011

19. Ndolomingo MJ, Bingwa N, Meijboom R (2020) Preparation of silver nanoprism-dye complex for fluorescent detection of dhydrogenperoxide in milk. J Mater Sci 55:6195–6241

20. Mallick P, Satpathy SK, Moharana S (2023) Nanomaterials for Fabrication of Thermomechanical Robust Composite. In: Nanoparticles Reinforced Metal Nanocomposites: Mechanical Performance and Durability. Springer, pp 297–315

21. F. Hasany S, Ahmed I, J R, Rehman A (2013) Systematic Review of the Preparation Techniques of Iron Oxide Magnetic Nanoparticles. Nanosci Nanotechnol 2:148–158. https://doi.org/10.5923/j.nn.20120206.01

22. Li C, Shuford KL, Park QH, et al (2007) High-yield synthesis of single-crystalline gold nano-octahedra. Angew Chemie-International Ed 46:3264–3268

23. Granqvist CG, Buhrman RA (1976) Ultrafine metal particles. J Appl Phys 47:2200–2219. https://doi.org/10.1063/1.322870

24. Kumar H, Venkatesh N, Bhowmik H, Kuila A (2018) Metallic nanoparticle: a review. Biomed J Sci Tech Res 4:3765–3775

25. Singh BK, Lee S, Na K (2020) An overview on metal-related catalysts: metal oxides, nanoporous metals and supported metal nanoparticles on metal organic frameworks and zeolites. Rare Met 39:751–766. https://doi.org/10.1007/s12598-019-01205-6

26. Klabunde KJ, Richards RM (2009) Nanoscale Materials in Chemistry: Second Edition. John Wiley & Sons

27. Schlögl R (2015) Heterogeneous catalysis. Angew Chemie - Int Ed 54:3465–3520. https://doi.org/10.1002/anie.201410738

28. Mirabello V, Calatayud DG, Arrowsmith RL, et al (2015) Metallic nanoparticles as synthetic building blocks for cancer diagnostics: From materials design to molecular imaging applications. J Mater Chem B 3:5657–5672. https://doi.org/10.1039/c5tb00841g

29. Santos C, Gabriel B, Blanchy M, et al (2014) Industrial applications of nanoparticles-a prospective overview 4 PUBLICATIONS 0 CITATIONS SEE PROFILE Selection and peer-review under responsibility of TEMA-Centre for Mechanical Technology and Automation. 5th International conference on Advanced Nano Ma. Mater Today Proc 00:0–000. https://doi.org/10.13140/2.1.5100.6726

30. Baghaban-Eslaminejad M, Oryan A, Kamali A, Moshiri A (2017) The role of nanomedicine, nanotechnology, and nanostructures on oral bone healing, modeling, and remodeling. In: Nanostructures for Oral Medicine. Elsevier, pp 777–832

31. Mody V, Siwale R, Singh A, Mody H (2010) Introduction to metallic nanoparticles. J Pharm Bioallied Sci 2:282. https://doi.org/10.4103/0975-7406.72127

32. Sharif MJ, Hossain MJ (2023) Metallic Nanomaterials as Catalysts. Mater Res Found 141:14–41

33. Chen T, Meng D (2023) A Critical Review of Nanoparticles and Nano Catalyst. J Comput Intell Mater Sci 1:12–22

34. Wang Q, Dai N, Zheng J, Zheng JP (2019) Preparation and catalytic performance of Pt supported on Nafion® functionalized carbon nanotubes. J Electroanal Chem 854:113508. https://doi.org/10.1016/j.jelechem.2019.113508

35. Zhu K, Xu H, Wakeel M, et al (2021) In-situ synthesis of ultrafine Co nanoparticles confined in interconnected nitrogen-doped carbon networks for enhanced reduction of 4-nitrophenol. Appl Surf Sci 563:150320. https://doi.org/10.1016/j.apsusc.2021.150320

36. Katre S, Baghmare P, Giri AS (2024) Photocatalytic nanomaterials and their implications towards biomass conversion for renewable chemical and fuel production. Nanoscale Adv

37. Liew K Bin, Janakiraman AK, Sundarapandian R, et al (2022) A review and revisit of nanoparticles for antimicrobial drug delivery. J Med Life 15:328

38. Mondal SK, Chakraborty S, Manna S, Mandal SM (2024) Antimicrobial nanoparticles: current landscape and future challenges. RSC Pharm 1:388–402

39. Mondal SK, Chakraborty S, Manna S, Mandal SM (2024) Antimicrobial nanoparticles: current landscape and future challenges. RSC Pharm 1:388–402. https://doi.org/10.1039/d4pm00032c

40. Ostwald W (1927) Die Welt der vernachlässigten Dimensionen: eine Einführung in die moderne Kolloidchemie mit besonderer Berücksichtigung ihrer Anwendungen. Theodor Steinkopff

41. Kunckel J (1972) Ars vitraria experimentalis: Oder Vollkommene Glasmacher-Kunst. Georg Olms Verlag

42. Mie G (1908) Beiträge zur Optik trüber Medien, speziell kolloidaler Metallösungen. Ann Phys 330:377–445

43. Stookey SD, Araujo RJ (1968) Selective polarization of light due to absorption by small elongated silver particles in glass. Appl Opt 7:777–779

44. Barton JP, Ma W, Schaub SA, Alexander DR (1991) Electromagnetic field for a beam incident on two adjacent spherical particles. Appl Opt 30:4706–4715

45. Pines D (2018) Elementary excitations in solids. CRC Press

46. Kawabata A, Kubo R (1966) Electronic properties of fine metallic particles. II. Plasma resonance absorption. J Phys Soc Japan 21:1765–1772

47. Peiris S, McMurtrie J, Zhu HY (2016) Metal nanoparticle photocatalysts: Emerging processes for green organic synthesis. Catal Sci Technol 6:320–338. https://doi.org/10.1039/c5cy02048d

48. Wei Z, Spinney R, Ke R, et al (2016) Effect of pH on the sonochemical degradation of organic pollutants. Environ Chem Lett 14:163–182

49. Wen J, Xie J, Chen X, Li X (2017) A review on g-C3N4-based photocatalysts. Appl Surf Sci 391:72–123

50. Plasma-sprayed photocatalytic zinc oxide coatingsNavidpour AH, Kalantari Y, Salehi M, et al (2017) Plasma-sprayed photocatalytic zinc oxide coatings. J Therm Spray Technol 26:717–727

51. Peng L, Xie T, Lu Y, et al (2010) Synthesis, photoelectric properties and photocatalytic activity of the Fe 2 O 3/TiO 2 heterogeneous photocatalysts. Phys Chem Chem Phys 12:8033–8041

52. Guo H, Kemell M, Heikkilä M, Leskelä M (2010) Noble metal-modified TiO2 thin film photocatalyst on porous steel fiber support. Appl Catal B Environ 95:358–364

53. Chen X, Liu L, Yu PY, Mao SS (2011) Increasing solar absorption for photocatalysis with black hydrogenated titanium dioxide nanocrystals. Science (80-) 331:746–750

54. Potbhare AK (2023) Nanomaterials as Photocatalyst. Appl Emerg Nanomater Nanotechnol 148:304–333. https://doi.org/10.21741/9781644902554-11

55. Prasad S, Kumar V, Kirubanandam S, Barhoum A (2018) Engineered nanomaterials: Nanofabrication and surface functionalization. In: Emerging Applications of Nanoparticles and Architectural Nanostructures: Current Prospects and Future Trends. Elsevier Inc., pp 305–340

56. Hammani S, Barhoum A, Nagarajan S, Bechelany M (2019) Toner waste powder (twp) as a filler for polymer blends (ldpe/hips) for enhanced electrical conductivity. Materials (Basel)

12:3062

57. Rasouli R, Barhoum A, Uludag H (2018) A review of nanostructured surfaces and materials for dental implants: Surface coating, patterning and functionalization for improved performance. Biomater. Sci. 6:1312–1338

58. Rahman MA, Hasnain SMM, Pandey S, et al (2024) Review on Nanofluids: Preparation, Properties, Stability, and Thermal Performance Augmentation in Heat Transfer Applications. ACS Omega 9:32328–32349. https://doi.org/10.1021/acsomega.4c03279

59. Ijaz I, Gilani E, Nazir A, Bukhari A (2020) Detail review on chemical, physical and green synthesis, classification, characterizations and applications of nanoparticles. Green Chem Lett Rev 13:59–81. https://doi.org/10.1080/17518253.2020.1802517

60. Anu Mary Ealia S, Saravanakumar MP (2017) A review on the classification, characterisation, synthesis of nanoparticles and their application. In: IOP conference series: materials science and engineering. IOP Publishing, p 32019

61. Kabiraz DC (2021) Chemical modification of carbon electrode for sensing application. Chem Modif solid surfaces by use Addit 110–138

62. Council NR, Earth D on, Studies L, et al (2009) Science and decisions: advancing risk assessment. National Academies Press

63. Afolalu SA, Soetan SB, Ongbali SO, et al (2019) Morphological characterization and physio-chemical properties of nanoparticle-review. In: IOP Conference Series: Materials Science and Engineering. IOP Publishing, p 12065

64. Joudeh N, Linke D (2022) Nanoparticle classification, physicochemical properties, characterization, and applications: a comprehensive review for biologists. J Nanobiotechnology 20:262. https://doi.org/10.1186/s12951-022-01477-8

65. Khan W, Sharma R, Saini P (2016) Carbon nanotube-based polymer composites: synthesis, properties and applications. Carbon Nanotub Prog their Polym Compos 1:1–45

66. Cho G, Park Y, Hong Y-K, Ha D-H (2019) Ion exchange: an advanced synthetic method for complex nanoparticles. Nano Converg 6:17

67. Zhang L, Webster TJ (2009) Nanotechnology and nanomaterials: promises for improved

tissue regeneration. Nano Today 4:66–80

68. Poh TY, Ali NABM, Mac Aogáin M, et al (2018) Inhaled nanomaterials and the respiratory microbiome: clinical, immunological and toxicological perspectives. Part Fibre Toxicol 15:46. https://doi.org/10.1186/s12989-018-0282-0

69. Khatami M, Alijani HQ, Nejad MS, Varma RS (2018) Core@ shell nanoparticles: greener synthesis using natural plant products. Appl Sci 8:411

70. Iqbal A, Ali S (2024) Nanomaterials: Fabrication Approaches and Applications. 469–498

71. Mekuye B, Abera B (2023) Nanomaterials: An overview of synthesis, classification, characterization, and applications. Nano Sel 4:486–501. https://doi.org/10.1002/nano.202300038

72. Rampino LD, Nord FF (1941) Preparation of palladium and platinum synthetic high polymer catalysts and the relationship between particle size and rate of hydrogenation. J Am Chem Soc 63:2745–2749

73. Tsai C, Shiau A, Chen S, et al (2007) Amelioration of collagen-induced arthritis in rats by nanogold. Arthritis Rheum Off J Am Coll Rheumatol 56:544–554

74. Ramezani N, Ehsanfar Z, Shamsa F, et al (2008) Screening of medicinal plant methanol extracts for the synthesis of gold nanoparticles by their reducing potential. Zeitschrift für Naturforsch B 63:903–908

75. Frens G (1973) Controlled nucleation for the regulation of the particle size in monodisperse gold suspensions. Nat Phys Sci 241:20–22

76. Kamazawa K, Tsunoda Y, Kadowaki H, Kohn K (2003) Magnetic neutron scattering measurements on a single crystal of frustrated ZnFe2O4. Phys Rev B - Condens Matter Mater Phys 68:024412. https://doi.org/10.1103/PhysRevB.68.024412

77. Bohra M, Agarwal N, Singh V (2019) A Short Review on Verwey Transition in Nanostructured Fe3O4 Materials. J Nanomater 2019:1–18. https://doi.org/10.1155/2019/8457383

78. Ferrari S, Kumar RS, Grinblat F, et al (2016) In-situ high-pressure x-ray diffraction study of zinc ferrite nanoparticles. Solid State Sci 56:68–72.

https://doi.org/10.1016/j.solidstatesciences.2016.04.006

79. Bohra M, Alman V, Arras R (2021) Nanostructured znfe2o4: An exotic energy material. Nanomaterials 11:1286. https://doi.org/10.3390/nano11051286

80. Nadaf SJ, Jadhav NR, Naikwadi HS, et al (2022) Green synthesis of gold and silver nanoparticles: Updates on research, patents, and future prospects. OpenNano 8:100076

81. Lu H, Tang SY, Yun G, et al (2020) Modular and Integrated Systems for Nanoparticle and Microparticle Synthesis—A Review. Biosensors 10:165. https://doi.org/10.3390/BIOS10110165

82. Nair GM, Sajini T, Mathew B (2022) Advanced green approaches for metal and metal oxide nanoparticles synthesis and their environmental applications. Talanta Open 5:100080. https://doi.org/10.1016/j.talo.2021.100080

83. Nguyen NTT, Nguyen TTT, Nguyen DTC, Van Tran T (2023) Green synthesis of ZnFe2O4 nanoparticles using plant extracts and their applications: A review. Sci Total Environ 872:162212

84. Nasaruddin RR, Chen T, Yao Q, et al (2021) Toward greener synthesis of gold nanomaterials: From biological to biomimetic synthesis. Coord Chem Rev 426:213540

85. Suppiah DD, Julkapli NM, Sagadevan S, Johan MR (2023) Eco-friendly green synthesis approach and evaluation of environmental and biological applications of Iron oxide nanoparticles. Inorg Chem Commun 152:110700

86. Salem SS, Fouda A (2021) Green Synthesis of Metallic Nanoparticles and Their Prospective Biotechnological Applications: an Overview. Biol Trace Elem Res 199:344–370. https://doi.org/10.1007/s12011-020-02138-3

87. Kuppusamy P, Yusoff MM, Maniam GP, Govindan N (2016) Biosynthesis of metallic nanoparticles using plant derivatives and their new avenues in pharmacological applications – An updated report. Saudi Pharm J 24:473–484. https://doi.org/10.1016/j.jsps.2014.11.013

88. Kus NS (2012) Organic reactions in subcritical and supercritical water. Tetrahedron 68:949–958

89. Chaudhary J, Tailor G, Yadav M, Mehta C (2023) Green route synthesis of metallic

nanoparticles using various herbal extracts: A review. Biocatal Agric Biotechnol 50:102692

90. Paiva-Santos AC, Herdade AM, Guerra C, et al (2021) Plant-mediated green synthesis of metal-based nanoparticles for dermopharmaceutical and cosmetic applications. Int J Pharm 597:120311

91. Singh J, Dutta T, Kim K-HH, et al (2018) 'Green' synthesis of metals and their oxide nanoparticles: applications for environmental remediation. J Nanobiotechnology 16:84. https://doi.org/10.1186/s12951-018-0408-4

92. Al-Madhagi H, Yazbik V, Abdelwahed W, Alchab L (2023) Magnetite Nanoparticle Co-Precipitation Synthesis, Characterization, and Applications: Mini Review. Bionanoscience 13:853–859

93. de la Encarnación C, de Aberasturi DJ, Liz-Marzán LM (2022) Multifunctional plasmonic-magnetic nanoparticles for bioimaging and hyperthermia. Adv Drug Deliv Rev 189:114484

94. Schwaminger SP, Fraga-García P, Blank-Shim SA, et al (2019) Magnetic one-step purification of his-tagged protein by bare iron oxide nanoparticles. ACS omega 4:3790–3799

95. Kandpal ND, Sah N, Loshali R, et al (2014) Co-precipitation method of synthesis and characterization of iron oxide nanoparticles

96. Hui BH, Salimi MN (2020) Production of iron oxide nanoparticles by co-precipitation method with optimization studies of processing temperature, pH and stirring rate. In: IOP conference series: materials science and engineering. IOP Publishing, p 12036

97. Montes-Hernandez G, Findling N, Renard F (2021) Direct and indirect nucleation of magnetite nanoparticles from solution revealed by time-resolved Raman spectroscopy. Cryst Growth Des 21:3500–3510

98. Ferreira LP, Reis CP, Robalo TT, et al (2022) Assisted synthesis of coated iron oxide nanoparticles for magnetic hyperthermia. Nanomaterials 12:1870

99. Tay ZW, Chandrasekharan P, Chiu-Lam A, et al (2018) Magnetic particle imaging-guided heating in vivo using gradient fields for arbitrary localization of magnetic hyperthermia therapy. ACS Nano 12:3699–3713

100. Bashir A, Pandith AH, Malik LA, et al (2021) Magnetically recyclable L-cysteine capped Fe3O4 nanoadsorbent: A promising pH guided removal of Pb(II), Zn(II) and HCrO4-contaminants. J Environ Chem Eng 9:105880. https://doi.org/10.1016/j.jece.2021.105880

101. Aliofkhazraei M (2015) Handbook of nanoparticles

102. Pérez-Tijerina E, Pinilla MG, Mejía-Rosales S, et al (2008) Highly size-controlled synthesis of Au/Pd nanoparticles by inert-gas condensation. Faraday Discuss 138:353–362

103. Helgeson HC, Kirkham DH, Flowers GC (1981) Theoretical prediction of the thermodynamic behavior of aqueous electrolytes at high pressures and temperatures: IV. Calculation of activity coefficients, osmotic coefficients, and apparent molal and standard and relative partial molal properties to 600oC. Am J Sci 281:1249–1516. https://doi.org/10.2475/ajs.281.10.1249

104. Lalawmpuia R, Lalhruaitluangi M, Lalhmunsiama, Tiwari D (2024) Metal organic framework (MOF): Synthesis and fabrication for the application of electrochemical sensing. Environ Eng Res 29:. https://doi.org/10.4491/eer.2023.636

105. Yu SH (2001) Hydrothermal/solvothermal processing of advanced ceramic materials. J Ceram Soc Japan 109:. https://doi.org/10.2109/jcersj.109.1269_s65

106. Singh H, Desimone MF, Pandya S, et al (2023) Revisiting the Green Synthesis of Nanoparticles: Uncovering Influences of Plant Extracts as Reducing Agents for Enhanced Synthesis Efficiency and Its Biomedical Applications. Int J Nanomedicine 18:4727–4750. https://doi.org/10.2147/IJN.S419369

107. Soltys L, Olkhovyy O, Tatarchuk T, Naushad M (2021) Green synthesis of metal and metal oxide nanoparticles: Principles of green chemistry and raw materials. Magnetochemistry 7:145. https://doi.org/10.3390/magnetochemistry7110145

108. Remya VR, Abitha VK, Rajput PS, et al (2019) Silver Nanoparticles Green Synthesis: A Mini Review. Chem Int 3:165–171

109. Singh H, Desimone MF, Pandya S, et al (2023) Revisiting the Green Synthesis of Nanoparticles: Uncovering Influences of Plant Extracts as Reducing Agents for Enhanced Synthesis Efficiency and Its Biomedical Applications. Int J Nanomedicine Volume 18:4727–4750. https://doi.org/10.2147/IJN.S419369

CHAPTER II

Synthesis and Characterization

II.1. Co-precipitation Method for Spinel Ferrite Nanoparticles

The co-precipitation method is a widely adopted technique for synthesizing spinel ferrite nanoparticles due to its simplicity, low cost, and scalability. It involves dissolving stoichiometric amounts of Fe^{3+} and divalent metal salts (M^{2+}) in aqueous solution, followed by the addition of NaOH or NH_4OH as a precipitating agent. The resulting hydroxide precipitate is washed, dried, and calcined to obtain the spinel phase MFe_2O_4. Particle size and magnetic properties can be controlled by adjusting pH, temperature, and precursor concentration [1]. Spinel ferrites crystallize in the cubic $Fd\bar{3}m$ structure, where cation distribution between tetrahedral and octahedral sites governs their magnetic behavior [2]. Several studies confirmed that co-precipitated ferrite nanoparticles exhibit superparamagnetic properties suitable for biomedical applications [3]. In this work, spinel ferrite nanoparticles were successfully prepared using this approach, yielding phase-pure powders with well-defined structural and magnetic characteristics.

II.2. Materials and Methods

To synthesize zinc ferrite nanoparticles, zinc acetate dihydrate $Zn(CH_3COO)_2 \cdot 2H_2O$ (MW = 219.5 g/mol) and iron(III) chloride hexahydrate $FeCl_3 \cdot 6H_2O$ (MW = 270.3 g/mol) were used as precursors, while sodium hydroxide (NaOH) served as both the precipitating agent and pH regulator. All solutions were prepared using deionized water (DI water).

II.2.1. Synthesis of Zinc Ferrite Nanoparticles by Co-precipitation Method

To produce approximately 10 g of $ZnFe_2O_4$, the required amounts of each precursor were carefully calculated based on the stoichiometric ratios of the spinel ferrite formula. Accordingly, 9.11 g of $Zn(CH_3COO)_2 \cdot 2H_2O$ (0.0415 mol) and 22.43 g of $FeCl_3 \cdot 6H_2O$ (0.083 mol) were weighed and dissolved separately, each in 100 mL of deionized water. As expected, the iron chloride solution turned dark orange upon dissolution, which is a typical visual indicator of Fe^{3+} ions in aqueous medium. The two solutions were then poured together into a 500 mL beaker and stirred magnetically at room temperature until a fully homogeneous mixture was obtained.

Once the mixed solution was ready, a 2 M NaOH solution was introduced dropwise under vigorous and uninterrupted stirring. Particular care was taken during this step to ensure that the base was added as slowly as possible, which is critical for achieving uniform nucleation and avoiding the formation of secondary phases. The pH of the solution was monitored continuously using a calibrated pH meter, and the addition of NaOH was maintained until the pH stabilized at

11. As soon as the alkaline environment was established, a reddish-brown precipitate appeared, signaling the successful co-precipitation of the metal hydroxides (**Figure II.1**). This color transition is in good agreement with what has been reported in the literature for similar ferrite systems prepared under comparable conditions [4].

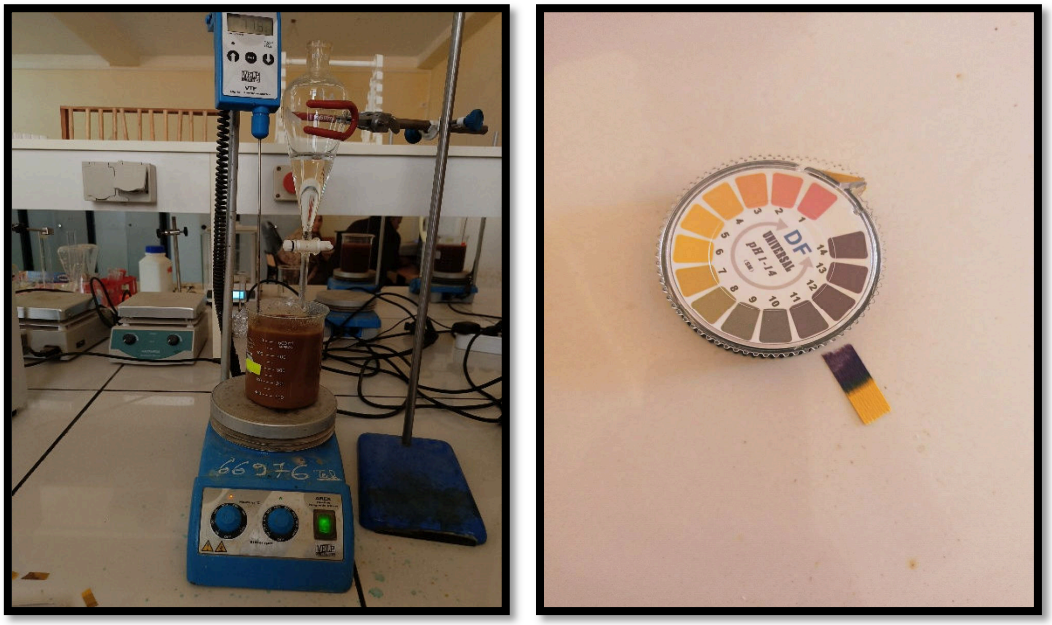

Figure (II.1): *Photograph of the reddish-brown precipitate formed during co-precipitation of $ZnFe_2O_4$ nanoparticles at pH = 11.*

The suspension was subsequently transferred to a hot plate and heated to 80 °C, where it was kept under continuous stirring for 2 hours. This aging step plays an important role in driving the reaction toward completion and in promoting the growth of well-defined nanocrystallites. After the mixture cooled down naturally to room temperature, the precipitate was recovered by centrifugation at speeds ranging from 6000 to 10000 rpm. The collected solid was washed repeatedly with deionized water, typically five to seven times, until the pH of the supernatant approached neutral values between 7 and 8, ensuring the complete removal of residual chloride and acetate ions. The washed precipitate was then placed in an oven and dried at 100 °C for 24 hours.

After drying, the powder was ground into a fine homogeneous mass using a mortar and pestle to break up any aggregates before the thermal treatment. The ground powder was placed in an alumina crucible and introduced into a muffle furnace, where it was calcined at 800 °C for 4

hours. This calcination step is indispensable, as it promotes the complete transformation of the precursor hydroxides into the crystalline spinel $ZnFe_2O_4$ phase [5]. The entire synthesis pathway, from precursor dissolution to the final calcined product, is summarized in the graphical illustration shown in **Figure (II.2)**. Once the furnace cycle was complete, the product was allowed to cool to room temperature before being collected and stored in a sealed container pending further structural and magnetic characterization.

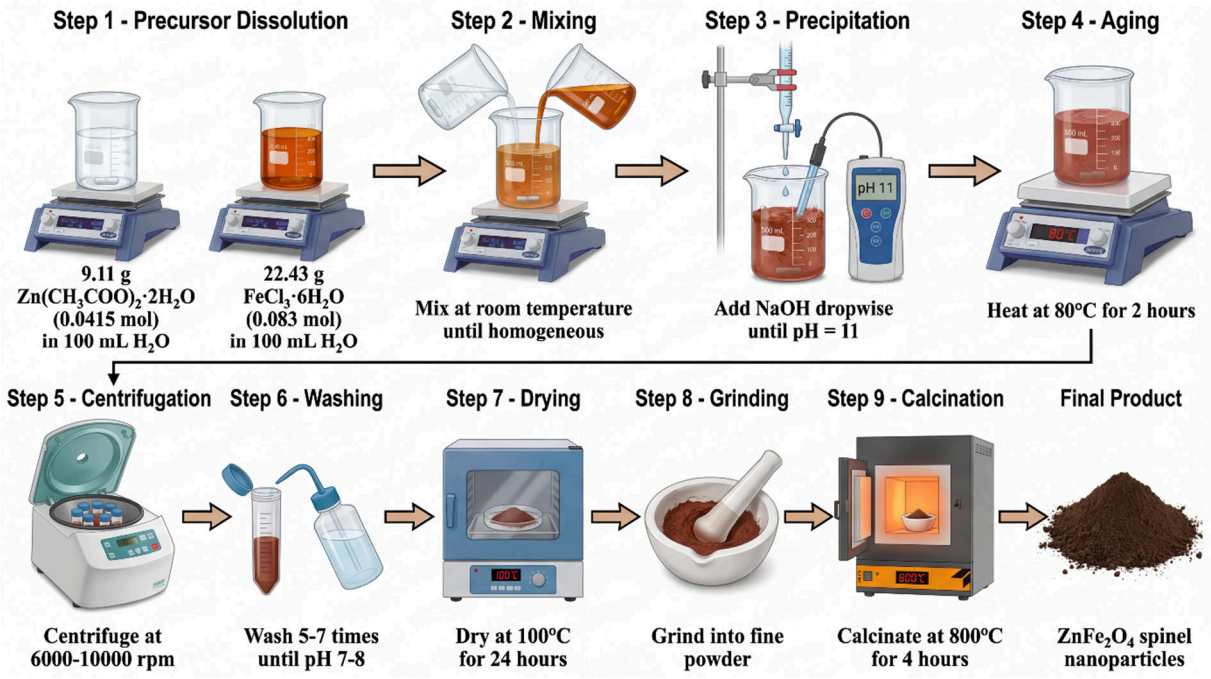

Figure (II.2): *Schematic representation of the synthesis procedure of $ZnFe_2O_4$ spinel nanoparticles by the co-precipitation method.*

II.2.2. Characterization Techniques

Understanding the properties of synthesized nanomaterials requires a thorough and multi-faceted characterization approach, since no single technique is sufficient to capture all the relevant structural, optical, and chemical features of a given material. The physicochemical properties of nanoparticles, including their crystalline structure, chemical bonding, morphology, surface composition, and optical behavior, are intimately linked to their performance in practical applications. For this reason, a combination of complementary techniques is always preferred over relying on a single method [6].

In the present work, the synthesized $ZnFe_2O_4$ spinel nanoparticles were characterized using three well-established analytical techniques: X-ray diffraction (XRD), Fourier-transform infrared spectroscopy (FTIR), and UV-Vis spectroscopy. XRD was employed to confirm the formation of the spinel phase and to determine the crystallite size, while FTIR was used to identify the characteristic metal-oxygen vibrational bands associated with the spinel structure. UV-Vis spectroscopy was performed to investigate the optical properties and estimate the optical bandgap of the prepared nanoparticles. Each of these techniques will be briefly described in the following sections.

II.2.2.1 Spectroscopy

Spectroscopy is a broad analytical discipline concerned with examining how matter interacts with electromagnetic radiation across different wavelength ranges. When radiation encounters a material, various physical phenomena may occur depending on the energy of the incident photons and the nature of the material itself, including absorption, transmission, reflection, or scattering. Each of these interactions produces a characteristic spectral response that carries detailed information about the composition, electronic structure, and bonding environment of the material under investigation. Since different regions of the electromagnetic spectrum probe different aspects of matter, combining multiple spectroscopic approaches provides a far more complete picture than any single measurement alone [7]. In this work, two spectroscopic techniques were employed to characterize the synthesized $ZnFe_2O_4$ nanoparticles, namely UV-Vis absorption spectroscopy and Fourier-transform infrared spectroscopy, both of which are described in the sections that follow.

II.2.2.1.1. UV-Visible Absorption Spectroscopy

UV-Vis absorption spectroscopy is one of the most widely used optical characterization tools in materials science, particularly for nanomaterials, owing to its simplicity, non-destructive nature, and the wealth of information it can provide. The technique is based on measuring the attenuation of a beam of light as it passes through a sample across the ultraviolet and visible regions of the electromagnetic spectrum, typically spanning wavelengths from 200 to 800 nm. The instrument used to perform this measurement is the UV-Vis spectrophotometer, which compares the intensity of the incident light beam (I_0) with that of the transmitted beam (I) after interaction with the sample. The ratio of these two quantities defines the transmittance $T = I/I_0$, which is

commonly expressed as a percentage (%T). The absorbance (A) is then derived from the transmittance as expressed in **(Eq (II.1))**:

$$A = \log_{10}\left(\frac{\%T}{100}\right) \qquad \textbf{(II. 1)}$$

The quantitative relationship between absorbance and sample concentration is governed by the Beer–Lambert law [8], given as **(Eq (II.2))**:

$$A = \log_{10}\left(\frac{I_0}{I}\right) = \varepsilon c l \qquad \textbf{(II. 2)}$$

where **A** is the measured absorbance, $\mathbf{I_0}$ is the initial light intensity before interaction with the sample at a given wavelength, **I** is the transmitted intensity, **l** is the optical path length through the sample (cm), **c** is the concentration of the absorbing species ($mol \cdot L^{-1}$), and **ε** is a constant referred to as the molar absorptivity or extinction coefficient ($L \cdot mol^{-1} \cdot cm^{-1}$). This law holds reliably under conditions of monochromatic radiation and sufficiently dilute solutions where scattering effects remain negligible.

Beyond concentration measurements, UV-Vis spectroscopy is particularly valuable in nanomaterials research for estimating the optical bandgap energy using the Tauc plot method, identifying characteristic absorption bands linked to electronic transitions, and probing the presence of specific chromophoric groups within the material [9].

- **The Principle of Operation of the Spectrophotometer**

The working principle of the UV-Vis spectrophotometer is rooted in the interaction between electromagnetic radiation and the electronic structure of matter. When a photon carrying sufficient energy strikes an atom or molecule, it is absorbed and its energy is transferred to an electron, causing it to jump from a lower energy level to a higher one. This transition occurs specifically from the highest occupied molecular orbital (HOMO) to the lowest unoccupied molecular orbital (LUMO). The wavelength at which this absorption takes place is characteristic of the type of chemical bond present in the material. As illustrated in **(Figure II.3a)**, electronic transitions vary in energy depending on the bond involved: σ→σ* transitions are the most energetic and typically occur in the deep ultraviolet region, whereas π→π* and n→π* transitions require less energy and

fall within the accessible UV-Vis range, making them particularly relevant for characterizing organic chromophores and semiconductor nanomaterials alike [9].

From an instrumental standpoint, the spectrophotometer generates a monochromatic beam of light that is split into two separate paths. The first beam passes through the sample cell containing the material under investigation, while the second travels through a reference cell containing only the solvent or blank. After passing through their respective cells, both beams reach dedicated photodetectors, which measure their intensities and compare them electronically. The resulting output is the absorbance spectrum of the sample, corrected for any contribution from the solvent or background. This dual-beam configuration, shown in **(Figure II.3b)**, ensures high measurement accuracy and minimizes instrumental drift during the analysis [8].

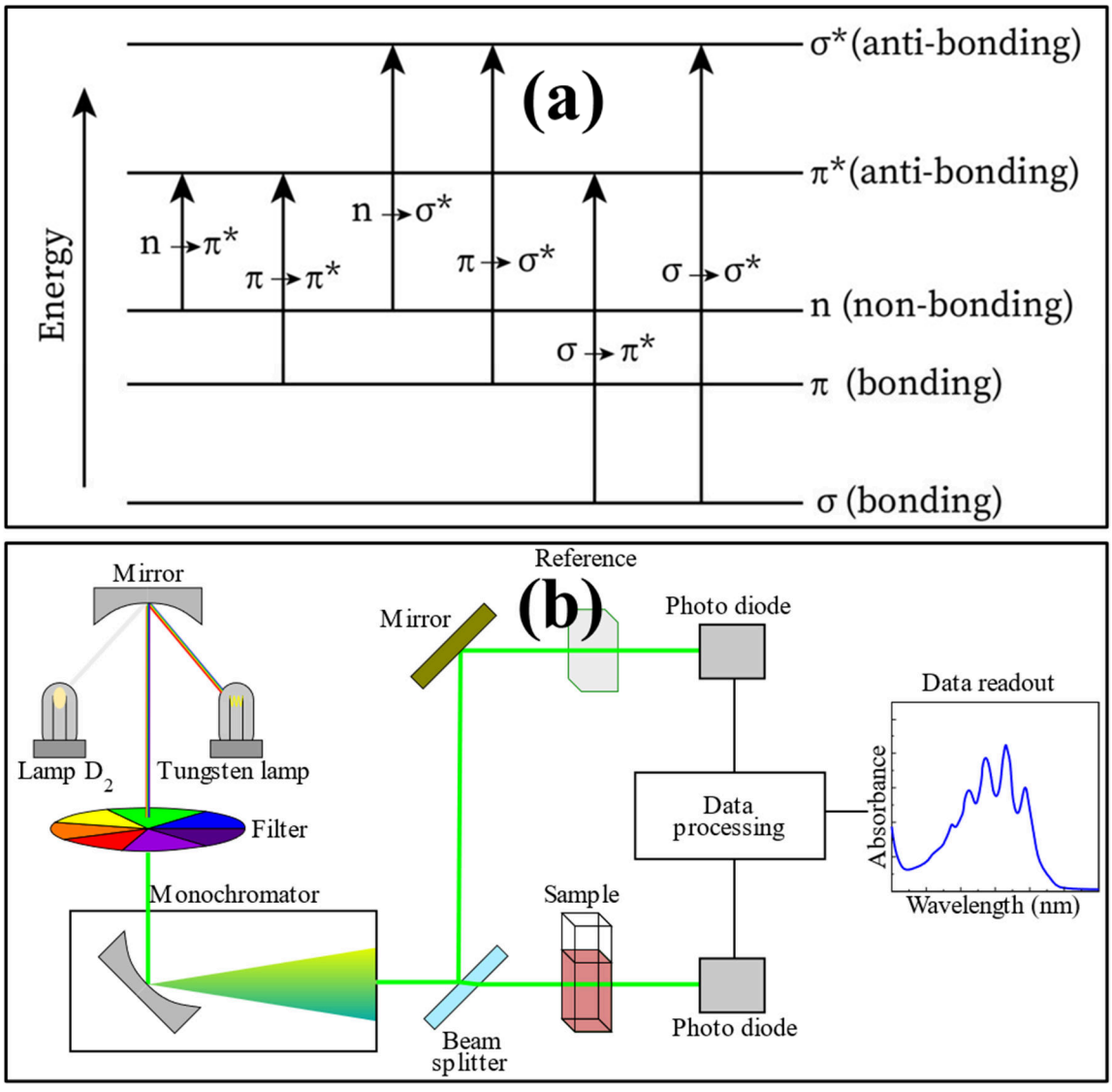

Figure (II.3): *(a) Electronic transitions between molecular orbitals during UV-Vis light absorption; (b) Schematic diagram of a typical dual-beam UV-Vis spectrophotometer setup.*

II.2.2.1.2 Fourier Transform Infrared (FTIR) Spectroscopy

Fourier Transform Infrared spectroscopy is one of the most informative and routinely employed characterization techniques in the field of nanomaterials science. What distinguishes FTIR from other spectroscopic methods is its ability to simultaneously probe the entire mid-infrared spectral range, typically between 400 and 4000 cm^{-1}, in a single measurement, rather than scanning individual frequencies one at a time as in conventional dispersive instruments. This multiplex advantage, combined with its high sensitivity and reproducibility, makes FTIR an indispensable tool for identifying chemical bonds, confirming phase formation, detecting surface functionalization, and monitoring structural changes in nanoparticle systems [10].

The operating principle of FTIR is fundamentally rooted in the interaction between infrared photons and the vibrational degrees of freedom of molecular bonds. When infrared radiation of a frequency matching the natural vibrational frequency of a particular bond is incident on a sample, the bond absorbs that energy and undergoes stretching or bending motions. For this absorption to be infrared-active, the vibration must be accompanied by a net change in the electric dipole moment of the molecule. The absorbed frequencies are thus characteristic of specific bond types and functional groups, and their positions in the spectrum serve as a reliable molecular fingerprint for compound identification [11].

From an instrumental perspective, the heart of an FTIR spectrometer is the Michelson interferometer, which consists of a fixed mirror, a moving mirror, and a beam splitter. The infrared beam from the source is divided into two paths by the beam splitter; one beam reflects off the fixed mirror while the other reflects off the moving mirror, which oscillates at a controlled velocity. When the two beams recombine, they produce an interference pattern known as an interferogram, whose intensity varies as a function of the mirror displacement. This interferogram encodes the full spectral information of the source and, after passing through the sample, is recorded by a detector and mathematically converted into the conventional absorbance spectrum using the Fourier transform algorithm. The complete instrumental setup is illustrated in **(Figure II.4)** [10].

In the context of spinel ferrite nanoparticles, FTIR spectroscopy plays a particularly important role in confirming the successful formation of the desired phase. The spinel structure is characterized by two distinct sublattice sites: tetrahedral (A-sites) and octahedral (B-sites), both of which give

rise to characteristic metal–oxygen stretching vibrations in the infrared spectrum. For $ZnFe_2O_4$ nanoparticles specifically, two prominent absorption bands are typically observed in the low-wavenumber region: a higher-frequency band around 550–600 cm^{-1} attributed to the stretching vibration of metal–oxygen bonds at tetrahedral sites, and a lower-frequency band near 400–450 cm^{-1} associated with octahedral site vibrations. The presence and positions of these bands provide direct evidence for the formation of the spinel ferrite phase and can also reflect changes in cation distribution resulting from variations in synthesis conditions [12]. Beyond phase identification, FTIR is also sensitive to surface-adsorbed species such as hydroxyl groups, residual organic precursors, and moisture, all of which appear as additional absorption features and must be accounted for when interpreting the spectra of co-precipitated nanoparticles.

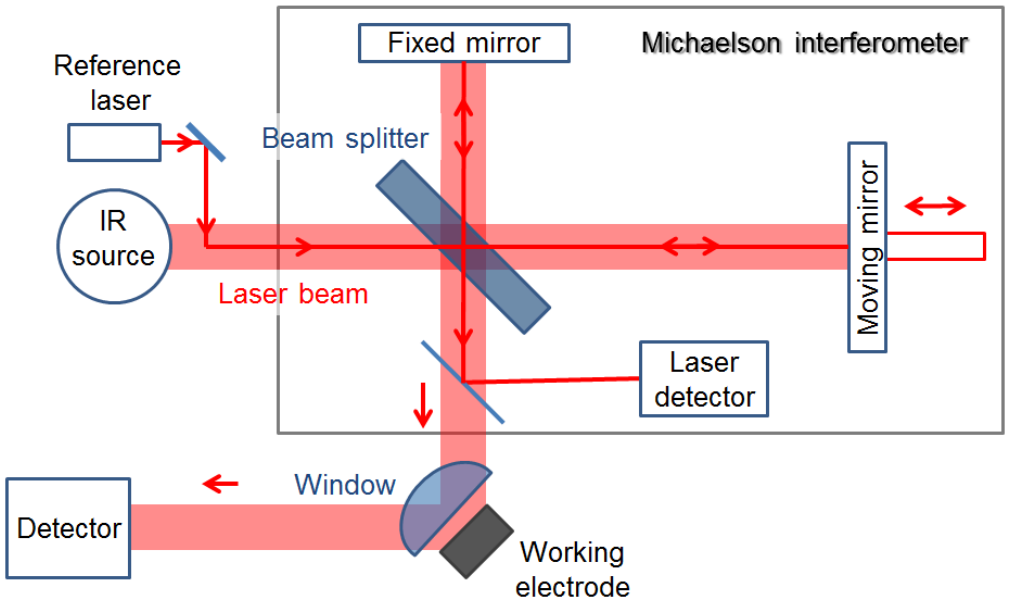

Figure (II.4): *Schematic diagram of a Fourier-transform infrared (FTIR) spectrometer. Adapted from reference* [13].

II.2.2.2. X-ray Diffraction (XRD)

X-ray diffraction is one of the most fundamental and widely applied techniques for the structural characterization of crystalline materials, and its origins trace back to the accidental discovery of X-rays by Wilhelm Conrad Röntgen in 1895. Working with a Crookes tube, Röntgen noticed that a fluorescent screen in his laboratory began to glow even when shielded from direct light, leading him to identify a new form of penetrating radiation, which he named X-Strahlen. His early experiments demonstrated that this radiation could pass through soft tissue and cast shadows

of denser structures such as bones onto photographic plates, an observation that immediately hinted at the extraordinary potential of X-rays as a probe of matter [14]. In the years that followed, the scientific community gradually unraveled the wave nature of X-rays, and in 1912, Max von Laue demonstrated that crystals could diffract X-rays, a finding that laid the groundwork for X-ray diffraction as a structural analysis tool.

The physical principle underlying XRD is relatively straightforward. X-rays are high-energy electromagnetic radiation with wavelengths in the range of 0.01 to 10 nm, comparable in magnitude to the interatomic spacings in crystalline solids. When a monochromatic X-ray beam strikes a crystalline sample, the radiation interacts primarily with the electron clouds surrounding the atoms arranged in the periodic crystal lattice. Each set of parallel atomic planes acts as a partial reflector, and the waves scattered from successive planes interfere constructively only when the path difference between them equals an integer multiple of the wavelength. This condition is precisely described by Bragg's law **(Eq (II.3))** [15]:

$$n\lambda = 2d \sin\theta \qquad \textbf{(II. 3)}$$

where **n** is a positive integer representing the diffraction order, **λ** is the wavelength of the incident X-ray beam, **d** is the interplanar spacing between successive crystallographic planes, and **θ** is the angle of incidence measured from the plane surface. When this condition is satisfied, a sharp diffraction peak appears in the recorded pattern at the corresponding angle 2θ, as illustrated in **(Figure II.5)**. The angular positions and relative intensities of these peaks constitute a unique fingerprint of the crystal structure, and they are routinely compared against reference patterns from the Joint Committee on Powder Diffraction Standards (JCPDS) database to identify the crystalline phase of the material under investigation.

In addition to phase identification, XRD provides quantitative information about the average crystallite size of nanoparticles through analysis of the peak broadening. As the crystallite dimensions decrease into the nanometer range, the diffraction peaks broaden measurably due to the reduced number of diffracting planes contributing to each reflection. This broadening is described quantitatively by the Scherrer equation **(Eq (II.4))** [16]:

$$D = \frac{K\lambda}{\beta \cos\theta} \qquad \textbf{(II. 4)}$$

where **D** is the mean crystallite size, **K** is the Scherrer shape factor, typically taken as 0.89 for spherical crystallites, **λ** is the X-ray wavelength, **β** is the full width at half maximum (FWHM) of the diffraction peak expressed in radians, and **θ** is the Bragg angle. In the present work, XRD was employed to confirm the formation of the pure spinel $ZnFe_2O_4$ phase, to determine the lattice parameter, and to estimate the mean crystallite size of the synthesized nanoparticles from the broadening of the most intense diffraction peak.

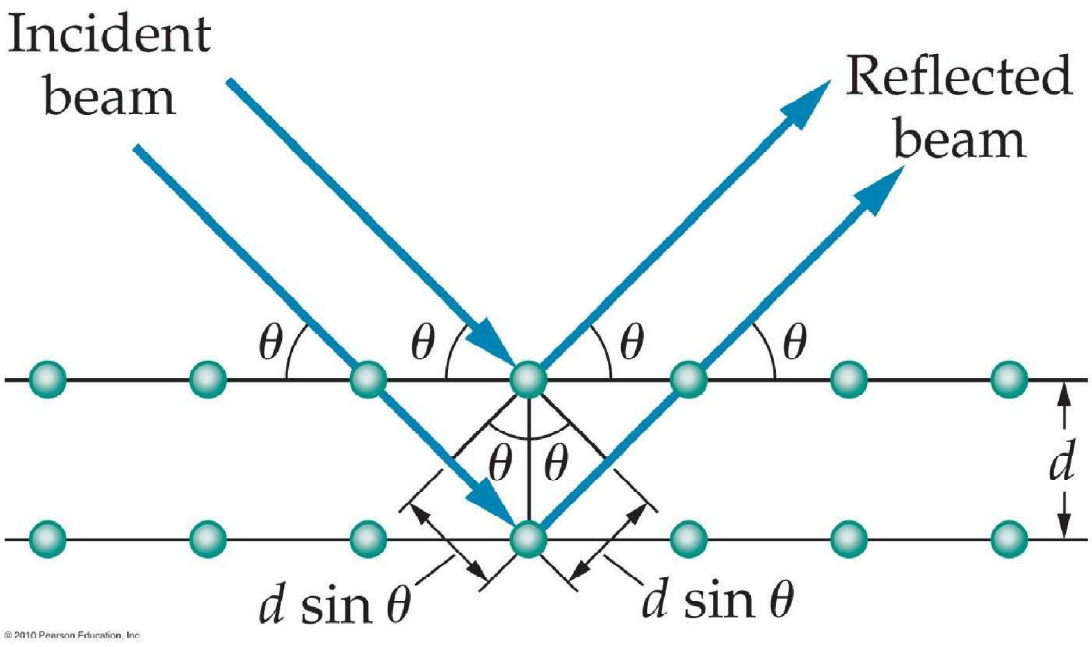

Figure (II.5): *Schematic illustration of X-ray reflections from parallel atomic planes in a crystal lattice, showing the geometric basis of Bragg's law.*

II.3. Results and Discussion

II.3.1. Reduction of Ions and Involved Mechanism

In the present work, $ZnFe_2O_4$ spinel ferrite nanoparticles were synthesized through the co-precipitation method, using zinc acetate dihydrate $Zn(CH_3COO)_2 \cdot 2H_2O$ and iron(III) chloride hexahydrate $FeCl_3 \cdot 6H_2O$ as the respective metal ion sources, with sodium hydroxide (NaOH) serving simultaneously as the precipitating agent and pH regulator. The synthesis proceeds through a sequence of well-defined chemical steps, beginning with the dissociation of the precursor salts in aqueous solution, followed by the co-precipitation of mixed metal hydroxides under alkaline

conditions, and culminating in a high-temperature calcination step that drives the transformation into the crystalline spinel phase [17].

II.3.1.1. Mechanism

Upon dissolution in deionized water, zinc acetate dihydrate dissociates completely into free zinc cations and acetate anions according to **(Eq (II.5))**:

$$Zn(CH_3COO)_2 \cdot 2H_2O \rightarrow Zn^{2+} + 2CH_3COO^- + 2H_2O \qquad (II.5)$$

Similarly, iron(III) chloride hexahydrate dissociates in aqueous solution to release trivalent iron cations and chloride anions, as shown in **(Eq (II.6))**:

$$FeCl_3 \cdot 6H_2O \rightarrow Fe^{3+} + 3Cl^- + 6H_2O \qquad (II.6)$$

When the NaOH solution is introduced dropwise into the mixed precursor solution and the pH is gradually raised to 11, the Zn^{2+} and Fe^{3+} ions react simultaneously with the hydroxide ions OH^- to form their respective metal hydroxide precipitates. This co-precipitation is highly sensitive to the local pH, and maintaining a stable alkaline environment throughout the addition is essential to ensure the complete and homogeneous precipitation of both metal species. The individual precipitation reactions are expressed in **(Eq (II.7))** and **(Eq (II.8))** [1]:

$$Zn^{2+} + 2OH^- \rightarrow Zn(OH)_2 \downarrow \qquad (II.7)$$

$$Fe^{3+} + 3OH^- \rightarrow Fe(OH)_3 \downarrow \qquad (II.8)$$

The immediate appearance of a reddish-brown precipitate upon NaOH addition is primarily attributed to the formation of $Fe(OH)_3$, which is well known to exhibit this characteristic color in alkaline aqueous media. At pH = 11, the supersaturation threshold is fully exceeded for both Zn^{2+} and Fe^{3+} ions, driving their quantitative and simultaneous removal from solution. Maintaining this highly alkaline environment is equally important for preventing the preferential or sequential precipitation of one hydroxide before the other, which would otherwise lead to cation segregation and compositional inhomogeneity in the final product [18]. The overall co-precipitation reaction leading to the formation of the mixed hydroxide precursor can be written as **(Eq (II.9))**:

$$Zn^{2+} + 2Fe^{3+} + 8OH^- \rightarrow Zn(OH)_2 + 2Fe(OH)_3 \downarrow \qquad (II.9)$$

II.3.1.2. Calcination

Calcination is a thermal decomposition process carried out at elevated temperatures to induce phase transformation and eliminate chemically bound water and hydroxyl groups from precursor compounds. In this study, the co-precipitated mixed hydroxide precursor was dried at 100 °C for 24 hours and subsequently calcined at 800 °C for 4 hours in a muffle furnace. During this thermal treatment, the zinc and iron hydroxides decompose and react with one another in the solid state, providing the atomic mobility necessary for cation diffusion into the tetrahedral and octahedral sites of the spinel lattice. The overall transformation reaction is described by **(Eq (II.10))** [19]:

$$Zn(OH)_2 + 2Fe(OH)_3 \xrightarrow{800°C} ZnFe_2O_4 + 4H_2O \qquad (\boldsymbol{II.10})$$

This calcination step is absolutely critical in the synthesis protocol. Beyond simply removing residual hydroxyl groups and physisorbed water, it provides the thermal energy required to complete the solid-state diffusion of Zn^{2+} and Fe^{3+} cations into their respective crystallographic sites within the spinel structure. The temperature of 800 °C was specifically chosen based on reported literature values for $ZnFe_2O_4$, as it represents a threshold above which a well-crystallized, phase-pure spinel product is reliably obtained without excessive grain growth. The calcination temperature also directly governs the mean crystallite size, the degree of crystallinity, and the inversion parameter of the spinel lattice, all of which have a direct bearing on the magnetic and optical properties of the final material. The structural and optical outcomes of this thermal treatment will be discussed in detail through the XRD and UV-Vis characterization results presented in the following sections.

II.3.2. Characterization of Zinc Ferrite Nanoparticles

In this work, three approaches were applied to characterize the novel compound $ZnFe_2O_4$ NPs. The optical characteristics of the compound were determined using ultraviolet-visible spectroscopy, functional groups and molecular interactions were elucidated using Fourier-transform infrared spectroscopy, and the structure was revealed using X-ray diffraction.

II.3.2.1. Optical Characterization

II.3.2.1.1. UV-Visible Absorption Spectrometer

The UV-Vis absorption spectrum recorded for the synthesized $ZnFe_2O_4$ nanoparticles over the wavelength range of 200 to 900 nm is presented in **Figure (II.6a)**. The spectrum reveals a broad and relatively intense absorption extending from the ultraviolet region into the visible range, with a distinct absorption feature centered at approximately 345 nm. This absorption band is characteristic of $ZnFe_2O_4$ and is generally attributed to ligand-to-metal charge transfer transitions involving Fe^{3+} ions in the spinel lattice, as well as to electronic transitions associated with the octahedral and tetrahedral crystal field environments of the iron cations [20]. The gradual and continuous decrease in absorbance toward longer wavelengths, without a sharp absorption edge, is consistent with the semiconducting nature of $ZnFe_2O_4$ and reflects the contribution of multiple overlapping electronic transitions within the spinel structure [21].

To determine the optical bandgap energy of the synthesized nanoparticles, the Tauc plot method was applied using the following relation (**Eq (II.11)**):

$$(\alpha h\nu)^2 = A(h\nu - E_g) \qquad \textbf{(II. 11)}$$

where α is the absorption coefficient, hν is the photon energy, A is a proportionality constant, and Eg is the optical bandgap energy. The value of $(\alpha h\nu)^2$ was plotted as a function of photon energy hν, and the bandgap was extracted by extrapolating the linear portion of the curve to the energy axis at $(\alpha h\nu)^2 = 0$, as illustrated in **Figure (II.6b)**. The estimated optical bandgap energy of the $ZnFe_2O_4$ nanoparticles was found to be **Eg = 2.5 eV**. This value falls well within the range reported in the literature for spinel zinc ferrite nanoparticles, where bandgap values typically lie between 1.9 and 2.7 eV depending on the synthesis route, calcination temperature, crystallite size, and degree of cation inversion [22]. The relatively moderate bandgap of 2.5 eV positions $ZnFe_2O_4$ as a promising visible-light-active semiconductor, with potential applications in photocatalytic degradation of organic pollutants, solar energy conversion, and optoelectronic devices.

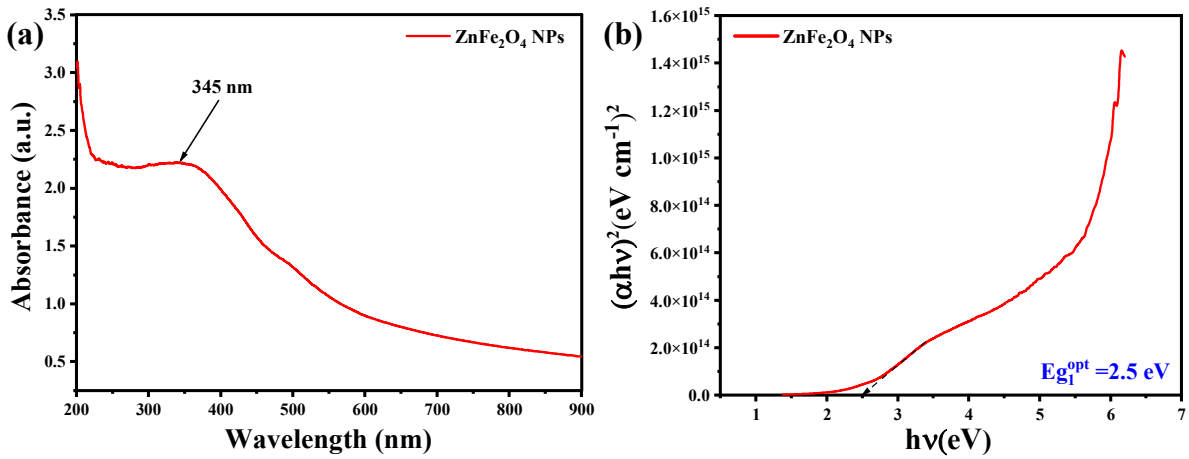

Figure (II.6): *Optical properties of $ZnFe_2O_4$ nanoparticles: (a) UV-Vis absorption spectrum; (b) Tauc plot for the determination of the direct optical bandgap energy.*

II.3.2.1.2. Fourier Transform Infrared Spectroscopy (FTIR):

The FTIR spectrum of the synthesized $ZnFe_2O_4$ nanoparticles was recorded over the wavenumber range of 400 to 4000 cm^{-1} and is presented in **Figure (II.7)**. The spectrum displays a number of well-defined absorption bands whose positions and assignments provide direct evidence for the formation of the spinel ferrite phase, as well as information about residual surface species arising from the synthesis process.

The most prominent and diagnostically significant absorption bands appear in the low-wavenumber fingerprint region. A strong absorption band observed at 531 cm^{-1} is assigned to the stretching vibration of metal–oxygen bonds at tetrahedral sites (A-sites) within the spinel lattice, where zinc cations preferentially reside in the normal spinel configuration of $ZnFe_2O_4$ [12]. A second, equally intense absorption band located at 432 cm^{-1} is attributed to the stretching vibration of metal–oxygen bonds at octahedral sites (B-sites), which are predominantly occupied by Fe^{3+} ions [23]. The simultaneous presence of these two characteristic bands, one above and one below 500 cm^{-1}, constitutes the definitive infrared fingerprint of the spinel ferrite structure and unambiguously confirms the successful formation of the $ZnFe_2O_4$ phase following calcination at 800 °C. These assignments are fully consistent with those reported by Waldron for spinel ferrites and with subsequent studies on co-precipitated zinc ferrite nanoparticles [12], [23].

Moving toward higher wavenumbers, the band observed at 864 cm^{-1} is tentatively attributed to bending vibrations of metal–oxygen–metal linkages within the spinel framework, a feature

occasionally reported in ferrite nanoparticles and associated with distortions in the local coordination environment of the cations [24]. The absorption features appearing at 1212 cm^{-1} and 1370 cm^{-1} are assigned to C–O and C–H bending vibrations, respectively, and are most likely associated with residual organic species originating from the acetate precursor used during synthesis, namely zinc acetate dihydrate [25]. A band at 1450 cm^{-1} corresponds to the asymmetric stretching of carboxylate groups (COO^-), further supporting the presence of trace acetate-derived surface species that were not fully eliminated during the washing and calcination steps [25]. The absorption band at 1736 cm^{-1} is assigned to the C=O stretching vibration of carbonyl groups, which may arise from partially decomposed or surface-adsorbed organic residues [26].

In the higher wavenumber region, two weak absorption features are detected at 2317 cm^{-1} and 2371 cm^{-1}, which are commonly associated with atmospheric CO_2 adsorbed on the surface of the nanoparticles during sample preparation and measurement [27]. The band at 2982 cm^{-1} is attributed to C–H stretching vibrations of methyl or methylene groups, again consistent with residual organic contamination from the precursor compounds [25]. Finally, the broad absorption band centered at 3745 cm^{-1} is assigned to the stretching vibration of isolated or free surface hydroxyl groups (O–H stretching), indicating the presence of residual hydroxyl species on the nanoparticle surface that were not fully converted during the thermal treatment [28]. The relatively low intensity of this band suggests that the calcination at 800 °C was largely effective in driving the dehydroxylation reaction to near completion.

Taken together, the FTIR spectrum of the synthesized $ZnFe_2O_4$ nanoparticles provides compelling spectroscopic evidence for the successful formation of the spinel phase, as confirmed by the characteristic dual-band signature at 531 and 432 cm^{-1}, while the remaining absorption features reflect minor surface contamination that is commonly encountered in co-precipitated nanoparticles and does not compromise the phase purity of the material [10].

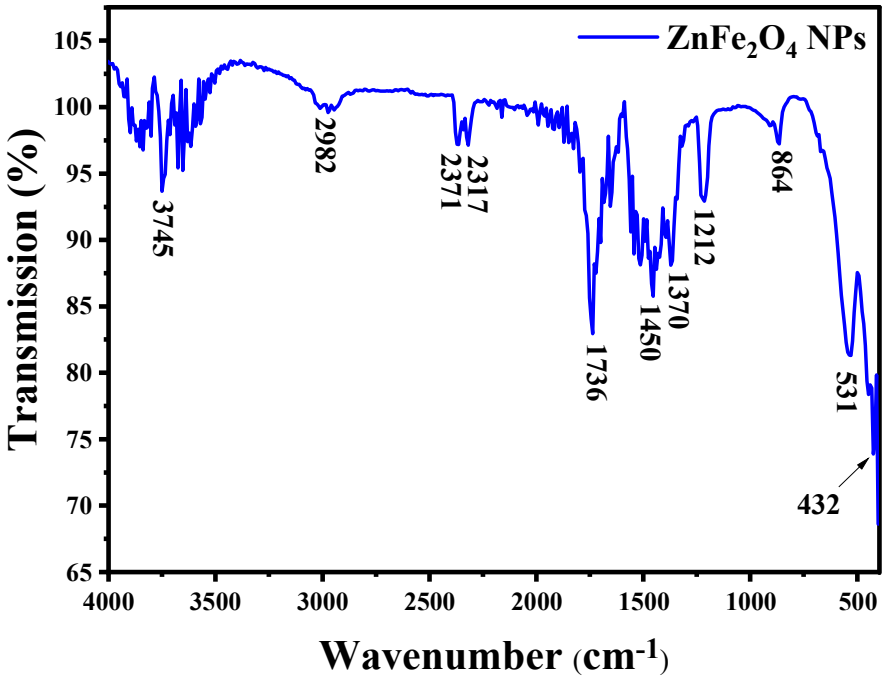

Figure (II.7): *FTIR spectrum of $ZnFe_2O_4$ nanoparticles recorded in the range of 400–4000 cm^{-1}*

II.3.2.2. Structural and Morphological Properties:

The structural characterization of the synthesized $ZnFe_2O_4$ nanoparticles was carried out using X-ray diffraction analysis, which represents the most direct and reliable tool for confirming phase formation and extracting quantitative structural parameters from nanocrystalline powders.

II.3.2.2.1. X-ray Diffraction (XRD) :

The XRD pattern recorded for the synthesized $ZnFe_2O_4$ nanoparticles is shown in **Figure (II.8)**. The diffractogram displays a series of sharp, well-resolved, and relatively intense diffraction peaks distributed across the entire angular range from approximately 15° to 90° (2θ), all of which were successfully indexed to the pure cubic spinel structure of zinc ferrite. Bragg's reflection peaks are observed at 2θ values of 18.3°, 29.9°, 35.3°, 37.1°, 43.0°, 53.2°, 56.8°, 62.3°, 70.8°, 74.0°, 74.7°, 86.9°, and 89.9°, corresponding to the (111), (220), (311), (222), (400), (422), (511), (440), (620), (533), (622), (642), and (731) crystal planes, respectively. These findings align with the Joint Committee on Powder Diffraction Standards (JCPDS Card N°. 00-001-1108), confirming a cubic crystal system with space group $Fd\bar{3}m$ (space group number 227) and lattice parameters a = b = c = 8.4300 Å [29].

The complete absence of any extraneous diffraction peaks attributable to secondary phases such as α-Fe_2O_3, ZnO, or FeOOH confirms that the calcination treatment carried out at 800 °C for 4 hours was fully effective in driving the solid-state reaction to completion, yielding a phase-pure spinel ferrite product [30].

The most intense diffraction peak corresponds to the (311) reflection at $2\theta \approx 35.3°$, with an interplanar spacing of d = 2.54 Å and a relative intensity of 100% according to the JCPDS reference data. This reflection is universally recognized as the fingerprint peak of the spinel structure and was used as the reference peak for crystallite size estimation. Its sharpness and high intensity, alongside the well-defined profiles of all remaining reflections, are strong indicators of a high degree of crystallinity in the synthesized material, which is directly attributable to the elevated calcination temperature employed in this work [1]. In the normal spinel configuration adopted by $ZnFe_2O_4$, zinc cations (Zn^{2+}) preferentially occupy the tetrahedral A-sites, while iron cations (Fe^{3+}) are exclusively distributed over the octahedral B-sites of the $Fd\bar{3}m$ structure, a cation arrangement that governs the magnetic, optical, and electronic properties of the compound [18].

The mean crystallite size of the $ZnFe_2O_4$ nanoparticles was estimated from the broadening of the most intense (311) diffraction peak using the Scherrer equation introduced in the previous section (**Eq (II.4)**), yielding an average crystallite size of D = 26.74 ± 0.50 nm. This value falls well within the range reported in the literature for $ZnFe_2O_4$ nanoparticles prepared by co-precipitation and calcined at comparable temperatures [3]. The narrow size distribution reflected by the small uncertainty of ±0.50 nm attests to the homogeneity of the synthesis and the good reproducibility of the co-precipitation protocol. It is also worth noting that the crystallite size obtained in the present work is somewhat larger than values typically reported for samples calcined at lower temperatures, a trend that is well understood in terms of thermally activated solid-state diffusion and grain coalescence, both of which become increasingly significant as the calcination temperature rises above 600 °C [31].

Taken together, the XRD results provide conclusive and comprehensive evidence for the successful formation of single-phase, well-crystallized $ZnFe_2O_4$ spinel ferrite nanoparticles with a cubic $Fd\bar{3}m$ structure, a lattice parameter of 8.4300 Å, and a mean crystallite size of approximately 26.74 nm, fully validating the effectiveness of the co-precipitation route combined with high-temperature calcination for the controlled synthesis of this material.

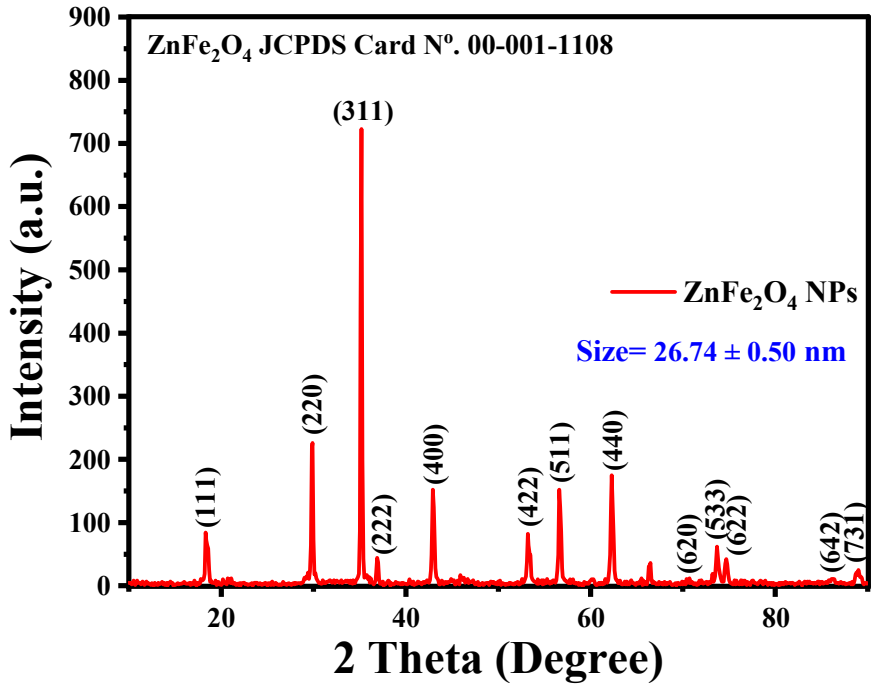

Figure (II.8): *X-ray diffraction pattern of $ZnFe_2O_4$ nanoparticles indexed according to JCPDS Card Nº. 00-001-1108*

II.4. Conclusion

In this chapter, $ZnFe_2O_4$ spinel ferrite nanoparticles were successfully synthesized via the co-precipitation method using zinc acetate dihydrate and iron(III) chloride hexahydrate as precursor salts, with sodium hydroxide serving as the precipitating agent and pH regulator. The synthesis protocol involved careful control of the pH at 11, an aging step at 80 °C for 2 hours, followed by drying at 100 °C and final calcination at 800 °C for 4 hours. The combination of these carefully optimized conditions proved effective in producing a phase-pure, well-crystallized spinel ferrite product, as confirmed by the three complementary characterization techniques employed in this work.

The structural analysis carried out by X-ray diffraction provided the most direct confirmation of the synthesis outcome. All diffraction peaks observed in the XRD pattern were successfully indexed to the cubic spinel structure of $ZnFe_2O_4$ in accordance with JCPDS Card Nº. 00-001-1108, with no detectable secondary phases present in the final product. The mean crystallite size estimated from the broadening of the most intense (311) reflection using the Scherrer equation was found to be 26.74 ± 0.50 nm, indicating a nanocrystalline material with a narrow size

distribution and a high degree of crystallinity consistent with the elevated calcination temperature applied.

The FTIR spectrum recorded for the synthesized nanoparticles further corroborated the XRD findings by revealing the two characteristic metal–oxygen stretching vibration bands at 531 cm^{-1} and 432 cm^{-1}, which are the definitive infrared fingerprint of the spinel ferrite phase, corresponding to metal–oxygen bond vibrations at tetrahedral and octahedral sites, respectively. Additional absorption features observed at higher wavenumbers were attributed to residual surface hydroxyl groups and minor organic species from the precursors, none of which compromise the phase purity of the material.

The optical characterization performed by UV-Vis absorption spectroscopy revealed a characteristic absorption feature at 345 nm, attributed to ligand-to-metal charge transfer transitions involving Fe^{3+} ions within the spinel lattice. The optical bandgap energy of the synthesized $ZnFe_2O_4$ nanoparticles was determined from the Tauc plot to be 2.5 eV, a value that places this material within the category of visible-light-active semiconductors and suggests its potential suitability for applications in photocatalysis, environmental remediation, and optoelectronic devices.

Taken together, the results obtained in this chapter demonstrate that the co-precipitation route, when combined with an appropriate calcination treatment, represents a simple, scalable, and reliable approach for the controlled synthesis of $ZnFe_2O_4$ spinel ferrite nanoparticles with well-defined structural, spectroscopic, and optical properties. Future work could focus on investigating the effect of calcination temperature and precursor stoichiometry on the cation distribution and magnetic properties of the material, as well as evaluating its photocatalytic performance toward the degradation of organic pollutants under visible light irradiation.

References

References

1. Maaz K, Mumtaz A, Hasanain SK, Ceylan A (2007) Synthesis and magnetic properties of cobalt ferrite (CoFe2O4) nanoparticles prepared by wet chemical route. J Magn Magn Mater 308:289–295. https://doi.org/10.1016/j.jmmm.2006.06.003

2. Sivakumar N, Narayanasamy A, Ponpandian N, Govindaraj G (2007) Grain size effect on the dielectric behavior of nanostructured Ni0.5Zn0.5Fe2O4. J Appl Phys 101:. https://doi.org/10.1063/1.2721379

3. Amiri S, Shokrollahi H (2013) The role of cobalt ferrite magnetic nanoparticles in medical science. Mater Sci Eng C 33:1–8. https://doi.org/10.1016/j.msec.2012.09.003

4. Vinosha PA, Mely LA, Jeronsia JE, et al (2017) Synthesis and properties of spinel ZnFe2O4 nanoparticles by facile co-precipitation route. Optik (Stuttg) 134:99–108. https://doi.org/10.1016/j.ijleo.2017.01.018

5. Ashok K, Usha P, R. N, et al (2024) Multifunctional Characterization and Anticancer Properties of Magnetic Zinc Ferrite Nanoparticles by Modified Ultrasonic Assisted Co-precipitation Method. ECS J Solid State Sci Technol 13:083011. https://doi.org/10.1149/2162-8777/ad71f2

6. Tiwari JN, Tiwari RN, Kim KS (2012) Zero-dimensional, one-dimensional, two-dimensional and three-dimensional nanostructured materials for advanced electrochemical energy devices. Prog Mater Sci 57:724–803. https://doi.org/10.1016/j.pmatsci.2011.08.003

7. Hanlan J, Skoog DA, West DM (1973) Principles of Instrumental Analysis. Saunders college publishing Philadelphia

8. Swinehart DF (1962) The Beer-Lambert law. J Chem Educ 39:333–335. https://doi.org/10.1021/ed039p333

9. Tauc J, Grigorovici R, Vancu A (1966) Optical Properties and Electronic Structure of Amorphous Germanium. Phys Status Solidi 15:627–637. https://doi.org/10.1002/pssb.19660150224

10. Griffiths PR, De Haseth JA (2006) Fourier Transform Infrared Spectrometry: Second Edition. Wiley

11. Mohan J (2004) Organic spectroscopy: principles and applications. Alpha Science Int'l Ltd.

12. Waldron RD (1955) Infrared spectra of ferrites. Phys Rev 99:1727–1735. https://doi.org/10.1103/PhysRev.99.1727

13. Bard AJ (2010) Encyclopedia of Electrochemistry. In: Encyclopedia of Electrochemistry. Wiley-VCH, pp 1–7720

14. Röntgen WC (1896) On a new kind of rays. Science (80-) 3:227–231. https://doi.org/10.1126/science.3.59.227

15. Cullity BD, Stock SR (2001) Elelments of X-ray Diffraction. Prentice-Hall

16. Paul Scherrer (1918) Nachrichten von der Gesellschaft der Wissenschaften zu Göttingen. Math Klasse 1:98–100

17. Kombaiah K, Vijaya JJ, Kennedy LJ, Bououdina M (2017) Optical, magnetic and structural properties of ZnFe2O4 nanoparticles synthesized by conventional and microwave assisted combustion method: A comparative investigation. Optik (Stuttg) 129:57–68. https://doi.org/10.1016/j.ijleo.2016.10.058

18. Carta D, Casula MF, Falqui A, et al (2009) A Structural and magnetic investigation of the inversion degree in ferrite nanocrystals mfe2o4 (M = Mn, Co, Ni). J Phys Chem C 113:8606–8615. https://doi.org/10.1021/jp901077c

19. Andhare DD, Jadhav SA, Khedkar M V, et al (2020) Structural and Chemical Properties of ZnFe2O4 Nanoparticles Synthesised by Chemical Co-Precipitation Technique. J Phys Conf Ser 1644:012014. https://doi.org/10.1088/1742-6596/1644/1/012014

20. Vinosha PA, Mely LA, Jeronsia JE, et al (2017) Study of Structural, Optical, Dielectric and Magnetic Properties of Zinc Ferrite Synthesized by Co-Precipitation. Nano Hybrids Compos 17:1–9. https://doi.org/10.4028/www.scientific.net/nhc.17.1

21. Zhang R, Qin C, Bala H, et al (2023) Recent Progress in Spinel Ferrite (MFe2O4) Chemiresistive Based Gas Sensors. Nanomaterials 13:2188. https://doi.org/10.3390/nano13152188

22. Chandrika M, Ravindra A V., Rajesh C, et al (2019) Studies on structural and optical properties of nano ZnFe 2 O 4 and ZnFe 2 O 4 -TiO 2 composite synthesized by co-

precipitation route. Mater Chem Phys 230:107–113. https://doi.org/10.1016/j.matchemphys.2019.03.059

23. Manohar A, Kim KH (2025) Effect of calcination temperature on the structural, magnetic, and surface characteristics of quaternary $CaFe_2O_4$/$CuFe_2O_4$/$ZnFe_2O_4$/$NiFe_2O_4$ ferrite nanocomposites. Appl Phys A Mater Sci Process 131:730. https://doi.org/10.1007/s00339-025-08815-1

24. Mahmoud MH, Hassan AM, Said AEAA, Taha TA (2022) Structural, magnetic, and catalytic studies of microwave-combustion/ball-mill synthesized zinc ferrite nanoparticles. Inorg Chem Commun 144:109932. https://doi.org/10.1016/j.inoche.2022.109932

25. Nakamoto K (2008) Infrared and Raman Spectra of Inorganic and Coordination Compounds: Part B: Applications in Coordination, Organometallic, and Bioinorganic Chemistry. Wiley

26. Stuart BH (2005) Infrared Spectroscopy: Fundamentals and Applications. Wiley

27. Smith BC (2011) Fundamentals of fourier transform infrared spectroscopy, second edition. CRC Press

28. Zaki MI, Hasan MA, Al-Sagheer FA, Pasupulety L (2001) In situ FTIR spectra of pyridine adsorbed on SiO2-Al2O3, TiO2, ZrO2 and CeO2: General considerations for the identification of acid sites on surfaces of finely divided metal oxides. Colloids Surfaces A Physicochem Eng Asp 190:261–274. https://doi.org/10.1016/S0927-7757(01)00690-2

29. Kumar BU, Ramesh T, Kumar KK, et al (2026) Structural, Optical, Magnetic and Dielectric Properties of Europium Substituted Zinc Ferrite Nanostructures Synthesized By Coprecipitation Method. J Supercond Nov Magn 39:59. https://doi.org/10.1007/s10948-026-07139-2

30. Hasanpoor M, Aliofkhazraei M, Delavari H (2015) Microwave-assisted Synthesis of Zinc Oxide Nanoparticles. Procedia Mater Sci 11:320–325. https://doi.org/10.1016/j.mspro.2015.11.101

31. Šutka A, Gross KA (2016) Spinel ferrite oxide semiconductor gas sensors. Sensors Actuators, B Chem 222:95–105. https://doi.org/10.1016/j.snb.2015.08.027

CHAPTER III
Study of Efficient Heavy Metals Removal

III.1. Heavy Metal Contamination in Industrial Petroleum Wastewater

From a scientific standpoint, any metallic element with a density exceeding 5 g/cm³ falls under the category of heavy metals. While numerous elements meet this criterion, only a specific subset carries considerable environmental relevance, as outlined in **Table (III.1)**. It is worth noting that arsenic, though technically a metalloid, is conventionally grouped with hazardous heavy metals due to its comparable toxic behavior.

The health consequences associated with prolonged or acute exposure to heavy metals are both varied and severe. These range from stunted growth and developmental abnormalities, particularly in younger populations, to organ failure, neurological deterioration, and in the most extreme cases, death. Certain metals such as lead and mercury have been linked to autoimmune responses, whereby the body's own immune defenses begin attacking healthy cells and tissues. The downstream effects of such dysfunction may manifest as renal failure, cardiovascular complications, and neurological disorders, with fetal brain development being among the most vulnerable targets. Conditions like rheumatoid arthritis have also been associated with chronic metal exposure. At sufficiently elevated concentrations, some heavy metals are capable of inducing irreversible brain damage. Children represent a particularly at-risk demographic, not only due to their developing physiology but also because their food intake relative to body mass is proportionally greater than that of adults, which amplifies their dietary metal exposure.

In response to these well-documented risks, regulatory frameworks governing wastewater discharge were established with the explicit goal of limiting human and environmental exposure to toxic substances. These regulations define permissible thresholds for the types and quantities of heavy metals allowed in effluent streams. **Table (III.1)** presents the Maximum Contaminant Levels (MCL) designated by the United States Environmental Protection Agency (USEPA) for the most environmentally significant heavy metals [1].

Table (III.1): *Health Effects and USEPA Maximum Contaminant Levels (MCL) of Key Heavy Metals in Aquatic Environments*

Heavy Metal	Associated Health Effects	MCL (mg/L)
Arsenic	Dermal lesions, internal organ cancers, vascular disorders	0.050
Cadmium	Renal dysfunction, kidney tissue damage, carcinogenic potential	0.01
Chromium	Headache, gastrointestinal distress, nausea, vomiting, carcinogenicity	0.05
Copper	Hepatic damage, Wilson's disease, sleep disturbances	0.25
Nickel	Skin irritation, respiratory complications, chronic asthma, carcinogenic	0.20
Zinc	Depressive symptoms, fatigue, neurological impairments, excessive thirst	0.80
Lead	Fetal neurological damage, renal disease, cardiovascular and nervous system disorders	0.006
Mercury	Autoimmune arthritis, kidney failure, circulatory and neurological system damage	0.00003

III.1.1. Origins and Classification of Heavy Metals

III.1.1.1. Heavy Metal Sources

Heavy metals are introduced into the environment through two broad categories of processes: those occurring naturally and those driven by human activity. Regardless of their origin, these metals ultimately migrate into soil, water bodies, and the atmosphere, cycling continuously across these interconnected compartments, as illustrated in **Figure (III.1)** [2].

III.1.1.1.1. Geogenic and Natural Emission Pathways

A substantial body of scientific literature has identified and characterized the naturally occurring sources responsible for heavy metal mobilization in the environment. These emissions do not occur uniformly but are instead triggered under specific geochemical and atmospheric conditions, as depicted in **Figure (III.2)**. Among the most well-recognized natural release mechanisms are volcanic activity, sea spray aerosols, wildfires, the mechanical and chemical weathering of rock formations, biogenic cycling, and the atmospheric transport of dust-laden soil particles.

Through weathering and erosion, metals that were once locked within geological matrices are gradually liberated and redistributed across different environmental media. In terms of their chemical speciation, heavy metals exist in a variety of compound forms, including hydroxides, oxides, sulphides, sulphates, phosphates, silicates, and organically bound complexes.

Among the most environmentally widespread heavy metals are lead (Pb), nickel (Ni), chromium (Cr), cadmium (Cd), arsenic (As), mercury (Hg), zinc (Zn), and copper (Cu). Despite typically occurring at trace concentrations under natural conditions, these elements pose a non-negligible threat to human health and that of other mammals when accumulated beyond safe thresholds [2].

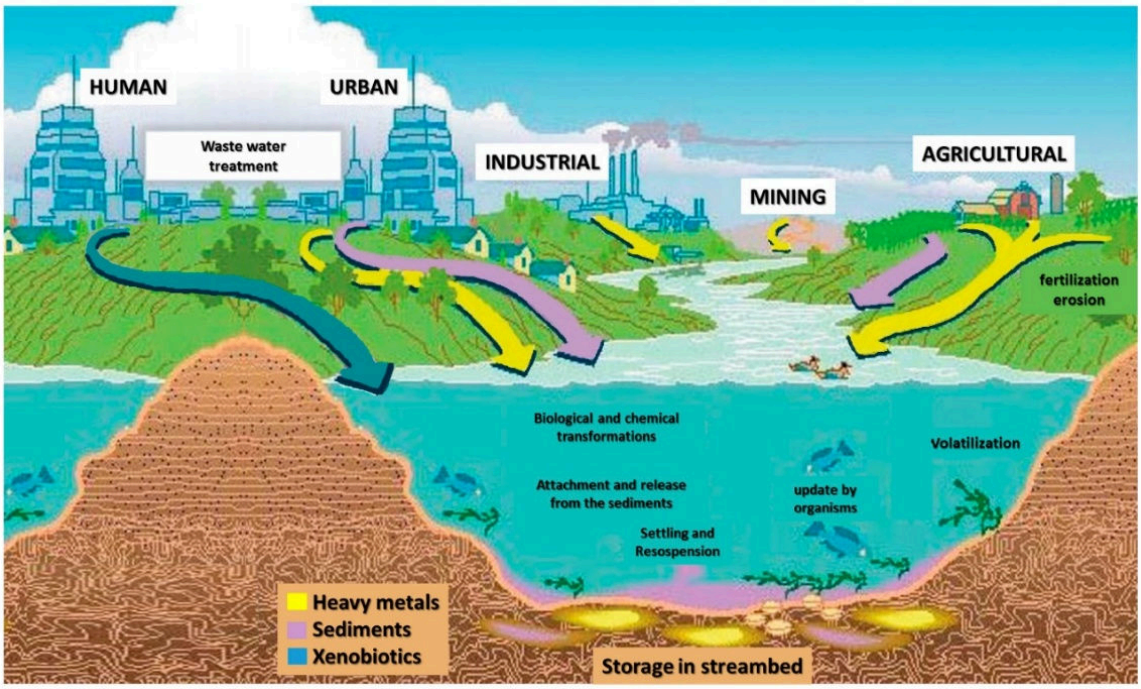

Figure (III.1): *Pathways of heavy metal input and accumulation across environmental compartments* [3].

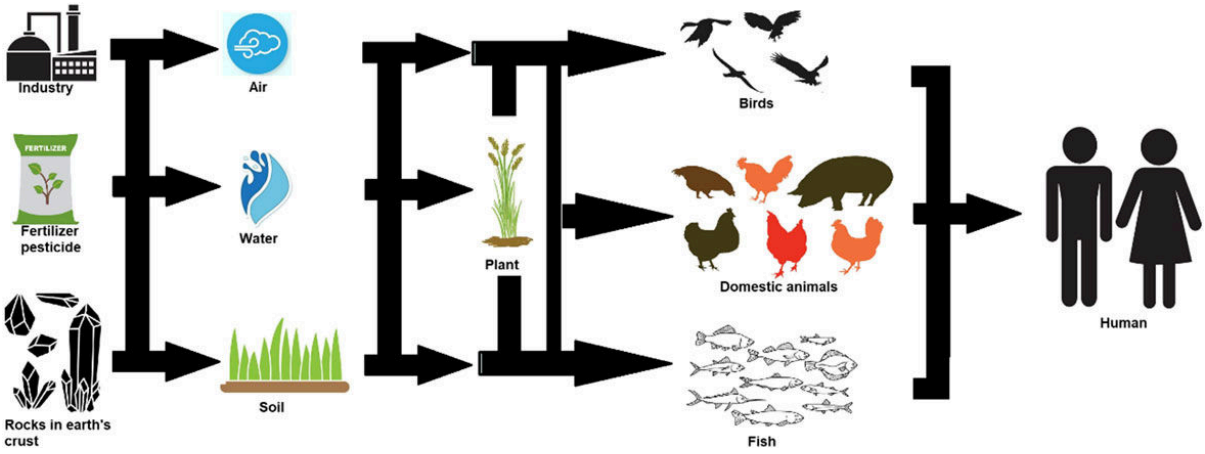

Figure (III.2): *Natural emission sources of heavy metals and their biogeochemical cycling in the environment* [4].

III.1.1.1.2. Human-Driven Contamination Pathways

Beyond natural processes, human industrial and agricultural activities represent a significant and often dominant source of heavy metal releases into the environment. Anthropogenic emissions have been shown to exceed natural metal fluxes for several elements, underscoring the disproportionate impact of human activity on global metal cycling. Notably, a considerable fraction of the metals detected in wind-transported dust particles can be traced back to industrial sites rather than purely geological origins.

Several well-documented anthropogenic sources contribute substantially to environmental heavy metal burdens. Vehicular exhaust emissions are a primary pathway for lead dispersal, while copper, zinc, and arsenic enter the environment largely through smelting operations. Agricultural applications of pesticides and herbicides account for significant arsenic inputs, and the combustion of fossil fuels releases nickel, vanadium, mercury, selenium, and tin into the atmosphere. Taken together, the relentless demand for manufactured goods driven by a growing global population has positioned human activity as the foremost driver of environmental metal contamination [2].

III.1.1.2. Heavy Metal Discharge from Key Industrial Sectors

A wide range of industrial activities generates effluent streams heavily loaded with toxic heavy metals. Among the most significant contributors are electroplating and metal surface treatment facilities, which produce large quantities of wastewater enriched with cadmium, zinc, lead, chromium, nickel, copper, vanadium, platinum, silver, and titanium. The operations involved in these processes span electroplating, electroless deposition, anodizing, conversion coating, chemical etching, surface cleaning, and precision milling [5].

The manufacture of printed circuit boards (PCBs) represents another substantial industrial source, where tin, lead, and nickel are predominantly used as protective and resistive plating layers [5]. Further contributions come from inorganic pigment production, which generates wastes containing chromium compounds and cadmium sulfide; petroleum refining operations, whose spent catalysts carry residual nickel, vanadium, and chromium; photovoltaic manufacturing, which yields films with elevated silver and ferrocyanide concentrations; and wood treatment facilities that generate arsenic-laden effluents from chromated copper-arsenate processes.

Collectively, these industrial sectors generate substantial volumes of contaminated wastewater, sludge, and sediment that are classified as hazardous waste, requiring intensive and

resource-demanding treatment before any environmentally safe discharge can occur [5]. As illustrated in **Figure (III.3)**, the pathway from industrial discharge to human exposure involves a series of ecological transfers, including uptake by plankton, bioaccumulation through the aquatic food chain, and ultimate risk to human health through contaminated drinking water and seafood consumption.

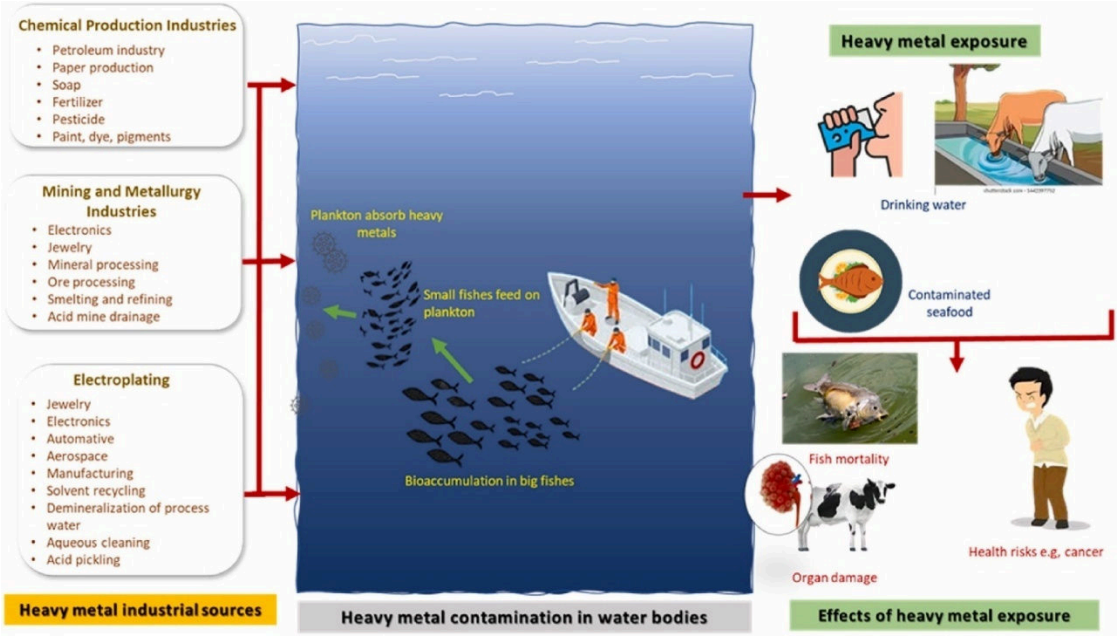

Figure (III.3): *Heavy metal transfer pathways from industrial discharge sources through aquatic ecosystems to human health exposure routes* [5].

III.1.1.3. Classification and Characteristics of Heavy Metals

Heavy metals vary considerably in their origins, chemical behavior, and toxicological profiles. The following discussion presents an integrated overview of the most environmentally and biologically significant heavy metals encountered in industrial and natural contexts (**Table (III.2)**).

Mercury (Hg) carries one of the longest histories of human exposure, having been traded and used as a decorative pigment since antiquity. While occupational poisoning was once widespread — particularly among miners and craftsmen who handled mercury daily — the modern concern has shifted toward environmental contamination. Industrial discharge into water bodies and the agricultural use of mercurial fungicides have led to mercury accumulation in aquatic ecosystems, where fish serve as the primary vector of human exposure [6].

Cadmium (Cd), by contrast, is largely a product of modern industry. Although limited historical exposure may have occurred in populations living on cadmium-rich soils or consuming contaminated water, significant health consequences — particularly renal damage — generally require sustained high-level exposure of the kind associated with occupational settings [6].

Lead (Pb) has accompanied human civilization for over four millennia, initially valued as a byproduct of silver extraction. Its widespread use in Roman plumbing, wine preservation, and various manufacturing processes ensured chronic population-level exposure throughout history. The metal's solubility in biological fluids makes it particularly hazardous, and its toxicological legacy continues to inform modern environmental policy [6].

Chromium (Cr) has become an increasingly prominent environmental concern in the wake of rapid industrial expansion, particularly in the chemical and leather tanning sectors. Hexavalent chromium, the most dangerous oxidation state, is both highly soluble in biological tissues and strongly carcinogenic. Its extensive use across metallurgical, refractory, and tannery industries has made it a persistent contaminant in both soil and water [7].

Iron (Fe), while essential to biological systems, is classified among the transition heavy metals. It functions as a redox agent in respiratory enzymes and plays a central role in oxygen and electron transport through iron-containing proteins. Storage proteins such as ferritin and albumin regulate iron homeostasis in humans and other higher organisms [7].

Nickel (Ni) is recognized for its role in plant and soil biochemistry, and appears to be essential for the growth of marine microalgae. However, excessive nickel intake — even at relatively modest concentrations — can interfere with iron absorption and disrupt hepatic enzyme activity. Epidemiological studies have consistently linked occupational inhalation of nickel dust to elevated risks of nasal and pulmonary cancers [7].

Copper (Cu) is one of the most historically utilized metals, finding applications across construction, agriculture, and electrical engineering since the ninth century. Its environmental presence stems from both natural geological processes and human activities such as mining, smelting, and pesticide use. Overexposure to copper can result in liver and kidney damage, hemolysis, and gastrointestinal inflammation, and its non-biodegradable nature allows it to accumulate persistently within living organisms [8].

Zinc (Zn) is widely distributed in the environment and plays a crucial role in plant metabolism, enzyme function, and auxin synthesis. Deficiency in zinc leads to identifiable

symptoms such as leaf chlorosis in plants and metabolic disruption in animals. Despite its biological necessity, elevated zinc concentrations can result in intestinal toxicity and metabolic imbalance [7].

Arsenic (As) is naturally present in soils at average concentrations of 2–5 mg/kg, with volcanic activity representing its most significant natural atmospheric source. Anthropogenic activities — including smelting, mining, and industrial discharge — substantially amplify arsenic mobilization. In natural water systems, arsenic contamination predominantly originates from the weathering of arsenic-bearing minerals, particularly arsenopyrite (FeAsS), the most abundant arsenic-containing mineral in nature [9].

Table (III.2): Summary of Key Heavy Metals — Origins, Applications, and Primary Health Effects

Heavy Metal	Main Sources	Key Industrial Uses	Primary Health Effects	Ref.
Mercury (Hg)	Industrial discharge, fungicides, mining	Pigments, instruments	Neurological damage, environmental poisoning	[6]
Cadmium (Cd)	Cadmium-rich soils, lead ore processing	Modern manufacturing	Renal damage, kidney dysfunction	[6]
Lead (Pb)	Mining, plumbing, fossil fuels	Silver extraction, construction	Brain damage, cardiovascular disorders	[6]
Chromium (Cr)	Electroplating, tanning, steel industry	Metallurgy, leather tanning	Carcinogenicity, tissue solubility	[7]
Iron (Fe)	Earth's crust, seawater	Biological enzyme systems	Oxidative stress at high concentrations	[7]
Nickel (Ni)	Soil, industrial dust	Alloys, electronics	Nasal and pulmonary cancer risk	[7]
Copper (Cu)	Mining, smelting, pesticides	Electrical wiring, plumbing	Liver/kidney damage, hemolysis	[8]
Zinc (Zn)	Soil, industrial processes	Enzyme cofactor, agriculture	Intestinal toxicity at high levels	[7]
Arsenic (As)	Volcanic activity, smelting, mining	Pesticides, wood treatment	Carcinogenicity, vascular disease	[9]

III.1.2. Environmental and Toxicological Consequences of Heavy Metal Contamination

III.1.2.1 Toxic Profiles of Selected Heavy Metals

Of the 92 naturally occurring elements, approximately 30 have been identified as carrying measurable toxic potential toward human health. These elements arise through both geological and anthropogenic processes, though industrial discharge stands out as a particularly significant and controllable emission pathway. The contamination cycle associated with heavy metals is well established: pollutants originating from industrial operations are progressively transferred through the atmosphere, soil, and water systems before ultimately entering the food chain and reaching human populations. An important nuance in toxicology is that heavy metals do not require high concentrations to be harmful — even trace-level exposures can produce adverse biological effects under certain conditions. The dimensions of human exposure, uptake, and metabolic absorption have been emphasized as areas of growing concern, particularly in industrialized nations [7].

III.1.2.2. Mechanisms of Biological and Environmental Disruption

At the biochemical level, heavy metals exert their toxic effects primarily through their affinity for sulfhydryl groups and their capacity to generate reactive oxygen species (ROS). These interactions trigger a cascade of damaging cellular events, including oxidative stress, glutathione depletion, and the functional inactivation of critical biological macromolecules. Once metals enter living organisms, they interfere with specific metabolic pathways, either by inhibiting essential enzymatic reactions or by mimicking natural substrates and disrupting normal signaling processes.

The downstream health consequences of such disruptions are wide-ranging and include the development of malignancies, metabolic disorders, immune dysregulation, endocrine disruption, organ-specific dysfunction, and congenital abnormalities. In recognition of these risks, numerous international regulatory bodies have established permissible thresholds for heavy metal concentrations in environmental media, food supplies, and drinking water sources. Risk assessment studies examining metal contamination in food and water have reported detectable concentrations in approximately 21% of analyzed samples [7].

III.1.2.3. Broad Environmental Impacts Across Natural Systems

The presence of heavy metals in the environment triggers a broad spectrum of adverse effects that extend well beyond individual organisms. All major environmental compartments are affected, including the hydrosphere, lithosphere, biosphere, and atmosphere, each serving as both a receptor and a vector for metal transport and accumulation. Disruption of ecological food webs is among the most consequential outcomes, as bioaccumulation through trophic levels amplifies metal concentrations far beyond what is present in the surrounding environment. Health deterioration and increased mortality rates in both wildlife and human populations persist until effective remediation measures are implemented. A comprehensive overview of the health-related impacts associated with heavy metal exposure is presented in **Figure (III.4)** [2, 10].

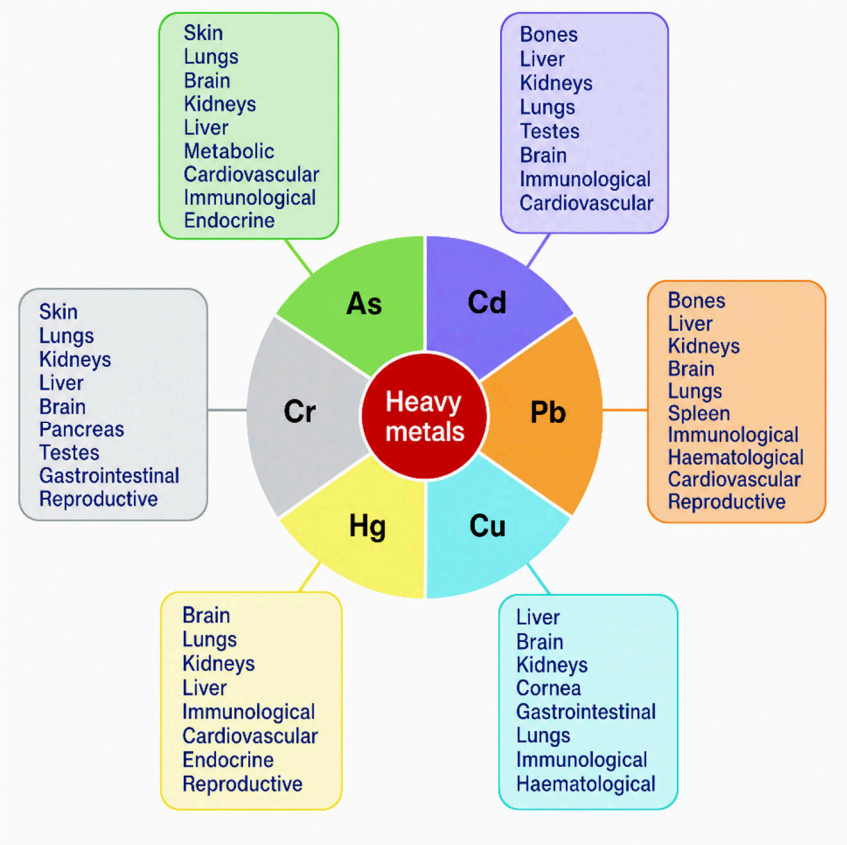

Figure (III.4): *Environmental consequences of heavy metal contamination across ecological and biological systems* [11].

III.1.2.4. Effects of Heavy Metal Contamination on Environmental Compartments

Growing industrial activity and population demands have elevated heavy metal contamination to a pressing global concern. The three primary environmental compartments affected are soil, water, and air [2].

III.1.2.4.1. Soil Contamination

Soils act as the principal sink for heavy metals released through mining operations, industrial effluents, sewage sludge, fertilizers, pesticides, and petrochemical spills. Unlike organic pollutants, heavy metals resist microbial and chemical degradation, allowing them to persist indefinitely and accumulate within food chains. Beyond their direct ecological toxicity, heavy metals alter fundamental soil properties — including pH, porosity, and natural chemistry — thereby compounding the environmental burden by simultaneously slowing the biodegradation of co-existing organic contaminants [2].

III.1.2.4.2. Water Contamination

Urban and industrial runoff are primary drivers of heavy metal accumulation in aquatic systems, where metals tend to concentrate in sediments. Even at trace concentrations, these metals pose serious risks to aquatic organisms and humans alike, as toxicity depends on exposure duration, metal speciation, and the biological sensitivity of exposed species. Through bioaccumulation along food chains, humans — as apex consumers — face disproportionately elevated health risks [2].

III.1.2.4.3. Air Contamination

Rapid urbanization and industrialization have intensified atmospheric heavy metal loading, largely through particulate matter (PM2.5 and PM10) generated by traffic, industry, and natural events such as dust storms and volcanic eruptions. These airborne particles are associated with respiratory infections, cardiovascular disease, and premature mortality, while also contributing to acid rain, smog, and infrastructure corrosion. Atmospheric heavy metals are broadly categorized into three groups: Group 1 (Cu, Cd, Pb), Group 2 (Cr, Mn, Ni, V, Zn), and Group 3 (Na, K, Ca, Ti, Al, Mg, Fe) [2].

A concise summary of the most hazardous heavy metals, their environmental sources, and associated health impacts is provided in **Table (III.3)** [12].

Table (III.3): Sources and Health Impacts of the Most Hazardous Heavy Metals

Heavy Metal	Primary Sources	Health Effects
Mercury (Hg)	Coal burning, acid rain leaching, industrial and mining wastes	Nervous system, kidney, and vision damage
Lead (Pb)	Paint, mining waste, lead pipes, vehicle exhaust	Kidney and nervous system damage, impaired protein synthesis
Cadmium (Cd)	Electroplating, mining, plastic industries, sewage	Kidney disease
Arsenic (As)	Herbicides, wood preservatives, mining	Skin, eye, and liver damage; carcinogenic
Antimony (Sb)	Mining and ore processing	Eye, skin, and lung irritation; cardiac and gastrointestinal effects
Chromium (Cr)	Cement industry, chemical plant effluents, tobacco smoke	Pulmonary fibrosis, lung cancer

III.2. Adsorption and Catalytic Activity of $ZnFe_2O_4$ Nanoparticles in Heavy Metal Removal

III.2.1. Adsorption Mechanisms for Heavy Metal Removal

Several techniques have been developed and industrially applied for the removal of heavy metals from contaminated water, including ion exchange, chemical precipitation, flotation, electrochemical deposition, and adsorption. While each of these methods carries its own merits, most are associated with considerable operational costs and generate substantial volumes of sludge requiring further treatment. Among the available alternatives, adsorption has emerged as one of the most promising approaches for heavy metal remediation, owing to its operational simplicity, flexibility, and potential for low-cost implementation [12].

III.2.1.1. Adsorption: Fundamental Principles

Adsorption is defined as the adhesion of atoms, ions, or molecules from a liquid phase onto the surface of a solid material. It is fundamentally a mass transfer process driven by physical or chemical interactions between the dissolved species and the solid adsorbent surface. In the context of wastewater treatment, the selection of an appropriate adsorbent is governed primarily by two criteria: cost-effectiveness and technical performance. Adsorbents are broadly classified into four categories: natural materials, industrial waste-derived materials, biological materials, and agricultural by-products [12].

III.2.1.1.1. Natural Material Adsorbents

Natural geological materials have been widely investigated as low-cost adsorbents for heavy metal removal. Limestone, for instance, has demonstrated reasonable effectiveness in treating metal-contaminated water, though its removal efficiency often falls short of the levels required for large-scale remediation. Studies conducted on mechanically ground Serbian clay reported complete removal of Cr and Pb at approximately 98%, while Cd and Ni removal reached only 81%. Natural zeolite has also shown encouraging results in treating palm oil mill effluent, achieving removal efficiencies exceeding 50% for Zn(II) and Mn(II), and over 60% for Fe(III) [12].

III.2.1.1.2. Industrial Waste-Derived Adsorbents

The valorization of industrial waste materials as low-cost adsorbents has attracted considerable research interest. Materials such as fly ash, red mud, blast furnace slag, lignin, and sugarcane bagasse have all demonstrated meaningful heavy metal uptake capacities. Research on Turkish coal fly ash revealed that high-calcium fly ash performed comparably to activated carbon in adsorbing Ni(II), Cu(II), and Zn(II). Further studies examining the combined effect of fly ash and lime found that at an adsorbent ratio of 0.66, a lime content of 5% by mass, a concentration of approximately 122 g/L, and a solution temperature of 66°C, optimal adsorption with minimal loss was achieved for Cu^{2+}, Ni^{2+}, Zn^{2+}, Cd^{2+}, and Pb^{2+}. Activated carbon derived from Jatropha husks demonstrated removal efficiencies of 61% for Cr(VI) and 97% for Ni [12].

III.2.1.1.3. Biological and Agricultural Waste Adsorbents

Biosorption using agricultural by-products has gained increasing traction as a sustainable and cost-effective strategy for heavy metal removal. This process relies on the passive binding of metal ions to biomass cellular structures through physicochemical interactions. Comparative studies on pectin-rich fruit peels identified grape peels as the most effective biosorbent for cadmium uptake. Rice husk outperformed sawdust in removing Pb^{2+}, Cd^{2+}, Zn^{2+}, Cu^{2+}, and Ni^{2+}, attributable to its functional silica groups and large surface area. Rutin resin achieved a chromium biosorption capacity of 41.6 mg/g, while chemically modified okra residue demonstrated exceptionally high uptake for Pb^{2+} (273.97 mg/g) and Cd^{2+} (121.51 mg/g). The selectivity of biosorbents toward specific metals is largely dictated by their surface functional groups: silica

shows affinity for sulfur, zinc, and copper; hydroxyl groups favor chromium; and nitro groups preferentially bind lead [12].

III.3. Heavy Metal Removal from Petroleum Wastewater

III.3.1. Preparation of $ZnFe_2O_4$ Nanoparticle Suspensions

All nanoparticle suspensions were prepared using ultrapure water to ensure the highest possible quality and reproducibility of experimental conditions. Upon initial preparation, nanoparticles commonly tend to cluster and settle at the bottom of the container, forming aggregates that must be disrupted prior to use. To achieve adequate and homogeneous dispersion, sonication was employed as the primary dispersion technique, leveraging ultrasonic wave energy to break down particle agglomerates at the individual particle level. This step is particularly critical for $ZnFe_2O_4$ nanoparticles, which exhibit a natural tendency toward aggregation due to their magnetic character and high surface energy. For all experimental trials, suspensions were prepared at a concentration of 5 mg of nanoparticles per 1 mL of distilled water [13, 14].

III.3.2. Analytical Instrumentation: ICP-MS NexION 2000

Heavy metal concentrations in the petroleum wastewater samples were quantified using an Inductively Coupled Plasma Mass Spectrometer (ICP-MS), model NexION 2000, supplied by HTDS, as shown in **Figure (III.5)**. This instrument represents one of the most sensitive analytical platforms currently available for trace elemental analysis, combining inductively coupled plasma ionization with high-resolution mass spectrometry to achieve detection limits at the parts-per-trillion (ppt) level.

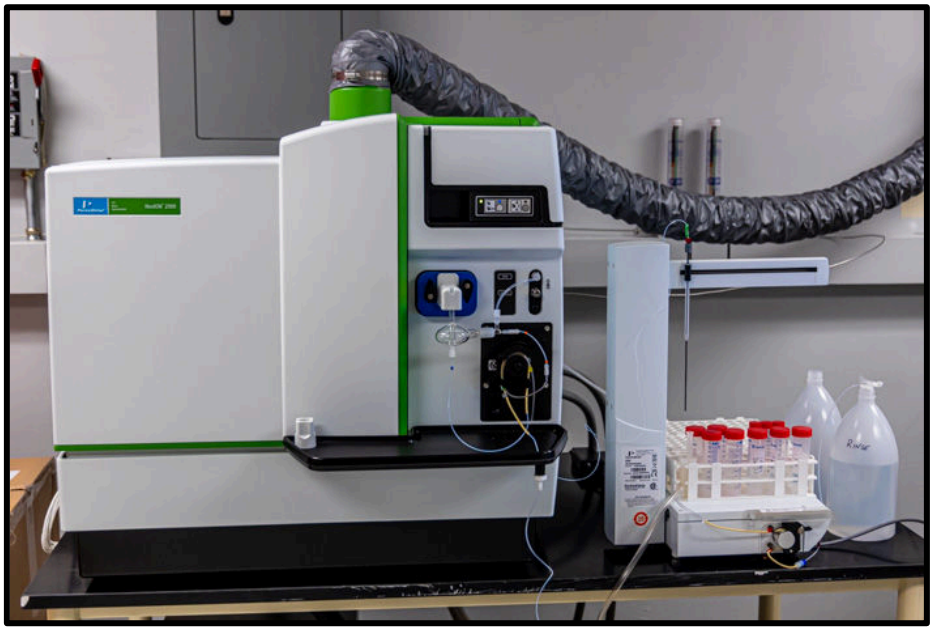

Figure (III.5): *NexION 2000 ICP-MS Spectrometer used for heavy metal quantification in this study.*

III.3.2.1. Instrument Operating Principle

The analytical sequence of the NexION 2000 proceeds through the following stages:

1. **Sample Introduction:** The liquid sample is injected via a 0.5 mL injection loop into a water-cooled spray chamber maintained at a controlled temperature.
2. **Nebulization and Aerosol Generation:** A variable-speed peristaltic pump drives the sample through a nebulizer, converting it into a fine aerosol that is subsequently carried into the plasma zone by a high-purity argon gas stream (99.9999% purity).
3. **Plasma Ionization:** Within the inductively coupled plasma, operating at temperatures between 6,000 and 7,000 K, the aerosol is completely vaporized and its constituent atoms are ionized.
4. **Mass Separation and Detection:** The generated ions are transferred into the mass spectrometer, where they are resolved according to their mass-to-charge ratio (m/z) and quantified with high precision.

5. **Gas Flow Management:** Dedicated flow regulators independently control the nebulizer, plasma, and auxiliary gas streams to maintain stable plasma conditions throughout the analysis.
6. **Interference Mitigation:** An extraction system removes matrix-derived impurities, and Kinetic Energy Discrimination (KED) mode is applied to suppress polyatomic spectral interferences.

III.3.2.2. Key Instrument Components

The NexION 2000 system comprises the following principal components: a water-cooled spray chamber for thermal stabilization of the incoming aerosol; a peristaltic pump-driven nebulizer for consistent sample delivery; a valve system equipped with a 0.5 mL injection loop; high-purity argon and helium gas supply cylinders; Syngistix data acquisition and analysis software; and 20 mL polypropylene sample storage tubes.

III.3.2.3. Analytical Applications in This Work

In the context of this study, the ICP-MS instrument was deployed to determine the concentrations of heavy metals — including As, Cd, and Pb — in petroleum wastewater samples before and after treatment with $ZnFe_2O_4$ nanoparticles. The simultaneous multi-element detection capability of the instrument made it particularly well suited for evaluating adsorption efficiency across several metal species in a single analytical run, thereby ensuring both accuracy and experimental throughput in the assessment of the nanoparticles' remediation performance.

III.3.3. Adsorption Mechanism of Heavy Metals on $ZnFe_2O_4$ Nanoparticles

The removal of heavy metals from petroleum wastewater using $ZnFe_2O_4$ spinel ferrite nanoparticles proceeds through a series of sequential mass transfer and surface interaction steps, as illustrated in **Figure (III.6)**. Upon introduction of the nanoparticles into the wastewater, the system is maintained under stirring conditions for a contact period of 30 minutes to allow sufficient interaction between the nanoparticle surfaces and the dissolved metal ions. The loaded nanoparticles are subsequently separated by centrifugation. The overall adsorption mechanism unfolds across four distinct stages [10, 15]:

A. External Diffusion: Heavy metal ions present in the bulk wastewater are transported toward the outer surface of the $ZnFe_2O_4$ nanoparticles, driven by concentration gradients and facilitated by convective mixing induced by continuous stirring.

B. Film Diffusion: The ions then traverse the liquid boundary layer enveloping each nanoparticle, migrating through this interfacial film to reach the external particle surface.

C. Surface Diffusion: Once at the nanoparticle surface, the metal ions diffuse laterally across the $ZnFe_2O_4$ surface, navigating toward available active adsorption sites. This step is governed by surface charge interactions and the physicochemical affinity between the metal ions and the spinel ferrite surface.

D. Adsorption and Fixation: In the final stage, the heavy metal ions bind firmly to specific active sites on the $ZnFe_2O_4$ surface through electrostatic attraction, ion exchange, and surface complexation with hydroxyl groups present on the nanoparticle surface, resulting in their effective immobilization and removal from the aqueous phase.

This sequential process culminates in the formation of stable $ZnFe_2O_4$–heavy metal surface complexes. The efficiency of this mechanism stems from the high surface-to-volume ratio inherent to the nanoscale dimensions of the synthesized material, the abundance of reactive surface hydroxyl groups confirmed by FTIR analysis, and the well-ordered spinel lattice structure that provides a chemically active and thermally stable adsorption matrix [16, 17].

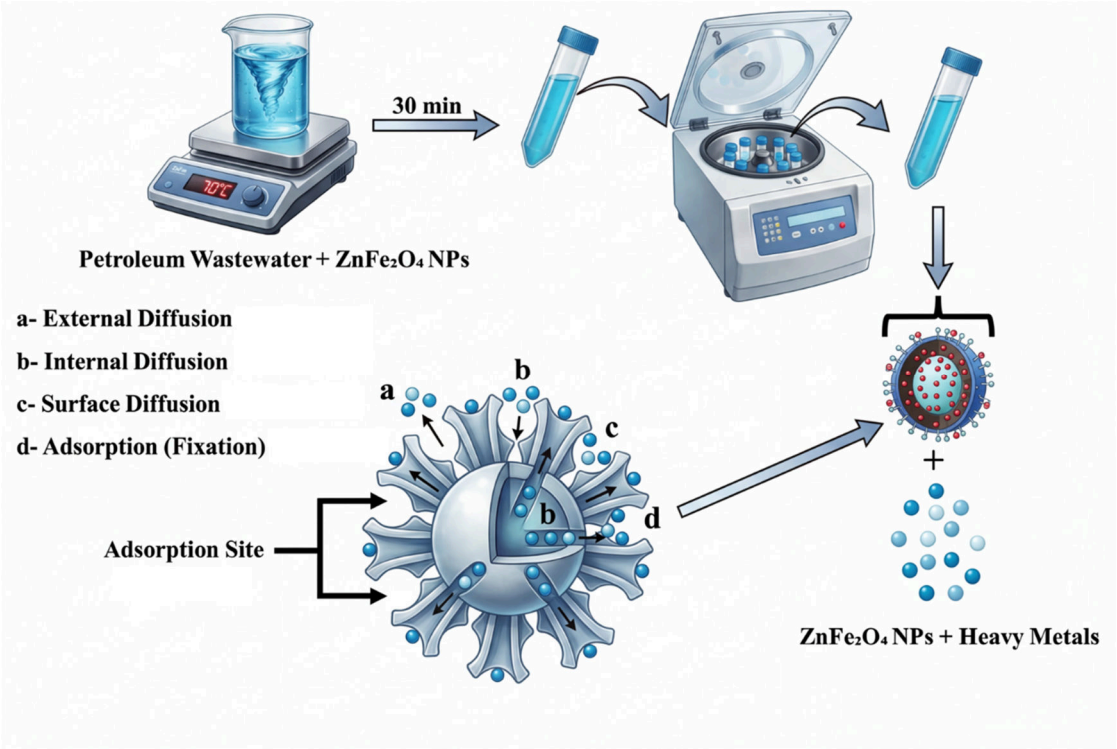

Figure (III.6): *Schematic representation of the stepwise adsorption mechanism of heavy metal ions onto $ZnFe_2O_4$ nanoparticle surfaces* [18].

III.4. Results and Discussion

The remediation performance of $ZnFe_2O_4$ nanoparticles toward petrochemical wastewater was evaluated over a 30-minute treatment period, with measurements taken at five time intervals (0, 5, 10, 20, and 30 minutes). Two categories of pollutants were monitored simultaneously: ten heavy metal species — arsenic (As), cadmium (Cd), chromium (Cr), manganese (Mn), molybdenum (Mo), nickel (Ni), lead (Pb), antimony (Sb), selenium (Se), and zinc (Zn) — and three physicochemical water quality indicators, namely oil-in-water content (OIW), total suspended solids (TSS), and chemical oxygen demand (COD). The complete numerical dataset is consolidated in **Table (III.4)**, while the temporal evolution of removal efficiency for all parameters is graphically presented in **Figure (III.7a)** and **Figure (III.7b)** [19, 20].

The capacity of $ZnFe_2O_4$ to achieve such efficient and rapid pollutant removal is closely linked to its nanostructural characteristics. With a mean crystallite size of approximately 26.74 nm — as confirmed by XRD analysis — the material presents a markedly elevated surface-area-to-volume ratio compared to bulk counterparts. This nanoscale dimensionality translates directly into

a greater density of active surface sites available for interaction with pollutant species in solution, which accounts in large part for the speed and completeness of the removal curves observed in **Figure (III.7)**. Additionally, the estimated optical bandgap energy of Eg = 2.5 eV positions $ZnFe_2O_4$ as a visible-light-responsive semiconductor, enabling the generation of reactive surface species under ambient irradiation conditions — a characteristic that further promotes the destabilisation and capture of both ionic metal species and dissolved organic compounds at the material's surface.

❖ **Heavy Metal Removal**

As illustrated in **Figure (III.7a)** and detailed in **Table (III.4)**, the removal of all ten heavy metals proceeded rapidly from the moment of contact, with the most pronounced rates occurring between 0 and 10 minutes. The initial concentrations of the target species spanned nearly three orders of magnitude — from 125 µg/L for Se to 153,259 µg/L for Zn — yet the material demonstrated consistent performance across this broad range, a feature attributable to its high density of accessible surface sites at the nanoscale.

At the five-minute mark, Mo and Se already exhibited removal efficiencies of 91.63% and 90.88% respectively, indicating a strong early affinity of the $ZnFe_2O_4$ surface for these oxyanion-forming species. Mn and Zn also surpassed 88% removal within the same interval despite their comparatively high initial concentrations. By contrast, Ni displayed the most restrained early-stage response, reaching only 36.81% at five minutes — a divergence that is likely attributable to competition among co-existing metal ions for surface binding sites, as well as to differences in ionic radius and hydration energy that govern how readily each species can approach and bind to the nanoparticle surface. As, Cd, Pb, Sb, and Cr occupied intermediate positions, with five-minute efficiencies ranging between approximately 65% and 78% [16, 18].

The ten-minute data point marked a decisive transition for all species. Cr reached 99.45% removal (residual: 2.32 µg/L), while Mo and Se exceeded 94% and 97% respectively. The remaining metals — with the exception of Ni, which had by then reached 82.29% — had all surpassed 88% removal, confirming that the dominant removal mechanisms were operating at near-maximum capacity within this early window. By 20 minutes, Cr and Mo had both reached 100% removal, and all remaining metals had exceeded 99.47%, leaving only trace residual concentrations. The 30-minute endpoint confirmed the near-total elimination of all species: As, Cd,

Mn, Ni, Pb, Sb, and Zn all achieved efficiencies between 99.90% and 99.997%, while Cr, Mo, and Se recorded complete removal (100%) [21].

❖ **OIW, TSS, and COD Removal**

The temporal profiles for the physicochemical parameters, shown in **Figure (III.7b)** and **Table (III.4)**, exhibit a broadly similar pattern of progressive improvement, though with kinetic characteristics that differ from those of the heavy metals. Starting from initial concentrations of 587 mg/L (OIW), 235 mg/L (TSS), and 6,325 mg/L (COD), all three parameters underwent continuous reduction throughout the 30-minute period, without the near-plateau behaviour that was apparent for most heavy metals beyond 20 minutes.

TSS removal was the fastest of the three in early stages, reaching 62.30% at five minutes and 80.94% at ten minutes, which is consistent with the relatively straightforward physical mechanism of particle aggregation and entrapment at the nanoparticle surface — a process that does not depend on any particular chemical transformation of the target species. OIW followed closely, achieving 45.00% removal at five minutes and 78.50% at ten minutes, before reaching 91.69% and 95.20% at the 20- and 30-minute intervals respectively. The somewhat slower initial rate of OIW removal compared to TSS likely reflects the partial emulsification of oil droplets in the petrochemical matrix, which can hinder direct surface contact in the early stages of treatment.

COD presented the most gradual initial trajectory, with only 38.70% reduction at five minutes, yet it ultimately attained the highest final removal efficiency of the three parameters, reaching 98.34% at 30 minutes. This pattern is mechanistically consistent: COD reduction depends not only on the physical removal of suspended and emulsified organic matter but also on the progressive chemical transformation of dissolved organic compounds at the material's surface — a process that accumulates over time and accounts for the steep COD reduction observed between the 10-minute (72.40%) and 30-minute (98.34%) measurements. The eventual convergence of all three curves toward high removal values by 30 minutes, as visible in **Figure (III.7b)**, underscores the capacity of $ZnFe_2O_4$ to address the organic and colloidal complexity of petrochemical effluent in a comprehensive and time-efficient manner.

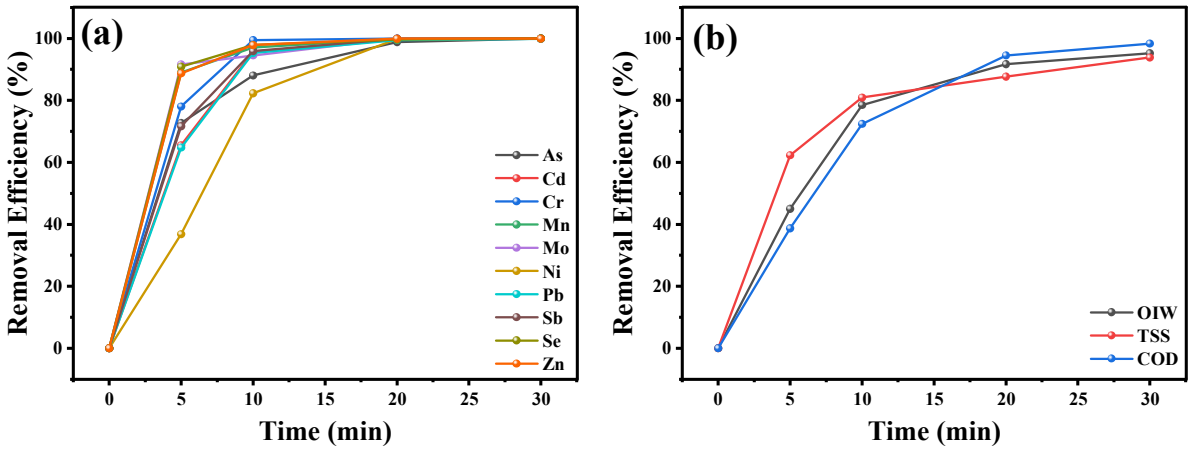

Figure (III.7): *Time-dependent removal efficiency of heavy metals **(a)** and physicochemical parameters (OIW, TSS, and COD) **(b)** from petrochemical wastewater using $ZnFe_2O_4$ nanoparticles.*

Table (III.4): *Measured concentrations and calculated removal efficiencies (RE%) of heavy metals (µg/L) and physicochemical parameters (mg/L) for petrochemical wastewater treated with $ZnFe_2O_4$ NPs as a function of contact time.*

Parameter	t = 0 min		t = 5 min		t = 10 min		t = 20 min		t = 30 min	
	C_0	RE%	C	RE%	C	RE%	C	RE%	C	RE%
Heavy Metals (µg/L)										
As	2537	0	691.6	72.74	303.2	88.05	30.32	98.80	1.253	99.95
Cd	492	0	169.7	65.51	20.88	95.76	1.72	99.65	0.325	99.93
Cr	419	0	92.1	78.02	2.32	99.45	0	100	0	100
Mn	96254	0	10548	89.04	2852.7	97.04	144.8	99.85	70.27	99.93
Mo	135	0	11.3	91.63	7.42	94.50	0	100	0	100
Ni	2426	0	1533	36.81	429.8	82.29	3.62	99.85	0.495	99.98
Pb	2562	0	902.5	64.77	119.9	95.32	13.61	99.47	2.654	99.90
Sb	2135	0	604.9	71.67	88.18	95.87	1.95	99.91	0.064	99.997
Se	125	0	11.4	90.88	2.70	97.84	0.44	99.65	0	100
Zn	153259	0	17265	88.73	3294.9	97.85	105.2	99.93	86.49	99.94
Physicochemical Parameters (mg/L)										
OIW	587	0	322.9	45.00	126.2	78.50	48.8	91.69	28.2	95.20
TSS	235	0	88.6	62.30	44.8	80.94	29.0	87.66	14.5	93.83
COD	6325	0	3877	38.70	1746	72.40	348	94.50	105	98.34

C_0: initial concentration; C: residual concentration at each time point; RE%: removal efficiency (%). Heavy metal concentrations in µg/L; OIW, TSS, and COD concentrations in mg/L.

III.5. Conclusion

This chapter investigated the capacity of $ZnFe_2O_4$ nanoparticles to simultaneously remove heavy metal contaminants and improve the physicochemical quality of petrochemical wastewater within a single short treatment cycle. The results obtained over a 30-minute contact period were, by any reasonable measure, compelling.

Across all ten heavy metals monitored — As, Cd, Cr, Mn, Mo, Ni, Pb, Sb, Se, and Zn — the material achieved near-total elimination regardless of the initial concentration, which varied across nearly three orders of magnitude. Cr, Mo, and Se reached complete removal (100%) as early as the 20-minute mark, while the remaining seven metals all surpassed 99.90% removal by 30 minutes. Notably, even Ni — which showed the most restrained early-stage response at only 36.81% after five minutes, likely due to competitive ion effects and its relatively high hydration energy — ultimately reached 99.98% removal by the end of the treatment period. These results confirm that $ZnFe_2O_4$ does not exhibit a narrow selectivity toward specific metal species, but rather offers a broad and consistent removal capacity across chemically diverse contaminants.

The physicochemical indicators followed a similarly positive trajectory, though with kinetic profiles that reflected the distinct nature of each removal mechanism. TSS responded most rapidly, reaching 62.30% reduction within the first five minutes through straightforward physical aggregation at the nanoparticle surface, and attaining 93.83% by 30 minutes. OIW removal progressed more gradually in the early stages — a behaviour consistent with the emulsified state of oil droplets in the petrochemical matrix — before reaching 95.20% at the final time point. COD, which captures the cumulative burden of dissolved and suspended organic matter, showed the steepest reduction in the later stages of treatment, ultimately achieving 98.34% — the highest final efficiency among the three parameters — reflecting the time-dependent nature of organic compound transformation at the material's surface.

The performance observed across both categories of pollutants is grounded in two key material characteristics: a mean crystallite size of approximately 26.74 nm, which confers an elevated surface-area-to-volume ratio and a high density of active adsorption sites, and an optical bandgap energy of 2.5 eV, which enables surface reactivity under visible light irradiation. Together, these properties underpin the speed, completeness, and versatility of the remediation process

documented in this chapter, and position $ZnFe_2O_4$ as a promising candidate for the treatment of complex industrial effluents where multiple classes of pollutants must be addressed simultaneous

References

References

1. Barakat MA (2011) New trends in removing heavy metals from industrial wastewater. Arab J Chem 4:361–377. https://doi.org/10.1016/j.arabjc.2010.07.019

2. Masindi V, Muedi KL (2018) Environmental Contamination by Heavy Metals. Heavy Met. https://doi.org/10.5772/intechopen.76082

3. Rosato E, Merone GM, Locatelli M, et al (2022) Analytical Chemistry: Tasks, Resolutions and Future Standpoints of the Quantitative Analyses of Environmental Complex Sample Matrices. Analytica 3:312–324. https://doi.org/10.3390/analytica3030022

4. Awa SH, Hadibarata T (2020) Removal of Heavy Metals in Contaminated Soil by Phytoremediation Mechanism: a Review. Water Air Soil Pollut 231:47. https://doi.org/10.1007/s11270-020-4426-0

5. Oladimeji TE, Oyedemi M, Emetere ME, et al (2024) Review on the impact of heavy metals from industrial wastewater effluent and removal technologies. Heliyon 10:e40370. https://doi.org/10.1016/j.heliyon.2024.e40370

6. Waldron T (1988) G . Grupe et al . (eds .), Trace Elements in Environmental History © Springer-Verlag Berlin Heidelberg 1988

7. Buckner CA, Lafrenie RM, Dénommée JA, et al (2016) We are IntechOpen , the world ' s leading publisher of Open Access books Built by scientists , for scientists TOP 1 %. Intech 11:13

8. Ab Hamid NH, bin Mohd Tahir MIH, Chowdhury A, et al (2022) The Current State-Of-Art of Copper Removal from Wastewater: A Review. Water (Switzerland) 14:. https://doi.org/10.3390/w14193086

9. Karak P (2022) Arsenic Contamination and its Impact on the Environment. Curr World Environ 17:58–73. https://doi.org/10.12944/cwe.17.1.6

10. Akpomie KG, Conradie J, Adegoke KA, et al (2023) Adsorption mechanism and modeling of radionuclides and heavy metals onto ZnO nanoparticles: a review. Appl Water Sci 13:20. https://doi.org/10.1007/s13201-022-01827-9

11. García-Niño WR, Pedraza-Chaverrí J (2014) Protective effect of curcumin against heavy metals-induced liver damage. Food Chem Toxicol 69:182–201. https://doi.org/10.1016/j.fct.2014.04.016

12. Bobade V, Eshtiaghi N, Eshtiagi N (2015) Heavy Metals Removal from Wastewater by Adsorption Process: A Review Aerated sludge rheology View project Digester hydrodynamics View project Heavy Metals Removal from Wastewater by Adsorption Process: A Review

13. Ben Ali O, Bouafia A, Meneceur S, et al (2026) Modified Pechini-synthesized Brownmillerite Ca2Fe2O5 nanoparticles with superior photocatalytic and multifunctional wastewater treatment performance: from dye degradation to petroleum effluent remediation. J Sol-Gel Sci Technol 117:18. https://doi.org/10.1007/s10971-025-07043-6

14. Bouaoune A, Mebarki F, Bouafia A, Meneceur S (2025) Eco-friendly α-Fe_2O_3@NiO core-shell nanocomposite via Moltkiopsis ciliata extract: High-efficiency photocatalytic degradation of dyes and antibiotics for sustainable wastewater treatment. J Water Process Eng 79:109046. https://doi.org/10.1016/j.jwpe.2025.109046

15. Singh S, Kapoor D, Khasnabis S, et al (2021) Mechanism and kinetics of adsorption and removal of heavy metals from wastewater using nanomaterials. Environ Chem Lett 19:2351–2381. https://doi.org/10.1007/s10311-021-01196-w

16. Meneceur S, Bouafia A, Laouini SE, et al (2023) Removal efficiency of heavy metals, oily in water, total suspended solids, and chemical oxygen demand from industrial petroleum wastewater by modern green nanocomposite methods. J Environ Chem Eng 11:111209. https://doi.org/10.1016/j.jece.2023.111209

17. Hasan GG, Laouini SE, Osman AI, et al (2024) Nanostructured Mn@NiO composite for addressing multi-pollutant challenges in petroleum-contaminated water. Environ Sci Pollut Res 31:44254–44271. https://doi.org/10.1007/s11356-024-34012-3

18. Bouafia A, Meneceur S, Chami S, et al (2023) Removal of hydrocarbons and heavy metals from petroleum water by modern green nanotechnology methods. Sci Rep 13:5637. https://doi.org/10.1038/s41598-023-32938-1

19. Ouezzani M, Allaoui A, Nesrat HS, et al (2026) Hydrothermal synthesis, photocatalytic hydrogen evolution, CO_2 reduction, organic dyes degradation, heavy metals adsorption, and photoelectrochemical applications of a multifunctional Co- doping $NiFe_2O_4$ spinel. Ionics (Kiel). https://doi.org/10.1007/s11581-026-07009-w

20. Aouadi S, Ferhat MF, Nesrat HS, et al (2025) Sol–gel synthesized MgO nanoparticles: Versatile applications in photocatalytic dye degradation, heavy metal removal, CO2 conversion, hydrogen production, and photoelectrochemical performance. Environ Prog Sustain Energy 45:. https://doi.org/10.1002/ep.70281

21. Hasan GG, Laouini SE, Osman AI, et al (2024) Nanostructured Mn@NiO composite for addressing multi-pollutant challenges in petroleum-contaminated water. Environ Sci Pollut Res 31:44254–44271. https://doi.org/10.1007/s11356-024-34012-3

CHAPTER IV
Photocatalytic Activity Study of Rose Bengal

Azo dyes represent one of the most extensively manufactured classes of synthetic colorants, accounting for more than half of the total global dye production. Their widespread use across industries such as textiles, leather tanning, paper manufacturing, and food processing is largely driven by their chemical stability, structural diversity, and strong tinctorial properties. However, this very stability, which makes them commercially attractive, also renders them highly persistent in aquatic environments. When dye-laden effluents are discharged without adequate treatment, they infiltrate surface water bodies and groundwater reservoirs, giving rise to serious ecological disturbances and posing substantial risks to human health [1].

The problem of dye contamination has grown into one of the most pressing environmental challenges of the current era. Even at sub-milligram concentrations, synthetic dyes can reduce light penetration into water bodies, thereby disrupting photosynthesis in aquatic ecosystems and disturbing the broader food chain. In response, the scientific community has devoted considerable effort to developing effective water treatment strategies, with the ultimate goal of minimizing dye-related contamination and its downstream consequences [2].

Conventional water treatment approaches, including coagulation, adsorption onto activated carbon, and biological degradation, have been widely investigated and applied at industrial scale. While these methods can reduce the overall pollutant load to varying degrees, they frequently fall short of achieving complete mineralization of dye molecules. In many cases, they merely transfer the contaminant from the liquid phase to a solid waste stream rather than destroying it entirely. Furthermore, the operational costs associated with these conventional techniques, combined with their limited efficiency against recalcitrant organic compounds, have motivated the search for more robust and cost-effective alternatives [3, 4].

Among the emerging treatment strategies, heterogeneous photocatalysis has attracted particular attention as a promising member of the broader family of advanced oxidation processes (AOPs). The fundamental principle underlying photocatalysis involves the generation of highly reactive oxygen species, primarily hydroxyl radicals (•OH), upon irradiation of a semiconductor photocatalyst with light of sufficient energy. These radicals attack the complex aromatic structures of dye molecules in a non-selective manner, leading to their progressive oxidation and ultimately to their complete mineralization into harmless end products such as carbon dioxide and water.

Unlike adsorption-based methods, photocatalytic degradation achieves genuine destruction of the pollutant without producing secondary contamination [5–7].

In this context, spinel ferrite nanoparticles have recently emerged as a highly promising class of visible-light-active photocatalysts. Their moderate bandgap energies, typically falling in the range of 1.9 to 2.7 eV, allow them to harvest a substantial portion of the solar spectrum, making them far more efficient than wide-bandgap semiconductors such as TiO_2 under natural sunlight conditions. Among the spinel ferrite family, zinc ferrite ($ZnFe_2O_4$) occupies a particularly interesting position due to its chemical stability, non-toxicity, and tunable electronic properties. Its normal spinel structure, in which Zn^{2+} cations preferentially occupy tetrahedral sites and Fe^{3+} cations reside on octahedral sites, confers a unique combination of optical and electronic characteristics that make it well suited for photocatalytic applications [8]. The present study is therefore directed toward the synthesis, structural characterization, and optical assessment of $ZnFe_2O_4$ spinel ferrite nanoparticles prepared by the co-precipitation method, with a view to evaluating their potential as visible-light-driven photocatalysts for the degradation of organic dye pollutants.

IV.1. Organic Dyes in Wastewater

The discharge of organic dyes into water bodies has become one of the most persistent and environmentally consequential problems associated with modern industrial activity. Dye-containing effluents originate from a broad spectrum of manufacturing sectors, including textile processing, leather finishing, paper production, food processing, cosmetics formulation, and electronic component fabrication, all of which rely heavily on synthetic colorants at various stages of their production cycles [9]. What makes this issue particularly challenging is not merely the large volume of dye-laden wastewater generated globally each year, estimated at several hundred thousand tonnes of dye lost to effluent streams annually, but rather the intrinsic chemical characteristics of these compounds that make them so difficult to manage once released into the environment [10].

Organic dyes, especially those belonging to the azo, anthraquinone, and triphenylmethane families, are engineered for structural stability and resistance to fading, properties that are commercially desirable but environmentally problematic. Their highly conjugated aromatic ring

systems confer exceptional resistance to biodegradation, thermal decomposition, and conventional chemical oxidation, allowing them to persist in aquatic environments for extended periods without undergoing meaningful transformation [11]. Even at trace concentrations in the parts-per-million or sub-parts-per-million range, these compounds impart intense coloration to receiving water bodies, reducing light penetration and thereby suppressing photosynthetic activity in aquatic organisms. This disruption propagates through the food chain and can lead to significant losses in biodiversity and ecosystem productivity. Beyond ecological impact, several classes of synthetic dyes and their degradation intermediates have been identified as mutagenic, carcinogenic, or acutely toxic to a wide range of organisms, raising serious concerns about their infiltration into drinking water sources and their long-term implications for human health [12].

In response to these growing concerns, a wide array of treatment strategies has been developed and evaluated for the removal of organic dyes from industrial effluents. These approaches can be broadly classified into three main categories: physical, chemical, and biological methods, each carrying its own set of advantages and inherent limitations [13].

Physical treatment methods, including membrane filtration, coagulation-flocculation, and adsorption onto activated carbon or other porous materials, have been among the most widely implemented at industrial scale. Adsorption in particular has received enormous attention due to the high surface area and tunable surface chemistry of modern adsorbents, which allow for the rapid uptake of dye molecules from solution. However, adsorption is fundamentally a separation process rather than a destruction process; it transfers the pollutant from the liquid phase to the solid phase without achieving any actual chemical transformation, thereby generating a secondary solid waste stream that still requires safe disposal [14]. Coagulation and flocculation using inorganic salts of iron or aluminium can aggregate dye particles into settleable flocs, but their efficiency drops sharply for soluble dyes with low molecular weight, and the resulting sludge volumes can be substantial.

Chemical methods, notably ozonation and chlorination, can achieve partial or complete oxidative degradation of dye molecules. Ozone is a powerful oxidant capable of cleaving aromatic rings and disrupting the chromophoric groups responsible for color, but its high production cost, short half-life in water, and the potential formation of toxic oxidation by-products limit its broader applicability [15]. Biological treatment strategies, relying on the metabolic activity of specialized

microorganisms to degrade or decolorize dye molecules, are cost-effective and environmentally benign under optimal conditions, but they are notoriously sensitive to fluctuations in pH, temperature, and dye concentration, and many synthetic dyes are simply too recalcitrant or too toxic to support meaningful microbial activity.

Given these limitations, advanced oxidation processes (AOPs), and heterogeneous photocatalysis in particular, have emerged as a highly promising complementary or standalone strategy for the treatment of dye-contaminated wastewater. Unlike conventional methods, photocatalysis achieves the genuine mineralization of organic dye molecules, converting them entirely into carbon dioxide, water, and inorganic ions without producing secondary pollutants or requiring the disposal of contaminated solid waste. It is within this broader framework that the photocatalytic activity of the $ZnFe_2O_4$ spinel ferrite nanoparticles synthesized in the present work will be evaluated and discussed in the sections that follow.

IV.1.1. Textile Dyes and Their Environmental Impact

Water contamination stands as one of the most critical environmental challenges of the twenty-first century, with consequences that extend far beyond the immediate point of pollution and reverberate throughout entire ecosystems. Aquatic environments are continuously exposed to an increasingly diverse array of contaminants, ranging from heavy metals and agricultural pesticides to synthetic organic compounds and industrial chemicals, each carrying its own toxicological profile and environmental fate [16]. Among the most concerning of these pollutants are persistent organic pollutants (POPs), a broad category that encompasses numerous synthetic dyes, chlorinated solvents, and industrial by-products. What distinguishes POPs from other classes of contaminants is their remarkable resistance to natural degradation processes, including microbial breakdown, photolysis, and hydrolysis, which allows them to accumulate in the environment over timescales of years to decades. Their lipophilic nature further enables them to bioaccumulate through successive trophic levels of the food chain, reaching concentrations in top predators and humans that are orders of magnitude higher than those found in the surrounding environment, with well-documented consequences for endocrine function, immune response, and carcinogenesis [17].

Within this broader landscape of water pollution, synthetic textile dyes occupy a particularly prominent and troubling position. The global textile industry consumes an estimated

700,000 tonnes of synthetic dyes annually, and it is widely reported that between 10% and 15% of the dye used during fabric dyeing processes is lost directly to wastewater streams without being fixed to the fiber. The chemical structures responsible for the intense coloration of these compounds, namely extended conjugated aromatic systems stabilized by electron-withdrawing substituents, are precisely the same features that confer their resistance to biodegradation and their persistence in aquatic environments [18]. Once discharged into receiving water bodies, even at concentrations as low as 1 mg/L, these dyes impart visible coloration that reduces the transparency of the water column, attenuates sunlight penetration, and suppresses the photosynthetic activity of submerged and floating aquatic vegetation. Beyond these aesthetic and ecological disruptions, a growing body of toxicological evidence has established that many synthetic dyes and their metabolic breakdown products exhibit mutagenic, genotoxic, and carcinogenic properties toward aquatic organisms and mammals alike, making their uncontrolled release a matter of serious public health concern [19].

A meaningful understanding of the environmental challenges posed by textile dyes requires familiarity with the remarkable chemical diversity of this class of compounds. Dyes can be classified according to several different criteria, each reflecting a different aspect of their chemistry or application. One widely used classification scheme groups dyes by their ionic character in solution, distinguishing between cationic dyes, which carry a positive charge and bind strongly to negatively charged fiber surfaces, anionic dyes, which are negatively charged and include the majority of acid and reactive dyes used in industrial dyeing, and nonionic dyes, which interact with fibers through non-electrostatic forces such as van der Waals interactions and hydrogen bonding [1]. A second classification system, perhaps more relevant from a chemical standpoint, categorizes dyes according to their core chromophoric functional group. Under this scheme, azo dyes, characterized by one or more nitrogen-nitrogen double bonds (–N=N–), constitute by far the largest and most commercially significant group, accounting for roughly 60 to 70% of all synthetic dyes produced worldwide. Other important chromophoric families include anthraquinone dyes, which are valued for their brilliant blue and green shades and their exceptional lightfastness, phthalocyanine dyes, which offer outstanding stability and are widely used to produce turquoise and navy blue colorations, and indigo-based dyes, which remain important in denim production [18]. A third classification approach, more practically oriented, groups dyes by their method of application to textile substrates, yielding categories such as reactive dyes, vat dyes, disperse dyes,

direct dyes, and acid dyes, each of which presents distinct chemical compositions, fixation efficiencies, and environmental behavior in wastewater treatment contexts, as illustrated in **Figure (IV.1)** [20].

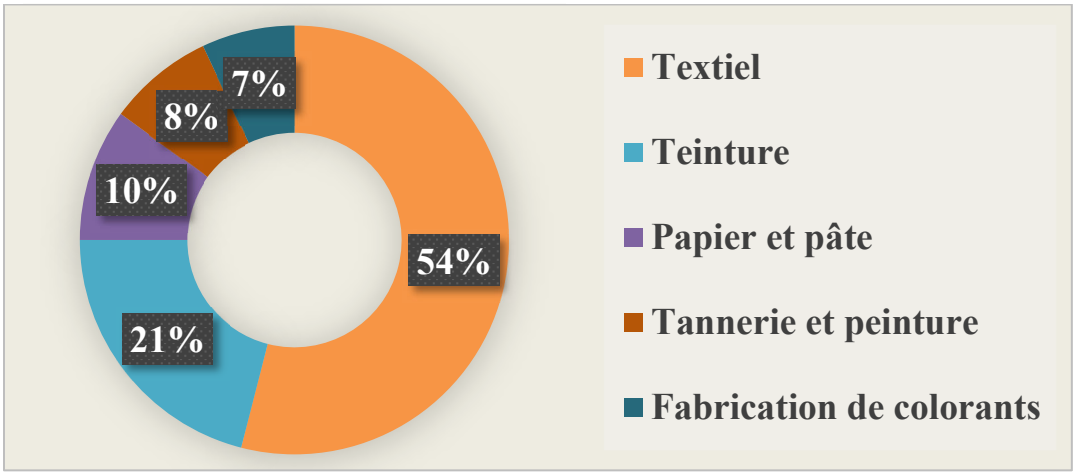

Figure (IV.1) : *Industries responsible for releasing dye-containing effluents into the environment* [20].

IV.1.2. Types of Dyes

The world of synthetic dyes is remarkably diverse, and any attempt to organize this diversity into a coherent classification system must inevitably account for multiple dimensions of their chemistry, including molecular structure, solubility behavior, ionic character, and method of application to substrates. No single classification scheme captures all of these dimensions simultaneously, which is why the scientific and industrial literature commonly employs several overlapping frameworks depending on the context and purpose of the discussion.

From a solubility standpoint, synthetic dyes are broadly divided into two major groups. Water-soluble dyes constitute the first and largest group, encompassing acid dyes, basic or cationic dyes, direct dyes, mordant dyes, and reactive dyes. Acid dyes are anionic compounds that bond to protein-based fibers such as wool, silk, and nylon through electrostatic interactions and hydrogen bonding under acidic dyebath conditions, and they are widely valued for their brilliant shades and broad color range [18]. Basic dyes, by contrast, carry a positive charge and exhibit exceptionally high affinity for acrylic fibers and, to a lesser extent, for wool and silk; their intense tinctorial strength makes them popular despite their relatively poor lightfastness. Direct dyes are applied to

cellulosic fibers such as cotton from a neutral or slightly alkaline bath without the need for a mordant, though their wash fastness is generally inferior to that of reactive dyes. Reactive dyes represent the most important category for cotton dyeing from both a commercial and environmental perspective, as they form covalent bonds with the hydroxyl groups of cellulose fibers, achieving excellent wash fastness; however, the fixation efficiency of reactive dyes rarely exceeds 70 to 80%, meaning that a significant fraction of the applied dye is inevitably lost to the wastewater stream [21].

Water-insoluble dyes form the second major group and include azo dyes developed in situ on the fiber, disperse dyes, sulfur dyes, and vat dyes. Disperse dyes are fine organic pigment particles with very low water solubility, designed specifically for dyeing hydrophobic synthetic fibers such as polyester and acetate through a diffusion mechanism at elevated temperature and pressure. Sulfur dyes are complex polymeric compounds applied in a reduced, soluble form and subsequently oxidized back to their insoluble state within the fiber, producing durable and cost-effective dark shades. Vat dyes, of which indigo is the most historically significant example, follow a similar reduction-oxidation application cycle and are prized for their outstanding fastness properties [22].

Cutting across both solubility categories, azo dyes deserve special attention given their overwhelming dominance in global dye production. Characterized by the presence of one or more azo groups (–N=N–) linking aromatic or heterocyclic ring systems, azo dyes account for approximately 60 to 70% of all synthetic dyes manufactured worldwide, spanning virtually every color of the visible spectrum and finding application in textiles, leather, paper, plastics, food, and cosmetics [1]. Their commercial success stems from the relative simplicity and versatility of their synthesis via diazotization and coupling reactions, which allow fine-tuning of color, solubility, and fastness properties through systematic structural modification. However, this very structural versatility is accompanied by serious environmental and toxicological concerns. The azo linkage can be reductively cleaved by intestinal microflora and certain environmental bacteria, releasing aromatic amines, several of which have been classified as confirmed or suspected human carcinogens by the International Agency for Research on Cancer (IARC). The persistence of azo dyes and their breakdown products in aquatic environments, combined with their demonstrated

acute and chronic toxicity toward fish, invertebrates, and algae, has placed them at the center of regulatory and scientific scrutiny worldwide [23].

These concerns are by no means limited to azo dyes. Across all structural families of synthetic colorants, the combination of chemical stability, biological recalcitrance, and toxicological activity demands the development and implementation of effective removal and degradation technologies. The inadequacy of conventional wastewater treatment processes in achieving complete mineralization of these compounds has driven growing interest in advanced oxidation processes, and heterogeneous photocatalysis in particular, as a viable route to their elimination from contaminated water streams, a direction that forms the central focus of the present work.

IV.1.3. Dye Removal by Adsorption

Adsorption is one of the most widely applied methods for removing synthetic dyes from contaminated water, owing to its operational simplicity, cost-effectiveness, and adaptability to a broad range of pollutant types. The process involves the spontaneous accumulation of dye molecules onto the surface of a solid adsorbent material, driven by electrostatic interactions, hydrogen bonding, and van der Waals forces. The efficiency of any adsorption system depends critically on the specific surface area of the adsorbent, the nature of its surface functional groups, solution pH, initial dye concentration, and contact time [3].

Activated carbon remains the most widely used adsorbent for dye removal, owing to its exceptionally high specific surface area, often exceeding 1000 m^2/g, and its well-developed pore structure. However, its high production cost, limited regenerability, and the challenge of disposing of dye-saturated spent carbon have driven growing interest in alternative materials [4]. In this context, metal oxide nanoparticles have emerged as particularly promising adsorbents. Their nanoscale dimensions confer extremely high surface-area-to-volume ratios, providing an abundance of active adsorption sites per unit mass. Iron oxide nanoparticles such as magnetite (Fe_3O_4) have attracted special attention, as their intrinsic magnetic properties allow simple and energy-efficient recovery from treated water using an external magnetic field [24].

Among the more recently explored materials, spinel ferrite nanoparticles, including $ZnFe_2O_4$, offer a notable functional advantage over conventional adsorbents. The surface hydroxyl

groups on their nanoparticle surfaces facilitate dye adsorption through ligand exchange and hydrogen bonding mechanisms, while their semiconducting character simultaneously enables photocatalytic degradation of the adsorbed molecules under light irradiation [25]. This combination of adsorption and photocatalytic activity in a single material represents a significant step forward compared to purely adsorptive approaches, which inherently suffer from the limitation that captured dye molecules are not destroyed but merely transferred from the liquid phase to the solid phase, necessitating further treatment or disposal of the saturated adsorbent [26].

IV.1.4. Photocatalysis

Heterogeneous photocatalysis has established itself over the past two decades as one of the most powerful and scientifically well-founded approaches within the broader family of advanced oxidation processes for the treatment of dye-contaminated wastewater. Unlike conventional treatment methods that merely transfer pollutants from one phase to another, photocatalysis achieves the complete mineralization of organic dye molecules, converting them irreversibly into carbon dioxide, water, and inorganic ions without generating secondary pollutants or hazardous solid waste streams [27].

The operating principle of heterogeneous photocatalysis is rooted in the electronic band structure of semiconductor materials. When a semiconductor photocatalyst is illuminated with photons carrying energy equal to or greater than its bandgap energy, electrons are promoted from the valence band to the conduction band, generating electron-hole pairs (e^-/h^+). These charge carriers migrate rapidly to the surface of the photocatalyst, where they participate in a cascade of redox reactions with adsorbed water molecules and dissolved oxygen. Valence band holes oxidize surface-adsorbed water or hydroxide ions to produce highly reactive hydroxyl radicals (•OH), while conduction band electrons reduce dissolved molecular oxygen to generate superoxide radical anions ($•O_2^-$). Both species, and particularly the hydroxyl radical, are non-selective and extremely powerful oxidants capable of attacking and breaking down the complex aromatic ring systems of synthetic dye molecules, ultimately driving their complete mineralization [5].

The overall photocatalytic mechanism can be summarized through the following sequence of reactions:

Semiconductor + $h\nu \rightarrow e^-(CB) + h^+(VB)$

$h^+(VB) + H_2O \rightarrow \bullet OH + H^+$

$e^-(CB) + O_2 \rightarrow \bullet O_2^-$

$\bullet OH + Dye \rightarrow$ degradation intermediates $\rightarrow CO_2 + H_2O$

The efficiency of a photocatalytic system depends on several interconnected factors, including the bandgap energy of the semiconductor, its specific surface area, the rate of electron-hole recombination, the light source wavelength and intensity, the initial dye concentration, and the solution pH [28]. Rapid recombination of photogenerated electron-hole pairs before they can reach the particle surface and initiate surface redox chemistry remains the principal limitation of most semiconductor photocatalysts, and a significant portion of current research effort is directed toward strategies for suppressing this recombination, such as heterojunction formation, metal doping, and morphological engineering of the photocatalyst [29].

Titanium dioxide (TiO_2) in its anatase form has historically been the benchmark photocatalyst, owing to its chemical stability, non-toxicity, and well-characterized photocatalytic activity. However, its wide bandgap of approximately 3.2 eV restricts its photoresponse to the ultraviolet region, which constitutes only about 4 to 5% of the solar spectrum, severely limiting its practical efficiency under natural sunlight [6]. This fundamental constraint has motivated intensive research into visible-light-active photocatalysts with narrower bandgaps, among which spinel ferrite nanoparticles have emerged as particularly promising candidates. With bandgap energies typically falling between 1.9 and 2.7 eV, materials such as $ZnFe_2O_4$ can harvest a substantially larger fraction of the solar spectrum, making them far more suitable for solar-driven photocatalytic applications [30].

IV.1.5. Rose Bengal

IV.1.5.1. Definition and General Properties

Rose Bengal (RB) is a synthetic halogenated fluorescent dye belonging to the xanthene family of organic colorants, more specifically classified as a tetraiodotetraclhorofluorescein derivative. Its systematic IUPAC name is 4,5,6,7-tetrachloro-2',4',5',7'-tetraiodofluorescein, and its molecular structure, shown in **Figure (IV.2)**, is characterized by a xanthene core substituted with four chlorine atoms on the benzene ring and four iodine atoms on the fluorescein moiety, a

combination that confers its distinctive deep pink to red coloration and its remarkable photochemical reactivity [31]. This high degree of halogenation is directly responsible for several of Rose Bengal's most important physicochemical properties, including its strong light absorption in the visible region centered around 549 nm, its high molar extinction coefficient, and its exceptional efficiency in generating singlet oxygen upon photoexcitation, a property that has made it one of the most studied photosensitizers in both biomedical and environmental research contexts [32].

From a physicochemical standpoint, Rose Bengal is an anionic dye that carries a net negative charge under neutral and alkaline pH conditions, owing to the dissociation of its carboxylate group. It dissolves readily in water, producing intensely colored pink solutions even at very low concentrations, which is consistent with its high molar absorptivity. Its photostability under prolonged light irradiation, combined with its resistance to conventional biological degradation, classifies it among the persistent organic dye pollutants of environmental concern [33]. The principal physicochemical properties of Rose Bengal are summarized in **Table (IV.1)**.

In the biomedical field, Rose Bengal has found longstanding application as a diagnostic staining agent in ophthalmology, where it is used to detect damaged or devitalized epithelial cells on the ocular surface, and in histology, where it serves as a counterstain for visualizing cytoplasmic components in tissue sections. Its high affinity for proteins and its ability to bind selectively to denatured cellular material make it a valuable tool for the diagnosis of conditions such as dry eye syndrome, keratoconjunctivitis sicca, and various corneal pathologies [34]. More recently, the potent photosensitizing properties of Rose Bengal have attracted attention in the context of photodynamic therapy, where its capacity to generate reactive oxygen species upon visible light irradiation has been exploited for the selective destruction of tumor cells and pathogenic microorganisms.

From an environmental perspective, Rose Bengal is increasingly used as a model dye pollutant in photocatalytic degradation studies, precisely because its strong and well-defined absorption band in the visible region makes it straightforward to monitor spectrophotometrically, and because its structural complexity and resistance to conventional treatment methods make it a meaningful and challenging test substrate for evaluating the performance of novel photocatalytic materials [32]. It is in this capacity that Rose Bengal serves as the target pollutant in the

photocatalytic evaluation of the $ZnFe_2O_4$ spinel ferrite nanoparticles synthesized in the present work.

Figure (IV.2) : *Photograph of Rose Bengal powder.*

Table (IV.1) : *Physicochemical properties of Rose Bengal (RB).*

Property	Rose Bengal (RB)
Appearance	Red-brown powder
Molecular formula	$C_{20}H_4Cl_4I_4O_5$
Molar mass ($g \cdot mol^{-1}$)	973.67 ± 0.026
Water solubility at 20 °C	8.7 g/L
Melting point (°C)	190 – 195
Maximum absorption wavelength (λmax)	549 nm
Charge in solution	Anionic
Colour Index number	CI 45440

Chemical structure	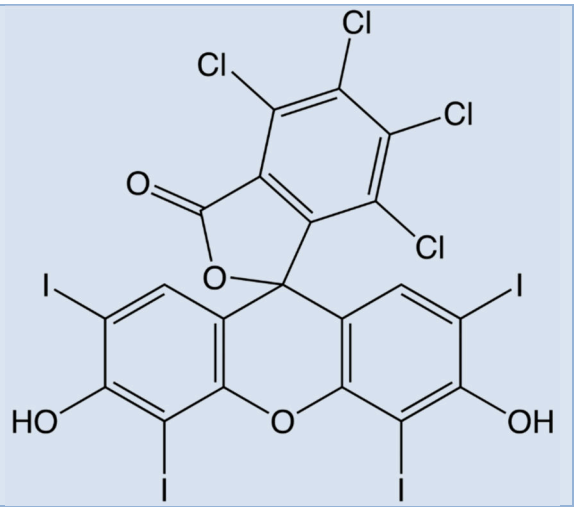

IV.2. Evaluation of Photocatalytic Activity

In this study, $ZnFe_2O_4$ spinel ferrite nanoparticles were selected as the photocatalytic material owing to their promising optical and structural properties established in the preceding chapter, particularly their visible-light-active bandgap energy of 2.5 eV and their well-crystallized pure spinel phase confirmed by XRD analysis. Rose Bengal dye was chosen as the target model pollutant given that it represents one of the most commonly encountered and environmentally persistent synthetic dyes in industrial wastewater. As a halogenated xanthene dye, Rose Bengal poses a significant threat to both aquatic ecosystems and human health due to its toxicity and its well-documented resistance to conventional degradation methods. It is therefore essential to develop efficient and environmentally friendly approaches capable of eliminating such organic dye pollutants from contaminated water. This study aims to evaluate the ability of the synthesized $ZnFe_2O_4$ nanoparticles to degrade Rose Bengal in aqueous solution under visible light irradiation, with the broader goal of establishing their potential as effective and sustainable photocatalytic materials for water treatment applications.

IV.2.1. Chemical Reagents

In this study, several reagents were used throughout the experimental procedures. Zinc acetate dihydrate $Zn(CH_3COO)_2 \cdot 2H_2O$, with a purity of 98%, and iron(III) chloride hexahydrate $FeCl_3 \cdot 6H_2O$, with a purity of 99%, were both obtained from Sigma-Aldrich, Germany, and served as the metal ion precursors for the synthesis of $ZnFe_2O_4$ nanoparticles. Sodium hydroxide (NaOH),

also supplied by Sigma-Aldrich, was used as the precipitating agent and pH regulator during the co-precipitation process. Deionized water was used as the solvent in all stages of the synthesis and photocatalytic experiments. Rose Bengal dye, which served as the model organic pollutant for the photocatalytic degradation tests, was supplied by a certified chemical provider. All reagents were used as received without any further purification.

IV.2.2. Photocatalytic Activity

- ***Principle:***

This study aimed to evaluate the photocatalytic efficiency of the synthesized $ZnFe_2O_4$ spinel ferrite nanoparticles in degrading Rose Bengal dye in aqueous solution under natural solar light irradiation.

- ***Procedure :***

All photocatalytic degradation experiments were conducted outdoors on February 25, 2026, under clear sunny sky conditions at the University of El Oued, Algeria, using natural sunlight as the sole irradiation source. For each experimental run, a carefully weighed amount of 5 mg of the synthesized $ZnFe_2O_4$ spinel ferrite nanoparticles was introduced into 10 mL of an aqueous Rose Bengal solution prepared at a fixed initial concentration of 5×10^{-5} M. The resulting dye-catalyst suspensions were thoroughly mixed prior to sun exposure to ensure uniform distribution of the nanoparticles throughout the solution. A total of six identical samples were prepared in parallel and subsequently placed under direct sunlight, with individual samples withdrawn from irradiation at predetermined time intervals of 15, 30, 45, 60, 75, and 90 minutes, as shown in **Figure (IV.3)**. Throughout the duration of the experiments, the ambient temperature remained relatively stable at approximately 34 °C. At each sampling point, the withdrawn suspension was centrifuged to separate the catalyst particles from the treated solution, after which the clear supernatant was analyzed using a UV-Vis spectrophotometer at the characteristic absorption wavelength of Rose Bengal ($\lambda max = 542$ nm) to determine the residual dye concentration [8, 35, 36]. The photocatalytic degradation efficiency at each irradiation time was then calculated according to the following expression (**Eq (IV.1)**):

$$\text{Degradation efficiency (\%)} = \frac{C_0 - C_t}{C_0} \times 100 \qquad \textbf{(IV. 1)}$$

where C_0 is the initial dye concentration at t = 0, and C_t is the residual dye concentration at irradiation time t.

Figure (IV.3): *Photodegradation of Rose Bengal under natural solar light irradiation using $ZnFe_2O_4$ nanoparticles.*

IV.3. Results of the Photocatalytic Activity of $ZnFe_2O_4$ Nanoparticles for Rose Bengal Degradation

The photocatalytic performance of the synthesized $ZnFe_2O_4$ spinel ferrite nanoparticles was assessed through their ability to degrade Rose Bengal dye in aqueous solution under natural solar light irradiation. The most immediate and visually compelling evidence for the photocatalytic activity of the synthesized $ZnFe_2O_4$ nanoparticles is provided by the striking color change observed in the treated dye solution, as illustrated in **Figure (IV.4)**. The photograph clearly shows a pronounced decoloration of the Rose Bengal solution after 90 minutes of solar irradiation in the presence of the catalyst, with the initially intense pink solution becoming nearly colorless, providing direct visual confirmation of the efficient destruction of the dye chromophore by the photocatalytic process.

Figure (IV.4) : *Photograph showing the visual decoloration of Rose Bengal aqueous solution after photocatalytic degradation using $ZnFe_2O_4$ nanoparticles under natural solar irradiation; the tubes on the right show the initial intense pink-colored dye solution prior to irradiation, while the tubes on the left show the nearly colorless treated solution after 90 minutes of sun exposure.*

The evolution of the degradation process was further monitored quantitatively by recording the UV-Vis absorption spectra of the dye solution at regular irradiation intervals, and the results are presented in **Figures (IV.5a)** and **(IV.5b)**.

As clearly shown in **Figure (IV.5a)**, the characteristic absorption peak of Rose Bengal centered at λmax = 542 nm decreased progressively and continuously with increasing irradiation time, reflecting the gradual destruction of the chromophoric groups responsible for the intense pink coloration of the dye. At t = 0, prior to any light exposure, the absorbance recorded at 542 nm was at its maximum value, corresponding to the initial Rose Bengal concentration of 5×10^{-5} M. As solar irradiation proceeded, a systematic and monotonic reduction in peak intensity was observed at each successive time interval, accompanied by a visible decoloration of the solution that became increasingly pronounced with time. By the end of the 90-minute irradiation period, the absorption peak had been reduced to near-baseline levels, providing direct spectroscopic evidence for the near-complete degradation of the Rose Bengal chromophore [37].

The corresponding degradation efficiency curve, plotted as a function of irradiation time in **Figure (IV.5b)**, provides a clearer quantitative picture of the temporal evolution of the photocatalytic process. The degradation efficiency increased rapidly during the initial stage of irradiation, reaching approximately 39.12% after just 15 minutes of sun exposure, which reflects the high initial rate of reactive oxygen species generation at the $ZnFe_2O_4$ surface under intense solar illumination. This rapid initial degradation can be attributed to the abundance of available active surface sites on the nanoparticles and the high concentration of Rose Bengal molecules accessible for attack by photogenerated hydroxyl radicals (•OH) and superoxide anions ($\bullet O_2^-$) at the beginning of the reaction [38]. As irradiation continued, the degradation efficiency progressed steadily, reaching 60.82% at 30 minutes, 75.70% at 45 minutes, and 80.42% at 60 minutes, before rising further to 84.57% at 75 minutes. A maximum degradation efficiency of 94.38% was ultimately achieved after 90 minutes of solar irradiation, demonstrating the remarkable photocatalytic capability of the synthesized $ZnFe_2O_4$ nanoparticles under natural sunlight conditions.

It is worth noting that the rate of degradation, while consistently positive throughout the experiment, exhibited a gradual deceleration during the later stages of irradiation. This progressive slowdown is a well-documented phenomenon in heterogeneous photocatalysis and can be rationalized by several concurrent factors. As the reaction advances, the concentration of intact Rose Bengal molecules in solution decreases significantly, reducing the probability of productive encounters between dye molecules and reactive oxygen species at the catalyst surface. Simultaneously, the accumulation of oxidative degradation intermediates, including smaller aromatic fragments and carboxylic acid derivatives generated during the progressive breakdown of the Rose Bengal structure, may compete with the parent dye for the available active sites on the $ZnFe_2O_4$ surface, effectively slowing the overall mineralization rate [39]. Despite this kinetic deceleration, the final degradation efficiency of 94.38% achieved within only 90 minutes represents an excellent photocatalytic performance and compares favorably with values reported in the literature for visible-light-driven spinel ferrite photocatalysts tested under comparable experimental conditions [40].

Taken together, these results convincingly demonstrate that the $ZnFe_2O_4$ spinel ferrite nanoparticles synthesized in this work by the co-precipitation method are highly effective visible-light-driven photocatalysts for the degradation of Rose Bengal dye, achieving near-complete

decoloration within a relatively short irradiation period using only natural sunlight as the energy source. These findings highlight the considerable potential of $ZnFe_2O_4$ as an environmentally friendly and cost-effective photocatalytic material for the treatment of dye-contaminated wastewater.

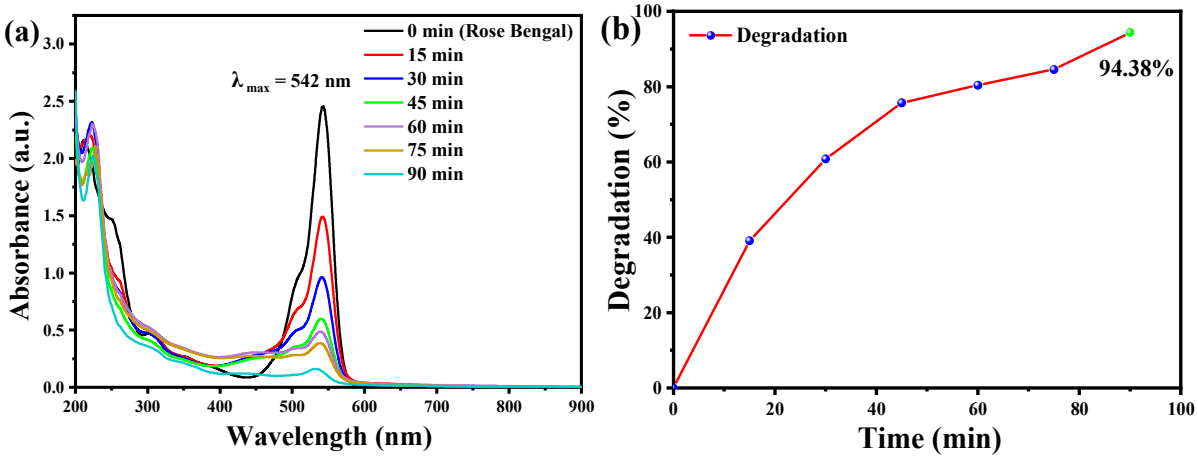

Figure (IV.5): *Photocatalytic degradation of Rose Bengal using $ZnFe_2O_4$ nanoparticles under natural solar irradiation: (a) temporal evolution of UV-Vis absorption spectra at λmax = 542 nm; (b) degradation efficiency as a function of irradiation time.*

IV.4. Conclusion

In this chapter, the photocatalytic activity of the $ZnFe_2O_4$ spinel ferrite nanoparticles synthesized by the co-precipitation method was successfully evaluated through their application to the degradation of Rose Bengal dye in aqueous solution under natural solar light irradiation. The experimental results demonstrated that the synthesized nanoparticles exhibit a notably high photocatalytic efficiency, achieving a degradation efficiency of 94.38% within only 90 minutes of sun exposure, without the need for any artificial light source or chemical oxidant additive.

The strong photocatalytic performance observed in this study can be directly linked to the structural and optical properties of the $ZnFe_2O_4$ nanoparticles established in the preceding chapter, particularly their phase-pure spinel structure, their nanocrystalline character with a mean crystallite size of 26.74 nm, and most importantly their visible-light-active optical bandgap energy of 2.5 eV, which allows them to efficiently harvest solar radiation and generate the reactive oxygen species responsible for dye mineralization. The progressive and steady increase in degradation efficiency

with irradiation time, combined with the near-complete decoloration of the Rose Bengal solution visually confirmed by the photograph in **Figure (IV.4)**, collectively underscore the effectiveness of $ZnFe_2O_4$ as a visible-light-driven photocatalyst for organic dye removal.

These findings establish the co-precipitation route as a simple, scalable, and reliable synthesis approach for producing $ZnFe_2O_4$ photocatalysts with well-defined properties and high degradation performance. More broadly, the results of this chapter highlight the considerable potential of spinel ferrite nanoparticles as environmentally friendly and cost-effective materials for water treatment applications, particularly for the elimination of persistent organic dye pollutants from industrial wastewater. Future investigations could focus on optimizing the catalyst dosage and solution pH, evaluating the reusability and stability of the $ZnFe_2O_4$ nanoparticles over successive degradation cycles, and extending the photocatalytic assessment to a broader range of organic pollutants under both solar and artificial visible light irradiation.

References

References

1. Tkaczyk A, Mitrowska K, Posyniak A (2020) Synthetic organic dyes as contaminants of the aquatic environment and their implications for ecosystems: A review. Sci Total Environ 717:137222. https://doi.org/10.1016/j.scitotenv.2020.137222

2. Holkar CR, Jadhav AJ, Pinjari D V., et al (2016) A critical review on textile wastewater treatments: Possible approaches. J Environ Manage 182:351–366. https://doi.org/10.1016/j.jenvman.2016.07.090

3. Yagub MT, Sen TK, Afroze S, Ang HM (2014) Dye and its removal from aqueous solution by adsorption: A review. Adv Colloid Interface Sci 209:172–184. https://doi.org/10.1016/j.cis.2014.04.002

4. Katheresan V, Kansedo J, Lau SY (2018) Efficiency of various recent wastewater dye removal methods: A review. J Environ Chem Eng 6:4676–4697. https://doi.org/10.1016/j.jece.2018.06.060

5. Miklos DB, Remy C, Jekel M, et al (2018) Evaluation of advanced oxidation processes for water and wastewater treatment – A critical review. Water Res 139:118–131. https://doi.org/10.1016/j.watres.2018.03.042

6. Byrne C, Subramanian G, Pillai SC (2018) Recent advances in photocatalysis for environmental applications. J Environ Chem Eng 6:3531–3555. https://doi.org/10.1016/j.jece.2017.07.080

7. Deng Y, Zhao R (2015) Advanced Oxidation Processes (AOPs) in Wastewater Treatment. Curr Pollut Reports 1:167–176. https://doi.org/10.1007/s40726-015-0015-z

8. Zouari Ahmed R, Laouini SE, Salmi C, et al (2025) Green synthesis of α-Fe2O3 and α-Fe2O3@Ag NC for degradation of rose Bengal and antimicrobial activity. Biomass Convers Biorefinery 15:255–269. https://doi.org/10.1007/s13399-023-05046-3

9. Lellis B, Fávaro-Polonio CZ, Pamphile JA, Polonio JC (2019) Effects of textile dyes on health and the environment and bioremediation potential of living organisms. Biotechnol Res Innov 3:275–290. https://doi.org/10.1016/j.biori.2019.09.001

10. Paździor K, Bilińska L, Ledakowicz S (2019) A review of the existing and emerging

technologies in the combination of AOPs and biological processes in industrial textile wastewater treatment. Chem Eng J 376:120597. https://doi.org/10.1016/j.cej.2018.12.057

11. Kant R (2012) Textile dyeing industry an environmental hazard. Nat Sci 04:22–26. https://doi.org/10.4236/ns.2012.41004

12. Forgacs E, Cserháti T, Oros G (2004) Removal of synthetic dyes from wastewaters: A review. Environ Int 30:953–971. https://doi.org/10.1016/j.envint.2004.02.001

13. Robinson T, McMullan G, Marchant R, Nigam P (2001) Remediation of dyes in textile effluent: A critical review on current treatment technologies with a proposed alternative. Bioresour Technol 77:247–255. https://doi.org/10.1016/S0960-8524(00)00080-8

14. Crini G (2006) Non-conventional low-cost adsorbents for dye removal: A review. Bioresour Technol 97:1061–1085. https://doi.org/10.1016/j.biortech.2005.05.001

15. Paździor K, Wrębiak J, Klepacz-Smółka A, et al (2017) Influence of ozonation and biodegradation on toxicity of industrial textile wastewater. J Environ Manage 195:166–173. https://doi.org/10.1016/j.jenvman.2016.06.055

16. Gavrilescu M, Demnerová K, Aamand J, et al (2015) Emerging pollutants in the environment: Present and future challenges in biomonitoring, ecological risks and bioremediation. N Biotechnol 32:147–156. https://doi.org/10.1016/j.nbt.2014.01.001

17. Sharma S, Bhattacharya A (2017) Drinking water contamination and treatment techniques. Appl Water Sci 7:1043–1067. https://doi.org/10.1007/s13201-016-0455-7

18. Benkhaya S, M' rabet S, El Harfi A (2020) A review on classifications, recent synthesis and applications of textile dyes. Inorg Chem Commun 115:107891. https://doi.org/10.1016/j.inoche.2020.107891

19. Sudarshan S, Harikrishnan S, RathiBhuvaneswari G, et al (2023) Impact of textile dyes on human health and bioremediation of textile industry effluent using microorganisms: current status and future prospects. J Appl Microbiol 134:. https://doi.org/10.1093/jambio/lxac064

20. Katheresan V, Kansedo J, Lau SY (2018) Efficiency of various recent wastewater dye removal methods: A review. J Environ Chem Eng 6:4676–4697. https://doi.org/https://doi.org/10.1016/j.jece.2018.06.060

21. Hunger K (2004) Industrial dyes: Chemistry, properties, applications. Wiley

22. Christie R (2001) Colour Chemistry. The Royal Society of Chemistry

23. Akter T, Protity AT, Shaha M, et al (2023) The Impact of Textile Dyes on the Environment. pp 401–431

24. Nithya R, Thirunavukkarasu A, Sathya AB, Sivashankar R (2021) Magnetic materials and magnetic separation of dyes from aqueous solutions: a review. Environ Chem Lett 19:1275–1294. https://doi.org/10.1007/s10311-020-01149-9

25. Santhosh C, Velmurugan V, Jacob G, et al (2016) Role of nanomaterials in water treatment applications: A review. Chem Eng J 306:1116–1137. https://doi.org/10.1016/j.cej.2016.08.053

26. Crini G, Lichtfouse E (2019) Advantages and disadvantages of techniques used for wastewater treatment. Environ Chem Lett 17:145–155. https://doi.org/10.1007/s10311-018-0785-9

27. Nasr M, Eid C, Habchi R, et al (2018) Recent Progress on Titanium Dioxide Nanomaterials for Photocatalytic Applications. ChemSusChem 11:3023–3047. https://doi.org/10.1002/cssc.201800874

28. Nguyen CH, Fu CC, Juang RS (2018) Degradation of methylene blue and methyl orange by palladium-doped TiO2 photocatalysis for water reuse: Efficiency and degradation pathways. J Clean Prod 202:413–427. https://doi.org/10.1016/j.jclepro.2018.08.110

29. Lakhera SK, Rajan A, T.P. R, Bernaurdshaw N (2021) A review on particulate photocatalytic hydrogen production system: Progress made in achieving high energy conversion efficiency and key challenges ahead. Renew Sustain Energy Rev 152:111694. https://doi.org/10.1016/j.rser.2021.111694

30. Li L, Jianhua W, Fang H (2025) Fabrication of ZnFe2O4@g-C3N4 for enhanced photo-fenton effect and visible light-driven organic dye degradation. Sci Rep 15:21707. https://doi.org/10.1038/s41598-025-05096-9

31. Sharma S, Sharma A (2019) Recent advances in photocatalytic manipulations of Rose Bengal in organic synthesis. Org Biomol Chem 17:4384–4405.

https://doi.org/10.1039/c9ob00092e

32. Sahu A, Choi W Il, Tae G (2012) A stimuli-sensitive injectable graphene oxide composite hydrogel. Chem Commun 48:5820–5822. https://doi.org/10.1039/c2cc31862h

33. Abrahamse H, Hamblin MR (2016) New photosensitizers for photodynamic therapy. Biochem J 473:347–364. https://doi.org/10.1042/BJ20150942

34. Doughty MJ (2013) Rose bengal staining as an assessment of ocular surface damage and recovery in dry eye disease-A review. Contact Lens Anterior Eye 36:272–280. https://doi.org/10.1016/j.clae.2013.07.008

35. Boutalbi A, Meneceur S, Laouini SE, et al (2024) Synthesis of Ag nanoparticles loaded with potassium polyacrylate hydrogel for rose bengal dye removal and antibacterial activity. Biomass Convers Biorefinery 14:23635–23647. https://doi.org/10.1007/s13399-023-04337-z

36. Gharbi AH, Hemmami H, Laouini SE, et al (2024) Novel CuO–SiO2 nanocomposites: synthesis, kinetics, recyclability, high stability and photocatalytic efficiency for Rose Bengal dye removal. Transit Met Chem 49:195–213. https://doi.org/10.1007/s11243-024-00574-x

37. Hasanpour M, Hatami M (2020) Photocatalytic performance of aerogels for organic dyes removal from wastewaters: Review study. J Mol Liq 309:113094. https://doi.org/10.1016/j.molliq.2020.113094

38. Ajmal A, Majeed I, Malik RN, et al (2014) Principles and mechanisms of photocatalytic dye degradation on TiO 2 based photocatalysts: A comparative overview. RSC Adv 4:37003–37026. https://doi.org/10.1039/c4ra06658h

39. Saravanan R, Gracia F, Stephen A (2017) Basic Principles, Mechanism, and Challenges of Photocatalysis. pp 19–40

40. Falak P, Hassanzadeh-Tabrizi SA, Saffar-Teluri A (2017) Synthesis, characterization, and magnetic properties of ZnO-ZnFe2O4 nanoparticles with high photocatalytic activity. J Magn Magn Mater 441:98–104. https://doi.org/10.1016/j.jmmm.2017.05.044

General Conclusion and Future Perspectives

General Conclusion and Future Perspectives

❖ General Conclusion

The central objective of this work was to synthesise, characterise, and evaluate $ZnFe_2O_4$ spinel ferrite nanoparticles as a multifunctional remediation agent for two distinct categories of industrial water pollution: heavy metal contamination in petrochemical wastewater, and the photocatalytic degradation of persistent organic dye pollutants. The results obtained across the four chapters of this study converge toward a coherent and encouraging conclusion — that a single, carefully synthesised nanomaterial can address the full pollutant complexity of real industrial effluents without requiring multi-stage treatment chains, chemical oxidant addition, or artificial irradiation sources.

The foundation of all subsequent findings rested on the structural and optical characterisation presented in Chapter II. The co-precipitation method, followed by calcination at 800 °C, yielded a phase-pure, single-phase $ZnFe_2O_4$ product with a well-ordered cubic spinel $Fd\bar{3}m$ structure, a lattice parameter of 8.4300 Å, and a mean crystallite size of 26.74 ± 0.50 nm. FTIR spectroscopy confirmed the spinel phase through the characteristic metal–oxygen stretching vibrations at 531 cm^{-1} and 432 cm^{-1}, while UV-Vis analysis and Tauc plot construction returned a bandgap energy of 2.5 eV — placing $ZnFe_2O_4$ firmly within the category of visible-light-active semiconductors and anticipating its photocatalytic utility demonstrated in Chapter IV.

The heavy metal removal study in Chapter III produced results that were remarkable in both their speed and completeness. Applied to real petrochemical wastewater containing ten co-existing heavy metal species at concentrations spanning nearly three orders of magnitude, alongside elevated levels of emulsified oil, suspended solids, and dissolved organics, the $ZnFe_2O_4$ nanoparticles achieved removal efficiencies exceeding 99.90% for all metals within 30 minutes. Chromium, molybdenum, and selenium reached complete elimination at 20 minutes, while even nickel — the most kinetically restrained species at early contact times — attained 99.98% removal by the endpoint. Simultaneously, oil-in-water content, total suspended solids, and chemical oxygen demand were reduced by 95.20%, 93.83%, and 98.34% respectively, with each parameter exhibiting a kinetic profile reflective of its specific removal mechanism. These results

demonstrated that $ZnFe_2O_4$ operates through multiple concurrent pathways rather than a single dominant mechanism, which accounts for its effectiveness across chemically diverse contaminant classes.

Chapter IV established a complementary dimension of the material's utility. Under natural solar light irradiation and without any chemical additive, $ZnFe_2O_4$ nanoparticles achieved 94.38% photocatalytic degradation of Rose Bengal dye within 90 minutes — a performance directly attributable to the 2.5 eV bandgap confirmed in Chapter II, which enables efficient visible-light harvesting and the consequent generation of reactive oxygen species responsible for dye mineralisation. This result extended the material's applicability beyond inorganic contaminant removal and into the domain of persistent organic pollutant degradation under practical, solar-driven conditions.

Across all application chapters, two intrinsic material properties emerged consistently as the structural basis for observed performance: the nanoscale crystallite size of ~26.74 nm, conferring a high density of accessible surface sites, and the optical bandgap of 2.5 eV, enabling visible-light-driven surface reactivity. Together, these properties — reliably delivered by the co-precipitation synthesis route — establish $ZnFe_2O_4$ as a structurally well-defined, chemically versatile, and practically viable material for the simultaneous treatment of inorganic and organic pollutants in complex industrial effluents.

❖ Future Perspectives

While the results of this study are scientifically solid, they were obtained under batch laboratory conditions that do not fully replicate the demands of real industrial deployment. The most immediate priority for future work is therefore the evaluation of $ZnFe_2O_4$ performance under continuous-flow conditions using column or fixed-bed reactor configurations, alongside systematic investigation of the material's reusability and structural stability across multiple regeneration cycles — both of which are prerequisites for any credible assessment of practical scalability.

At the mechanistic level, the competitive adsorption behaviour observed among co-existing heavy metal species warrants deeper investigation, particularly with respect to the

influence of pH, ionic strength, and the speciation of target metals under realistic effluent conditions. For the photocatalytic application, radical scavenger experiments to identify the dominant reactive species, combined with studies of catalyst loading and pH effects across a broader range of organic pollutants, would substantially strengthen the mechanistic understanding established here.

More broadly, the dual functionality of $ZnFe_2O_4$ — simultaneously capable of adsorbing heavy metals and photocatalytically degrading organic compounds — suggests the feasibility of an integrated, single-step treatment process for complex effluents where both pollutant classes co-exist. The development of surface-modified or composite $ZnFe_2O_4$ materials, for instance through heterojunction formation with complementary semiconductors to suppress charge carrier recombination and enhance photocatalytic efficiency, represents a promising direction that this work has opened and that future investigations would do well to pursue.